

**Synthesis and Electrochemical Properties of
Advanced Nanostructured Electrode for
Lithium Secondary Batteries Starting from
Layered Compounds**

(層状化合物を出発物質とするナノ構造リチウム二次
電池電極材料の合成と電気化学特性)

by

Quan Zhen

権 振

January, 2013

Department of Materials Science and Engineering

Nagoya Institute of Technology

Japan

Content

Chapter 1 Introduction	1
1.1 Lithium battery	1
1.2 Intercalation compounds for lithium batteries.....	4
1.2.1 <i>LiMO₂ (M: transition metal) layered rocksalt type compounds</i>	4
1.2.2 <i>LiM₂O₄ (M: transition metal) spinel type compounds</i>	10
1.2.3 <i>LiMPO₄ (M: transition metal) olivine type compounds</i>	12
1.3 Nanostructured materials for lithium batteries.....	15
1.4 Nanomaterials derived from layered compounds	20
1.4.1 <i>Layered double hydroxides (LDHs)</i>	21
1.4.2 <i>Nanosheet</i>	22
1.4.3 <i>Multiple metal oxide nanoparticles</i>	24
1.5 Purpose of study	25
Reference	27
Chapter 2 Synthesis and Electrochemical Property of LiCoO₂ Thin Films Composed of Nanosize Compounds Synthesized via Nanosheet Restacking Method	35
2.1 Introduction.....	35
2.2 Experimental.....	38
2.2.1 <i>Synthesis and characterization of LiCoO₂ thin film on Au substrate</i>	38
2.2.2 <i>Electrochemical measurements</i>	39
2.3 Results and discussion	40
2.3.1 <i>Characterization of the LiCoO₂ thin film</i>	40
2.3.2 <i>Electrochemical measurements</i>	46
2.4 Conclusion	52
Reference	53

**Chapter 3 Synthesis and Electrochemical Property of
LiCoO₂ Thin Film Coated on the Surface of Carbon and
Anatase TiO₂ Powders..... 55**

3.1 Introduction 55

3.2 Experimental..... 57

*3.2.1 Synthesis and characterization of LiCoO₂ thin film on glassy
carbon substrate and powder materials..... 57*

3.2.2 Electrochemical measurements..... 58

3.3 Results and discussion 60

3.3.1 LiCoO₂ film on glassy carbon substrate 60

3.3.2 LiCoO₂ coating on the surface of the powder materials 70

3.4 Conclusion..... 77

Reference 78

**Chapter 4 Preparation of Nanocrystalline LiMn₂O₄ Thin
Film by Electrodeposition Method and Its Electrochemical
Performance for Lithium Battery..... 80**

4.1 Introduction 80

4.2 Experimental..... 81

*4.2.1 Synthesis and characterization of LiMn₂O₄ thin film on Au
substrate..... 81*

4.2.2 Electrochemical measurements..... 82

4.3 Results and discussion 84

4.3.1 Characterization of the LiMn₂O₄ thin film on Au substrate... 84

*4.3.2 Electrochemical properties of LiMn₂O₄ thin film on Au
substrate..... 91*

4.4 Conclusion..... 101

Reference 102

Chapter 5 Synthesis and Electrochemical Property of Multiple Metal Oxide Nanoparticles as Cathode of Lithium Battery	104
5.1 Introduction.....	104
5.2 Experimental.....	106
5.2.1 <i>Synthesis and characterization of multiple metal oxide nanoparticles</i>	106
5.2.2 <i>Electrochemical measurements</i>	107
5.3 Results and discussion	108
5.3.1 <i>Characterization of multiple metal oxide nanoparticles</i>	108
5.3.2 <i>Electrochemical property of multiple metal oxide nanoparticles</i>	115
5.3.3 <i>Reaction mechanism based on the ex-situ XRD and the AC-impedance measurement results</i>	118
5.4 Conclusion	124
Reference	125
Chapter 6 Summary.....	127
List of publication	130
Acknowledgements	132

Chapter 1

Introduction

1.1 Lithium battery

The market for Li ion batteries (LIBs) has been rapidly grown with exploding demands for portable electronic devices since the initial commercialization by Sony in 1991. Compared with former generation batteries (e.g. lead-acid, nickel-cadmium, nickel-metal hydride batteries), LIBs can offer high energy density, small size and lightweight design, and longer cyclability. (See Figure 1.1) Indeed, LIBs have been the main backup power sources of portable electronic devices such as cellular phones, laptop computers and mobile electronic equipment. To date, electric vehicles (EV) powered by LIBs have been pushing forward in the worldwide market.

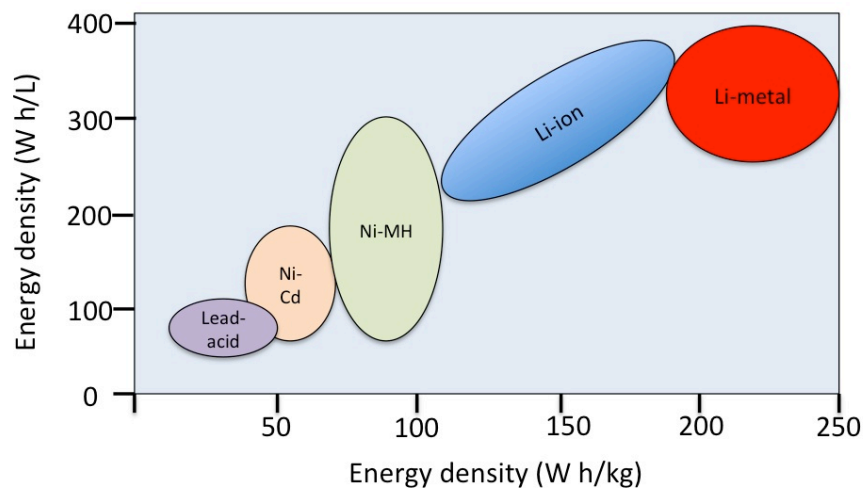


Figure 1.1 Comparison of the different battery technologies in terms of volumetric and gravimetric energy density [1].

The high-energy density of lithium batteries relies on lithium metal anode, because lithium is the lightest (molar mass $M_{\text{Li}}=6.94 \text{ g mol}^{-1}$) and the most electropositive (-3.04 V vs. SHE) metal. Motivated by the advantages of using lithium metal as anode, lithium primary cells were firstly come into practical use in 1970s. Their outstanding higher energy density and power density than other types of primary batteries facilitated lithium primary batteries as power sources for watch, calculator or implantable medical devices. The researches for ‘lithium non-aqueous secondary batteries’, were begun at almost the same period.

As the result of the development of electrochemistry and solid-state chemistry, intercalation materials were crucial in the development of high-energy rechargeable lithium battery system. These materials could introduce lithium ions to inside of their crystalline structure, during the reduction of transition metals from their higher oxidation state. This so-called “topotactical” electrochemical reaction would occur reversibly, without major phase change. Chalcogenides, containing TiS_2 , MoS_2 [2], were the most attractive candidate as the solid solution for rechargeable non-aqueous batteries. Especially, the layered TiS_2 was the best intercalation compound available at the time, having stable layered structure and electronic conductivity [3]. In 1972, Whittingham proposed a new battery system using TiS_2 as cathode, lithium metal as anode and lithium perchlorate in dioxolane as the electrolyte [4]. Although this cell generated the discharge voltage of 2 V that is higher than aqueous system, it was not viable due to the dendritic lithium growth on the anode lithium metal, which leads to explosion hazards during charge-discharge cycling. Besides, a large number of metal oxides were investigated as reversible insertion electrodes such as chromium oxides [5], vanadium oxides [6] and manganese oxide [7]. These oxides indicate higher capacities and voltage than chalcogenides with higher molecular weight. Accordingly, the manganese oxide and vanadium oxide were used in commercial rechargeable coin cells using Li-Al alloy as negative electrode. In 1980s, a new series of intercalation compounds, Li_xMO_2 (M : Co, Ni, Mn) were proposed by Goodenough et al. as the cathode materials [8], which are

still the most important cathode in today's battery market. However, the lack of suitable materials for the negative electrode and the stable electrolyte in high voltage delayed the realization of rechargeable lithium ion battery. In mid-eighties, carbonaceous materials were recognized to be a suitable anode that can substitute with lithium metal due to the reversible lithium (de-)intercalation capability at low voltage [9, 10]. In 1991, Sony corporation commercialized C/LiCoO₂ cell, which can be considered as the major breakthrough in new practical battery system. At the same time, studies on spinel materials have led to the selection of LiMn₂O₄ as a competitive material [11]. Later, another important cathode olivine material, LiFePO₄ was proposed by Goodenough's group [12], which is actively studied all around the world until today. Finally, studies on positive materials moved almost completely from sulfides to oxides and three families of oxide containing lithium are now the most used or studied until today.

The Figure 1.2 shows schematic reaction of Li ion batteries composed of graphite anode, LiCoO₂ cathode and organic solvent containing lithium salt as the electrolyte. Lithium ions move from the negative electrode to the positive electrode during discharge, and back from the positive electrode to negative electrode when charging. The detailed reaction steps of discharge process can be described to:

- i. The Li⁺ ions diffuse from inside of anode to anode/electrolyte interface.
- ii. The Li⁺ ions migrate from anode/electrolyte interface to electrolyte.
- iii. The electrons are given to external circuit for neutralizing negative charges induced by deintercalation of Li⁺ ions.
- iv. Li⁺ ions move to cathode/electrolyte interface through the electrolyte.
- v. The Li⁺ ions migrate from cathode/electrolyte interface to cathode.
- vi. The Li⁺ ions diffuse through the interlayer pathway of CoO₆ framework.
- vii. Cathode accepts electrons from external circuit and the transition metal reduced to lower charge state.

The reverse steps undergo at the charge process. For the slight expansion and

shrinking without significant structural change during insertion and extraction of Li^+ ions at both of cathode and anode, the high reversibility can be achieved. In following contents, the main feature of several representative intercalation materials will be described.

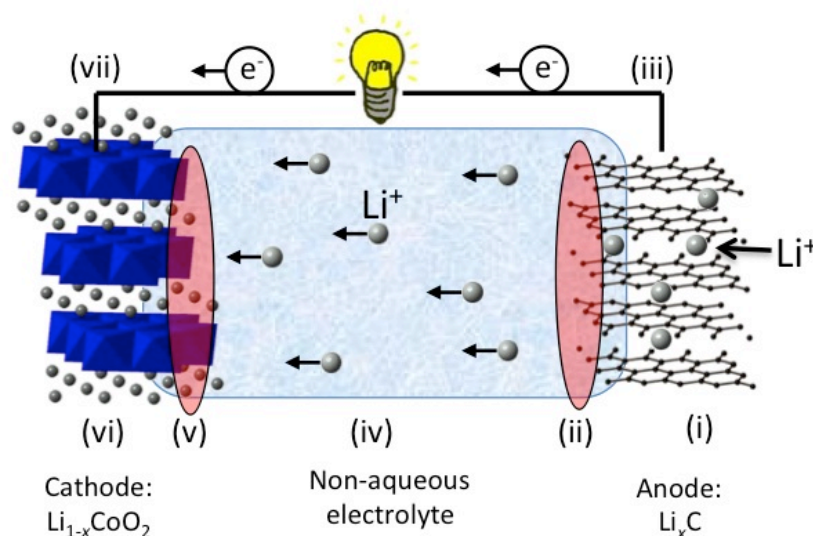


Figure 1.2 Schematic representation and operating principles of rechargeable lithium ion batteries in the discharge process. LiCoO_2 and graphite used as cathode and anode, respectively.

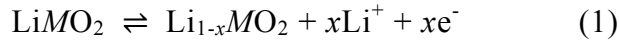
1.2 Intercalation compounds for lithium batteries

1.2.1 LiMO_2 (M : transition metal) layered rocksalt type compounds

1.2.1.1 Basic layered transition metal oxide

The layered rocksalt type compounds are represented by the formula LiMO_2 , where the M is typically an electrochemically active transition metal ions such as Co, Ni, V or Cr. The layered rock-salt, $\alpha\text{-NaFeO}_2$ structure has rhombohedral symmetry, $R\bar{3}m$. This structure is based on a close-packed network of oxygen atoms with the Li^+ and M^{3+} ions ordering on alternating (111) planes of cubic

rock-salt structure. As shown in Figure 1.3 (a), layered structure intercalation material provides a two-dimensional interstitial space, which can facilitate fast mobility of Li ion in the host materials. The following formula presents the electrochemical reaction taking place in a topotactic manner.



Among numerous layered materials, LiCoO_2 was the first material that was commercialized as a cathode for LIBs. LiCoO_2 crystal belongs the space group $R-3m$ with cell constants $a \approx 2.816 \text{ \AA}$ and $c \approx 14.08 \text{ \AA}$. The schematic view of the structure in Figure 1.3 (b) shows the “ABCABC” stacking of the “O-Li-O-Co-O-Li-O” triangular sheets [8]. In the charge-discharge process, the Li ion intercalates into or deintercalates from the van der Waals gap between CoO_2 layers reversibly. Some of the research focused on the phase transitions of Li_xCoO_2 as x varies from 0 to 1 [8, 13-15]. Reimers et al. reported that the coexistence of two hexagonal phases was observed for $0.75 \leq x \leq 0.93$ in Li_xCoO_2 . They also shown that a single-phase reaction took place and a monoclinic phase was observed at $x = 0.5$ [13]. This single-phase reaction is associated with phase changes from $R-3m$ to $C2/m$. At a higher delithiated state of $x \leq 0.25$, a two-phase reaction appears again, which can be explained in terms of the Jahn-Teller deformation of CoO_6 octahedra in a solid matrix [14]. Furthermore, CdI_2 type hexagonal phase was confirmed in the $0 \leq x \leq 0.2$ region using in-situ X-ray diffraction performed by synchrotron X-ray radiation [15, 16].

Although as high as 276 mAh g^{-1} of the theoretical capacity of LiCoO_2 can be delivered by complete delithiation, but at highly delithiated state, the layered structure of Li_xCoO_2 becomes unstable. Amatucci et al. pointed out that for voltages higher than 4.2 V, cobalt dissolution is the main reason of structural change and capacity fading [17]. Yazami et al also reported that the cell suffered irreversible loss of capacity and suppressed reversible reaction kinetics due to the

formation of some cubic spinel phase in the LiCoO_2 material at 4.7 V [18]. Therefore, the reversible capacity is restricted to 140 mAh g^{-1} ($0.5 \leq x \leq 1$ in Li_xCoO_2) in practice. It should be noted that, although excellent reversible capacity of LiCoO_2 can be obtained, thermal stability concerns of $\text{Li}_{1-x}\text{CoO}_2$ still exist, which may lead to severe safety issues. The main research is focused on further enhancement of the thermal stability and cyclability by coating Al_2O_3 or AlPO_4 [19, 20]. Recently, to meet demand of high power performance of new generation batteries, the high rate charge-discharge property of nanosized LiCoO_2 bulk and thin film are actively studied [21-23].

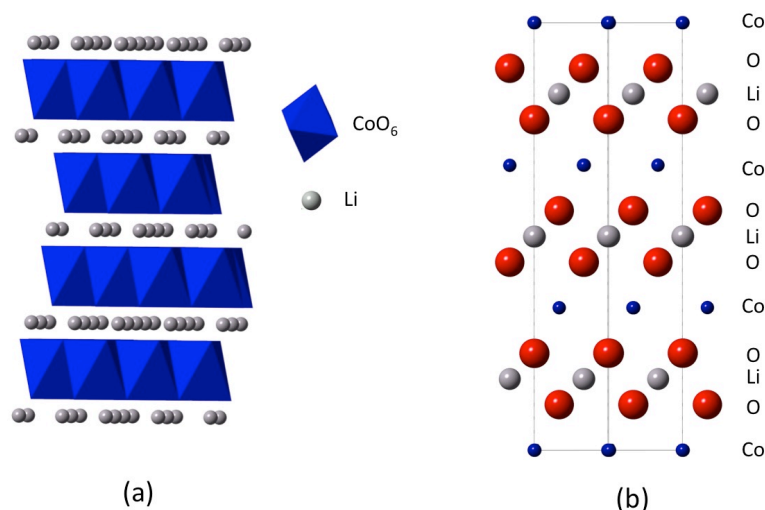


Figure 1.3 Schematic diagram of the layered LiCoO_2 structure showing (a) two-dimensional CoO_6 octahedra layers and interlayer Li ions and (b) ABCABC stacking of O-Li-O-Co-O-Li-O layers.

Unquestionably, LiCoO_2 is an excellent cathode material due to its high discharge voltage and good cyclability. However, it is desirable that a cheaper cathode material with lower environmental load is exchanged with LiCoO_2 due its toxicity, high cost and poor resources of cobalt. LiNiO_2 presents an advantage over LiCoO_2 because of the lower cost and toxicity of nickel than cobalt. The structure features of LiNiO_2 are exactly the same as those of LiCoO_2 [24-28].

However, it has a several disadvantages:

- i. The stoichiometric LiNiO_2 is difficult to obtain, because the high-temperature treatment of LiNiO_2 causes structure change from LiNiO_2 to $\text{Li}_{1-x}\text{Ni}_{1+x}\text{O}_2$, which has a partially disordered cation distribution at the Li sites [29].
- ii. Multiple phase transformation of LiNiO_2 during electrochemical cycling results in structural instability [30].
- iii. The removal of half the lithium from LiNiO_2 results in a metastable-layered structure $\text{Li}_{0.5}\text{NiO}_2$, and transforms to the spinel structure of $\text{Li}[\text{Ni}_2]\text{O}_4$ [27]. The low conductivity and high stability of the spinel phase suffers the cyclability of the LiNiO_2 .
- iv. Safety problem of LiNiO_2 is resulting from exothermic release of oxygen in the highly delithiated state [31].

For these reasons, LiNiO_2 is not practically used as the cathode material of LIB at present. In order to improve the electrochemical stability, substitutional metal ions are incorporated into nickel ion layer. The composition of $\text{LiCo}_{0.8}\text{Ni}_{0.2}\text{O}_2$ [32-34] has been researched widely until now, because this material is not only stable and less likely to lose oxygen than pure nickel oxide, and also favorable for the practical aspect owing to the low cost with small substitution content of cobalt. Delmas et al. reported that upon intercalation of $\text{Li}_{1-x}\text{Ni}_{0.8}\text{Co}_{0.2}\text{O}_2$ ($x \leq 0.5$), there is no phase transition during charge and discharge processes, but only a slight variation in cell parameter. [33].

1.2.1.2 $\text{LiNi}_{1/3}\text{Co}_{1/3}\text{Mn}_{1/3}\text{O}_2$

$\text{LiNi}_{1/3}\text{Co}_{1/3}\text{Mn}_{1/3}\text{O}_2$ is a new cathode material that containing Ni^{2+} , Co^{3+} and Mn^{4+} [35-37]. $\text{LiNi}_{1/3}\text{Co}_{1/3}\text{Mn}_{1/3}\text{O}_2$ have a $[\sqrt{3} \times \sqrt{3}]R30^\circ$ -type super-lattice based on an α - NaFeO_2 -type structure that consisted of homogeneously distributed Co^{3+} , Ni^{2+} , Mn^{4+} ions (Figure 1.4). $\text{LiNi}_{1/3}\text{Co}_{1/3}\text{Mn}_{1/3}\text{O}_2$ shows excellent cycle life and high capacity due to the unique electronic structure and small change in lattice volume. Yabuuchi et al. [35] reported that

LiNi_{1/3}Co_{1/3}Mn_{1/3}O₂ shows about 200 mAh g⁻¹ of rechargeable capacity between voltages of 2.5 ~ 4.6 V with negligible capacity loss in 30 cycles. In addition, the exothermic reaction of □_{0.88}Li_{0.12}Ni_{1/3}Co_{1/3}Mn_{1/3}O₂ is much milder than that of LiNiO₂ or LiCoO₂ (□ means Li ion vacancy). However, Zhou et al. reported that when delithiated Li_{1-x}Ni_{1/3}Co_{1/3}Mn_{1/3}O₂ was exposed to electrolyte near 260°C, the reaction rate accelerated dramatically with temperature [38]. They also reported that the thermal stability is improved by Al substitution. Ascribe to the lower cost than LiCoO₂ and higher energy density than LiFePO₄ and LiMn₂O₄, LiNi_{1/3}Co_{1/3-y}Mn_{1/3}Al_yO₂ is well suitable for use in large scale storage batteries [39, 40]. Therefore, the solid solution system of LiNi_{1/3}Co_{1/3}Mn_{1/3}O₂ is used as next-generation of cathode after LiCoO₂.

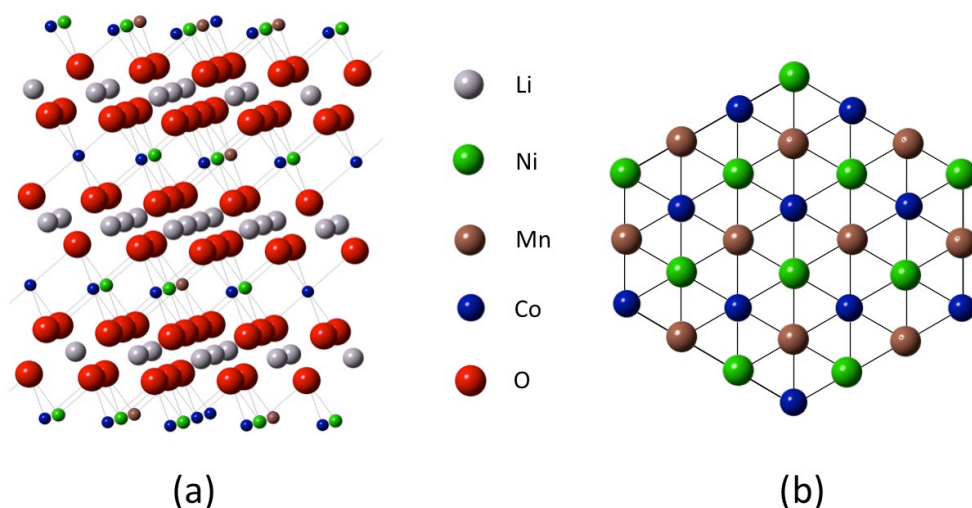


Figure 1.4 A schematic illustration on the model crystal of (a) LiCo_{1/3}Ni_{1/3}Mn_{1/3}O₂ based on the triangular basal net of sites in the α -NaFeO₂-type structure and (b) a super-structural [Co_{1/3}Ni_{1/3}Mn_{1/3}] layer of [$\sqrt{3}\times\sqrt{3}$]R30°-type.

1.2.1.3 Li-excess Mn-based layered oxide Li₂MnO₃

Li₂MnO₃ has a layered monoclinic structure with C_{2/m} symmetry. Li₂MnO₃ contains alternating lithium layered and layers consisting of excess lithium and manganese with mole ratio of Li:Mn = 1:2, which can be represented as

$\text{Li}[\text{Li}_{1/3}\text{Mn}_{2/3}]\text{O}_2$ as shown in Figure 1.5 (a) and (b). Compared with LiCoO_2 , the complex arrangement of the Li and Mn ion in the Li-Mn layer generates superlattice diffractions in XRD pattern (Figure 1.5 c). Li_2MnO_3 is electrochemically inactive due to the fully oxidized Mn^{4+} in metal oxide layer. However, it was attracted much interest for high energy density and inexpensive cathode material since some groups proposed that Li_2MnO_3 can be activated by either chemical [41] or electrochemical method [42, 43]. The Li-excess oxides can present very high rechargeable capacity more than 250 mAh g^{-1} [44, 45], but Li_2MnO_3 encounter the disadvantages of large irreversible capacity loss and poor rate capability. The irreversible capacity loss mainly takes place at the first charge process of the long oxygen release plateau, which is attributable either to the diffusion of transition metal into the lithium sites in the transition metal layer or the instability for lithium reinsertion into the transition metal layer [46]. The reason for the poor capability is still not clear. Researches on the cycling mechanism of Li-excess Mn-based layered oxides is under way. Wide approaches in researches have been devoted to overcome the irreversible capacity and the inferior rate capability of Li-excess Mn-based layered oxide, which are hindering the commercial application. Recently, it was proved that introducing Ni or Co cation into the Li-excess layered oxide could significantly enhance the reversible capacity and efficiency [46, 47]. Thackeray et al. proposed Li-excess oxide of $\text{Li}_{1.2}\text{Mn}_{0.524}\text{Ni}_{0.176}\text{Co}_{0.1}\text{O}_2$ was incorporated with a $\text{Li}_4\text{Ti}_5\text{O}_{12}$ anode to a full cell, and delivered near 300 mAh g^{-1} in the voltage range of $3.1 \sim 0.5 \text{ V}$ [48]. It is found that surface modification with AlF_3 [49], Al_2O_3 [50] and Li-N-PO_4 [51] is another effective way to reduce the irreversible capacity loss and enhance the cyclic and rate performance.

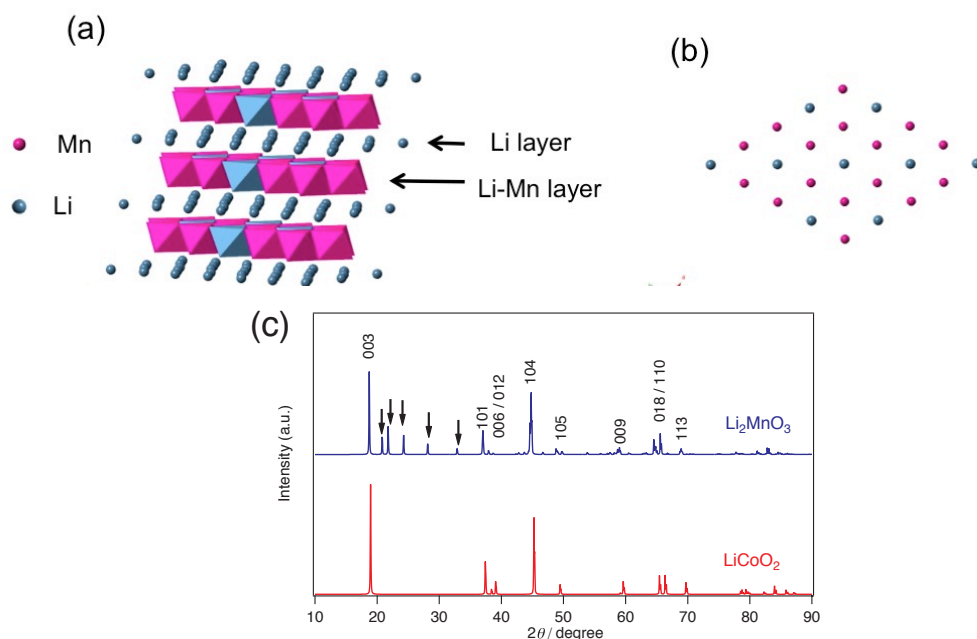


Figure 1.5 A schematic illustration on the model crystal of (a) Li_2MnO_3 (monoclinic structure, $C2/m$ symmetry) and (b) the Li-Mn layer. (c) The XRD patterns of layered LiCoO_2 and Li_2MnO_3 . The arrows denote diffractions of superlattice.

1.2.2 LiM_2O_4 (M : transition metal) spinel type compounds

LiMn_2O_4 crystalline with a spinel structure belongs to the $Fd-3m$ space group with cubic lattice parameter $a = 8.239 \text{ \AA}$ [11]. The cubic spinel LiMn_2O_4 structure is described with the Li cations on the $8a$, Mn on the $16d$ sites, and the oxygen ions on the $32e$ sites. Half of the octahedral interstices are occupied by the Mn ions forming three-dimensional framework of edge-sharing octahedra and Li ion occupies tetrahedral sites, which share common faces with four neighboring empty octahedral sites at the $16c$ position. The lithium ion diffuses through the three-dimensional network path of $16c-8a-16c$. The ideal cubic unit cell is shown in Figure 1.6. The Li insertion/deinsertion of $\text{Li}_x\text{Mn}_2\text{O}_4$ ($0 \leq x \leq 1$) during the charge-discharge reaction can be written as:

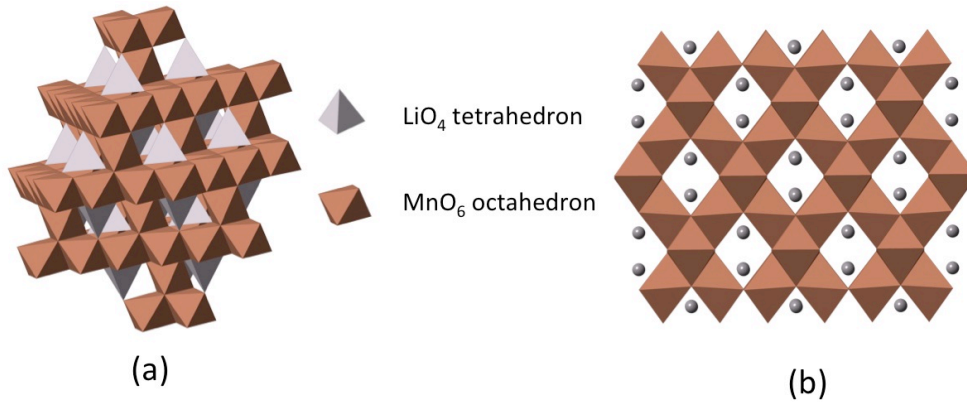
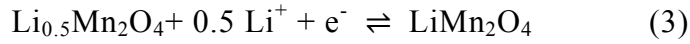
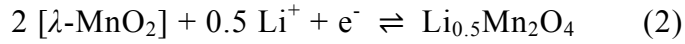


Figure 1.6 (a) LiMn_2O_4 cubic spinel type structure and (b) the cross-sectional view of 110 plane.

For many years, LiMn_2O_4 has been the object of intense worldwide research [52-56] because it has several attractive advantages: (i) much lower cost of Mn than Ni or Co, (ii) a larger thermal stability domain especially when over-charged, (iii) a higher discharge voltage than other cathode materials and (iv) lower load on environment. However, the fast fading of capacity is the main obstacle for the practice application, especially with increasing temperature. The origin of the capacity fading with cycling has been investigated in a large number of studies and several phenomena have been proposed to explain it [57-59]:

- i. Instability of the organic-based electrolyte at the high voltages reached when charging cells.
- ii. Slow dissolution of the Mn^{2+} in to the electrolyte according to the reaction:



- iii. The onset of Jahn-Teller effect in deeply discharged $\text{Li}_x\text{Mn}_2\text{O}_4$ ($x \geq 1$)

electrode.

To stabilize the structure during charge-discharge cycling, over-lithiated phase $\text{Li}_{1+x}\text{Mn}_{2-x}\text{O}_4$ has been proposed [57, 60-62]. Although the lower capacities as the ratio of Li/Mn increasing, the capacity fading is strongly reduced even at 60°C. Xia et al. explained that vacancy- and lithium-rich spinel having a small unit cell in which a homogeneous insertion/extraction reaction can proceed over the entire intercalation region [63]. Besides, a lot of research works, such as partial substitution of cation [64, 65], using a polymer electrolyte [66] and surface modification [62] is still going on to reduce Mn ion dissolution and improve the behavior of LiMn_2O_4 . Recently, it is found that surface coating of LiMn_2O_4 suppresses Mn ion dissolution and LiMn_2O_4 is practically used as the cathode materials for the battery in the electric vehicle.

1.2.3 LiMPO_4 (*M*: transition metal) olivine type compounds

The olivine structure of LiFePO_4 belongs to the *Pnma* space group with orthorhombic unit cell. It built up of PO_4^{3-} tetrahedral, with the Fe^{2+} occupying corner-shared octahedral positions, and the Li ions locate in chains of edge-shared octahedra. The model structure of LiFePO_4 is illustrated in Figure 1.7.

Since the proposal of LiFePO_4 as a potential candidate for lithium insertion by Goodenough et al. at 1997 [12], considerable interest has been generated because of its attractive features [67-69]:

- i. High theoretical specific capacity (170 mAh g^{-1}) and high operating voltage (about 3.5 V) for $\text{Fe}^{3+}/\text{Fe}^{2+}$ couple.
- ii. Much lower cost and environmental impact of Fe than Co, Ni, Mn.
- iii. Intrinsic thermal safety and excellent cyclability associated with phosphate.

One major disadvantage of LiFePO_4 is its extremely low electrical conductivity ($10^{-9} \sim 10^{-10} \text{ S cm}^{-1}$) due to the isolated Fe ion in the olivine structure.

However, this drawback has been overcome through various approaches, including carbon coating [70, 71] and diminishing particle size to nanometer level [72-74]. For example, the nanocomposited LiFePO₄ can reach the theoretical capacity of 170 mAh g⁻¹ with high power capability.

On the other hand, the reaction mechanism of LiFePO₄ cathode material actively studied by worldwide scientists. Different from two-dimensional diffusion in layered LiCoO₂ and three-dimensional diffusion in spinel LiMn₂O₄, it is believed that Li diffuses one-dimensional path along [010] channel during charge-discharge cycling [75, 76]. Two-phase reaction that called 'core-shell reaction' [77, 78] has been widely applied because of the extremely flat charge-discharge plateau. Yamada et al. [78] reported that intermediate Li_xFePO₄ ($\alpha < x < 1 - \beta$) region consists of Li _{α} FePO₄ and Li_{1- β} FePO₄ phase, where α and β are in the range of 0.03~0.04. Contrary to this model, Gibot et al. reported that the extremely fine LiFePO₄ nanoparticles (40 nm) formed by low temperature (108°C) precipitation process exhibit characteristic of single-phase behavior. The performance of LiFePO₄ with the particle size of 40 nm was competed favorably with usual 140 nm carbon-coated LiFePO₄ particles prepared at 500°C [69].

Now, LiFePO₄ is the most attractive candidate for cathode material of large-scale storage system ascribe to excellent security performance and low cost. During the 2008 Beijing Olympic Game, electric buses are the first in Beijing to use an advanced lithium ion electric battery with LiFePO₄ cathode. Each bus can carry 80 persons per trip and reach 80 km/h. With batteries fully charged, it can run 130 km without recharging [79].

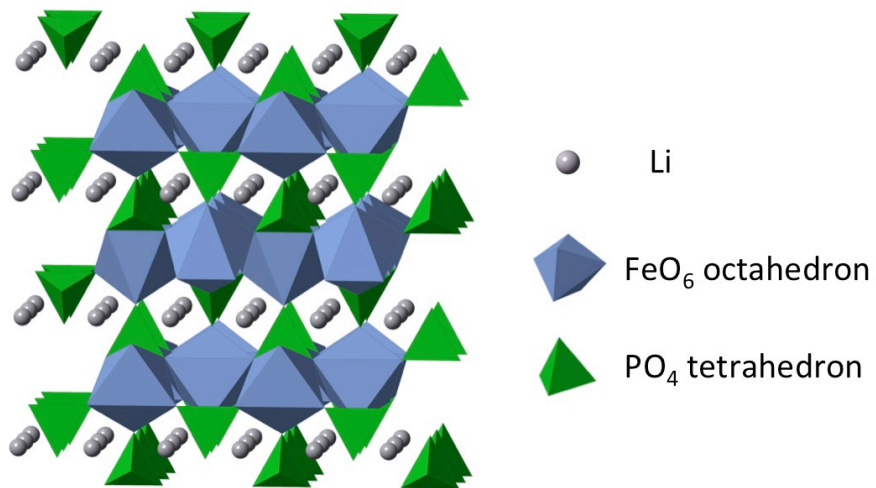


Figure 1.7 Schematic illustration of LiFePO_4 olivine type structure.

1.3 Nanostructured materials for lithium batteries

As stated in former paragraph, lithium secondary batteries are one of the great successes in modern electrochemical devices [1, 80]. They have been the dominant backup power sources for mobile devices such as cellular phones and laptop computers. Recently, establishment of a low carbon society, which is based on clean and sustainable energy, has gradually become a worldwide topic. Development of electric vehicle (EV) and hybrid electric vehicle (HEV) plays a key role in reducing CO₂ emission and addressing the crisis of fossil energy source exhaustion. Besides, effective energy storage technology of the renewable energy such as wind or solar power is also very important. But the generated power varies by time and weather. For the temporary stage of these electric power, application targets of lithium batteries are expanding from consumer electronic device to large-scale electric vehicles and energy storage systems to avoid the problems of exhaustion of fossil fuel and global warming. To satisfy the needs of new applications, batteries are required to be enhanced in terms of performance, especially high power density and high energy density. The lithium-ion battery R&D roadmap entitled “Battery RM 2010” has been drawn up by New Energy and Industrial Technology Development Organization (NEDO). For use as electric vehicle battery, the roadmap sets a target of improving specific power density from 100 Wh kg⁻¹ to 500 Wh kg⁻¹ and reducing the cost to 1/15 by 2030. In present stage, the intercalation system is going to reach the limits of potential energy density. Hence the new materials and technologies are required for remarkable improvement in energy density and cost for lithium batteries. One of the effective approaches is developing nanostructured electrode for lithium batteries that can be obtained with simple procedure.

On the other hand, lithium ion thin film batteries attracted much interest for the application of the back up power sources of microelectronic devices and micromechanics such as smart card, sensor technology, computer memory chip and so on. Figure 1.8 shows the schematic illustration of the thin film electrode.

The thin film electrodes are used to fabricate the battery without using polymeric binder and conductive additive, so that the electronic contact between active material and current collector should be better than bulk based electrode composite. Therefore, thin film batteries have advantages in power density, and their very small and very thin size helps to reduce the physical size of the sensor or device using the battery. To pursue further improvement in power density of thin film batteries, application of nanostructured cathode was proposed in attempt to raise high rate discharge performance.

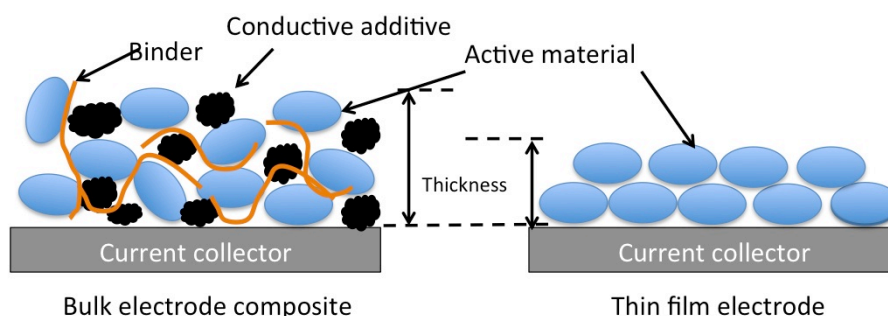


Figure 1.8 The schematic illustration of the bulk electrode composite and thin film electrode.

Nanostructured materials have attracted great interest in recent years because of its unique physical and electrochemical features generated from the combination of bulk and surface properties [81, 82]. It allows us to design electrode materials and optimize structures from molecule unit for achieving desired properties and performance. Hence, nanostructured materials are increasingly coming to be important for electrochemical energy storage. Several advantages of using nanostructured electrode for lithium batteries are listed as follows:

1. *Large surface area (higher electrode/electrolyte contact area) and short path length of electron and Li^+ transport, that leads to higher capacity and higher power density (Figure 1.9).*

This is the most important point for using nanostructured electrode to

improve power density and capacity. High charge-discharge rate capability depends on the Li ion diffusion length and the chemical Li ion diffusion coefficient, so that the active materials with large particle size are not suitable for high power batteries. For nanostructured electrodes, their higher surface area and shorter Li ion diffusion length due to small particle size should contribute to the higher rate capability. In the case of layered LiCoO_2 , Li^+ diffusion coefficient in cathode materials is ca. $10^{-11.6} \text{ cm}^2/\text{s}$. Based on this value, the lithium-ion diffusion length in a second is below 15 nm. Okubo et al. have studied nanosize effect on high-rate Li intercalation carefully in LiCoO_2 cathode synthesized by hydrothermal reaction [21, 83, 84]. They reported that LiCoO_2 nanoparticle with the size of 17 nm showed reversible charge-discharge performance even at as high discharge rate as 100 C. (1 C-rate means the discharge current that will discharge the entire capacity in 1 hour.) In this study, nanostructured cathode thin films with high surface area and short Li ion diffusion length are prepared to improve the high rate discharge performance of the thin film battery system.

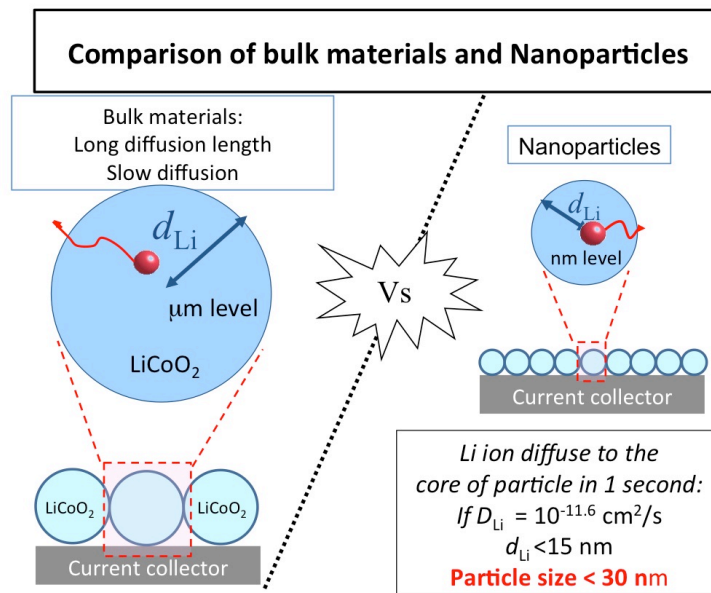


Figure 1.9 Schematic illustration for effect of nanoparticle.

2. *New reaction mechanism different with bulk materials could be obtained for nanoelectrode.*

As mentioned in 1.2.3, Gibot et al. reported that the extremely fine LiFePO₄ nanoparticles (40 nm) exhibit characteristic of single-phase behavior, which is different from two-phase core-shell model of bulk LiFePO₄ [69]. In the field of negative electrode, Tarascon et al. proposed that nanoparticles of transition-metal oxides (MO, where M is Co, Ni, Cu or Fe) demonstrate much higher electrochemical capacities and better capacity retention for long cycle [85, 86]. The reaction mechanism differs from the classical Li insertion/deinsertion for Li-alloying process, and involves the formation and decomposition of Li₂O, accompanying the reduction and oxidation of metal nanoparticles. This electrode reaction formula of this “conversion reaction” of transition metal oxide MO is shown as eq. (5):



Since first report by Tarascon et al. at 2000, the conversion reaction has been widely investigated not only for the 3d transition metal oxides, but also for transition metal fluorides [87, 88], sulfides [89, 90] and nitrides [91] as promising anodes for lithium batteries. Therefore, the new reaction mechanisms that are taking advantage of nanostructured materials will directly associate with fundamental advances in new generations of energy storage devices.

3. *Phase transformation could be suppressed during lithium insertion/deinsertion for nanoelectrode (Figure 1.10) .*

Iron based materials are excellent candidates for next generation electrode of lithium battery for its low cost and low toxicity. However, bulk iron oxides suffer from low specific capacity and poor reversibility. For example, bulk γ -Fe₂O₃ (1 μ m particle size) only shows discharge capacity of 50 mAh g⁻¹ due to the irreversible structure change from spinel to stable rock-salt structure during charge-discharge process induced by Li insertion. However, γ -Fe₂O₃ nanoparticle

(7 nm particle size) can effectively suppress the structure transformation and derive reversible capacity of 230 mAh g^{-1} . Moreover, the capacity retention also significantly improved by downsizing the of particle to nano size level for other type iron oxides such as $\alpha\text{-Fe}_2\text{O}_3$ [92] and Fe_3O_4 . [93, 94]. It is worth trying to develop new nanostructured bulk martials for high energy density cathode of large-scale energy storage system.

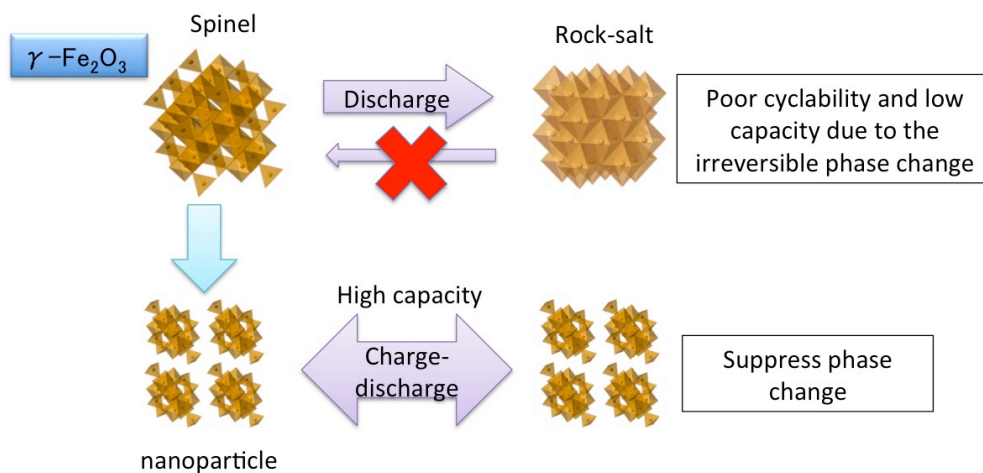


Figure 1.10 Schematic illustration for effect of nanoparticle

However, there are several hurdles to get over before make most use of the merits of nano-materials. For the nanostructured bulk materials, uniform and well-dispersed nanoparticles hold the key to excellent electrochemical performance of nanoelectrode. But these nanoparticles trend to aggregate together or promote crystal growth in annealing process, which directly harm the functionality of nanoparticles. To prevent undesirable reaction and maintain the shape of nanostructure, special synthesis processes and expensive chemicals are applied. For example, nano-sized $\gamma\text{-Fe}_2\text{O}_3$ was synthesized by mild oxidation of $\text{Fe}(\text{CO})_5$, which needs five-step complicated reaction and many reagents such as $\text{Fe}(\text{CO})_5$, octylether, oleic acid and so on [95, 96].

4. Nanosize compound for thin film fabrication

To realize the super high rate thin film battery, downsizing the compound

that constitutes the thin film is very important. But for the preparation of thin film cathode, it is difficult to obtain uniform thin film that composed of nanosize particle using novel synthesis method like sol-gel [55], electrostatic spray deposition (ESD) [97, 98] and aerosol flame deposition [99]. To fabricate uniform nanostructured thin film, physical vapor deposition (PVD) such as pulsed laser deposition (PLD) and r.f. sputtering method are employed. Matsumura et al. reported that LiMn_2O_4 thin film synthesized by PLD method consisted of uniform nanoparticles (10~20 nm particle size) showed charge-discharge ability even at over 500 C-rate [100]. However, the synthesis method cost very high due to the highly vacuum condition and UV laser use hinder these method from industrial application. Therefore, the use of PLD method is mainly used for constructing nanostructured ideal epitaxial thin films with low surface roughness, small grain boundary and ordered orientation to study structural characterization of electrode/electrolyte interface [101-103].

1.4 Nanomaterials derived from layered compounds

From above points of view, nanostructured electrode materials have been proved to be one of the most helpful strategies for the development of lithium batteries. Therefore, research and development have to focus on improving upon materials demerits. Firstly, the nanostructured materials must preserve the stability of the original feature not only the size but also the shape. Secondly, simple and inexpensive preparation process is desirable to obtain nanostructured materials. Layered compounds are promising precursor that can derive the expected nanostructured materials. (i) Most of layered compound precursors could be prepared by simple synthesis process such as co-precipitation method, sol-gel method and sintering process without any special equipment. (ii) Under given operating condition, layered compounds can be completely exfoliated to two-dimensional thin layer with the thickness of one or several molecular level, called “nanosheet”. (iii) Layered double hydroxide (LDH), a kind of the layered

hydroxide compound, is easy to form well-dispersed metal oxide nanoparticle by dehydration reaction at relatively low calcination temperature.

1.4.1 Layered double hydroxides (LDHs)

Layered double hydroxides (LDHs) are a class of ionic lamellar compounds made up of positively charged brucite-like layers with an interlayer region containing charge compensating anions and solvation molecules [104-106]. The metal cations occupy the centers of edge sharing octahedra, whose vertexes contain hydroxide ions that connect to form infinite 2D sheets. The most widely studied LDHs contain both divalent and trivalent metal cations, a composition formula for these LDHs can be written as $[M^{II}_{1-x}M^{III}_x(OH)_2] (A^{m-})_{x/m}$ where M^{II} : Ni^{2+} , Mg^{2+} , Zn^{2+} , Cu^{2+} , *etc.*, M^{III} : Fe^{3+} , Al^{3+} , V^{3+} , Co^{3+} *etc.*, A^{m-} : NO_3^- , Cl^- , CO_3^{2-} , *etc.* LDHs have received considerable attention due to its technological importance. Tungstate-exchanged Mg-Al LDH catalyzes oxidative bromination and bromide-assisted epoxidation reactions in a selective manner, and the catalyst is over 100 times more active than its homogeneous analogue [107]. In medical material field, the interlayer anion exchangeable capability of LDHs also meets the requirement of drug delivery hosts [108, 109]. Choy et al. have reported that nucleoside monophosphates and DNA can be intercalated into LDH by an ion-exchange process, in an attempt to develop possible applications of bio-LDH hybrids as gene or drug delivery carriers [110]. In addition, nanostructured materials also can be obtained starting from the LDHs through two routes. Firstly, delamination of LDHs produces positively charged thin platelets (nanosheet) with a thickness of a few atomic layers, which can be used as building units for making new designed organic-inorganic [111, 112] or inorganic-inorganic [113, 114] nanocomposites. Secondly, calcination of LDHs at low temperature induces dehydration and gas emission, and finally forms multiple metal oxide nanoparticles, which preserve the metal composition of former LDHs. Some cation vacancy sites are generated during anion emission for

the charge neutralization of the solid, because trivalent cations are partially substituted to the divalent cations: $M^{2+}_x M^{m+}_y \square_{1-x-y} O$, where \square indicates cation vacancy as shown in Figure 1.11. The multiple metal oxides form the homogeneous solid solution in the framework of M^{II} oxide with extremely small particle size and large specific surface area [115-117]. Therefore, the low cost and heterogeneous character of LDHs, together with its ability to obtain nanosheets and nanoparticles efficiently under mild conditions, raise the prospect for the able development of a clean and efficient industrial route to preparation of nanostructured materials.

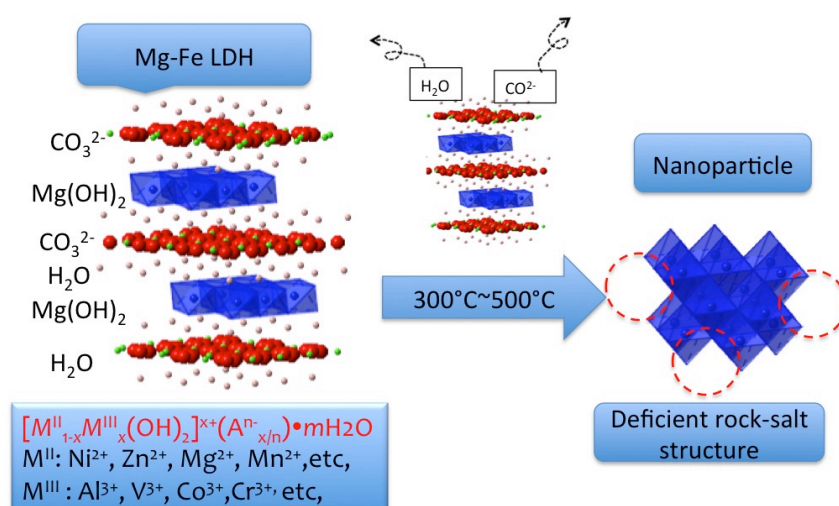


Figure 1.11 The layered structure of LDHs and multiple metal oxide derived by dehydration reaction.

1.4.2 Nanosheet

Two-dimensional (2D) nanosheets, which possess atomic or molecular thickness and infinite planar dimensions, are regarded as the thinnest functional nanomaterials [118]. The nanosheets correspond to a single layer, or fundamental unit of layered structure (Figure 1.12). Accordingly their thickness is extremely small, 0.5~3 nm, being dependent on original layered materials. Pioneering studies in nanosheet is from the successful delamination of layered titanate into

single TiO₂ nanosheet by Sasaki et al. in the 1990s [119]. The nanosheets are obtained by splitting layered compounds into individual layers through soft-chemical delamination. Usually, layered compounds with strong in-plane bonds and weak coupling between layers are preferred characteristics for the precursor. Recent advances in various delamination techniques have produced 2D nanosheets of various materials including graphene [120], metal oxides [121, 122], metal hydroxide [123, 124]. These nanosheets attracted considerable attention due to their unique features such as highly two-dimensional structure, ultrathin thickness, well-defined composition, and highly crystalline nature. Moreover, weak charge originated guest bulky ions prevents the nanosheet from aggregating together. These features help us to design the functional nanomaterials that possess the desired properties using nanosheet as a basic building block. For example, unilamellar seed layer consist of nanosheets with a molecular-level thickness of around 1 nm, was introduced onto glass substrate surface by langmuir-blodgett (LB) deposition. The ultimately thin seed layer acting as flexible monocrystal substrate, promoted orientation crystal growth on the surface [125, 126]. Not only nanosheet monolayer, but also multiple layer nanosheet thin film including binary nanosheet system or sandwich system can be assembled by layer-by-layer (LBL) or flocculation methods [113, 127, 128]. Furthermore, the well-ordered nanosheet multilayer provides the base of Li containing nanoparticles for subsequent treatment like hydrothermal and thermic reaction. Accordingly, nanosheet derived by layered compounds is expected to open up new avenue that can develop nanoelectrode for lithium batteries.

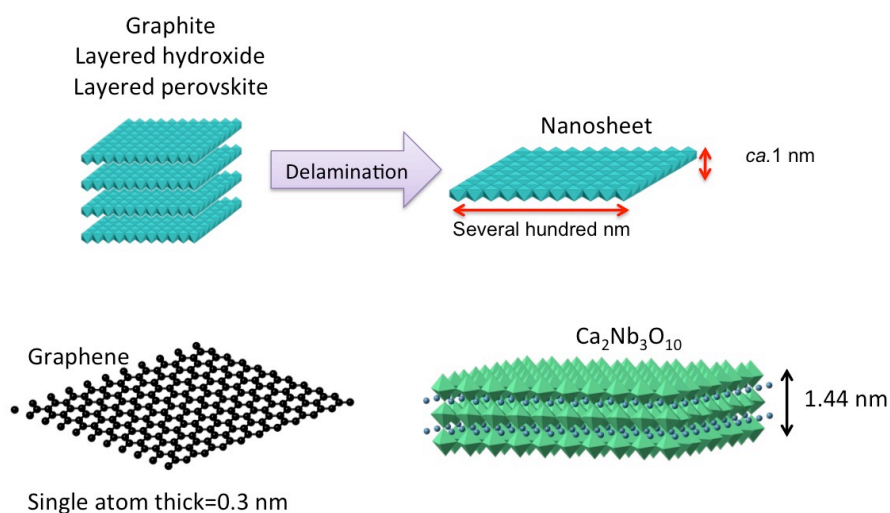


Figure 1.12 2D nanosheets: graphene and $\text{Ca}_2\text{Nb}_3\text{O}_{10}$ single layer

1.4.3 Multiple metal oxide nanoparticles

For the traditional intercalation materials, it is difficult to gain significant capacity due to the strict limitation of the lithium insertion site. In contrast, metal oxide nanoparticles show much higher capacity ascribed to different reaction mechanism, wider range of valence state ($\text{M}^n/\text{M}^{n+x}$, $x \geq 1$) or lighter molecular weight. Such approaches are feasible with Fe- or V-based metal oxides. As high as 250 mAh/g of capacity is delivered by Fe_2O_3 [95] and V_2O_5 [129]. However, further improvement of specific discharge capacity and cyclability is limited by single-metal system. To develop binary system or multiple metal system may solve this problem, because different reaction mechanism and stabilized crystal structure can be generated by these approaches. Matsumura et al. reported that 300 mAh g^{-1} of capacity can be obtained by $\alpha\text{-Fe}_2\text{O}_3\text{-SnO}_2$ binary system by surface and intercalation reaction [130]. Hibino et al. reported that the cyclability of CoV_3O_8 , V_2O_5 -based composite was significantly improved than V_2O_5 . These binary or multiple metal oxide systems will enable further development of metal oxide nanoparticles for lithium batteries.

1.5 Purpose of study

Improving power performance and energy density is the main issue for lithium batteries to be associated with practical using in large-scale application. Nanostructured material is one of the most useful strategies to develop electrochemical performance of electrode for new generation lithium batteries. However, the nanostructured electrode is still out of industrial application due to the potentially complicated synthesis process and high fabrication cost. The purpose of the study is to prepare nanostructured electrode with excellent electrochemical properties starting from layered compounds by easy and inexpensive synthesis method. My present study consists of following two parts.

- i. Preparation of nanostructured thin film by assembling nanosheet.

As described in above section (1.4.2), nanosheets derived from layered compounds show very interesting features. However, most of researches focused only on assembling technique and physical and electrical properties of nanosheets. In order to maximize the power performance of cathode, I attempted to develop two-step synthesis method that based on nanosheet restacking technique and subsequent lithiation treatment.

- ii. Synthesis of multiple metal oxide nanoparticle and investigation on reaction mechanism.

The multiple metal oxide nanoparticles are easily obtained by calcination of LDHs. However, the electrochemical performance of multiple metal oxide nanoparticles is strongly affected by the metal-composition and detail calcination condition. In order to develop multiple metal oxide system with high rechargeable capacity, optimization of the metal-composition and investigation on reaction mechanism base on the result of structural and electrochemical analysis have done.

The results in the present study are summarized as follows.

In chapter 2, LiCoO_2 thin films consisted of nanosize particles were synthesized on Au substrates by nanosheet restacking method and subsequent

hydrothermal reaction. The grain size of LiCoO_2 films estimated by XRD reflection was about 15 nm. High rate capability of the LiCoO_2 film at 400 C is confirmed by the small grain size and large surface area of LiCoO_2 thin film with nano size particles.

In chapter 3, LiCoO_2 consists of nano-particles was successfully coated on the surface of carbon powder by the electrostatic self-assembly deposition method and the hydrothermal treatment via the nanosheet deposition method. LiCoO_2 coated on acetylene black powder showed a high rate charge-discharge capability due to the high electronic conduction between LiCoO_2 and acetylene black powder.

In chapter 4, The LiMn_2O_4 thin films composed of nanoparticles were synthesized by sintering electrodeposited Mn_3O_4 precursor on the Au substrate. The LiMn_2O_4 film showed superior rate performance and cyclability because of good electric contact with substrate and high lithium diffusion coefficient.

In chapter 5, Mg-Fe, Ni-Fe, Ni-V multiple metal oxide nanoparticles were synthesized by calcination of the LDH precursors. These multiple metal oxides showed very high reversible charge-discharge capacity and good capacity retention. The result of using ex-situ X-ray diffraction and AC-impedance measurements indicated that intercalation and surface reaction reversibly occurs without remarkable structural change of the host.

These results reveal that using layered compounds precursors as starting materials is a promising method to synthesize nanostructured electrodes that possess excellent electrochemical properties for lithium batteries.

Reference

- [1]J.M. Tarascon, M. Armand, *Nature* 414 (2001) 359.
- [2]M.S. Whittingham, *Prog. Solid State Chem.* 12 (1978) 41.
- [3]M.S. Whittingham, *J. Electrochem. Soc.* 123 (1976) 315.
- [4]M.S. Whittingham, *Science (New York, N.Y.)* 192 (1976) 1126.
- [5]J.O. Besenhard, R. Schöllhorn, *J. Electrochem. Soc.* 124 (1977) 968.
- [6]D.W. Murphy, P.A. Christian, F.J. DiSalvo, J.N. Carides, *J. Electrochem. Soc.* 126 (1979) 497.
- [7]S. Turner, P.R. Buseck, *Science* 203 (1979) 456.
- [8]K. Mizushima, P.C. Jones, P.J. Wiseman, J.B. Goodenough, *Mater. Res. Bull.* 15 (1980) 783.
- [9]M. Mohri, N. Yanagisawa, Y. Tajima, H. Tanaka, T. Mitate, S. Nakajima, M. Yoshida, Y. Yoshimoto, T. Suzuki, H. Wada, *J. Power Sources* 26 (1989) 545.
- [10]R. Kanno, Y. Takeda, T. Ichikawa, K. Nakanishi, O. Yamamoto, *J. Power Sources* 26 (1989) 535.
- [11]M.M. Thackeray, W.I.F. David, P.G. Bruce, J.B. Goodenough, *Mater. Res. Bull.* 18 (1983) 461.
- [12]A.K. Padhi, K.S. Nanjundaswamy, J.B. Goodenough, *J. Electrochem. Soc.* 144 (1997) 1188.
- [13]J.N. Reimers, J.R. Dahn, *J. Electrochem. Soc.* 139 (1992) 2091.
- [14]T. Ohzuku, A. Ueda, *J. Electrochem. Soc.* 141 (1994) 2972.
- [15]X.Q. Yang, X. Sun, J. McBreen, *Electrochem. Commun.* 2 (2000) 100.
- [16]G.G. Amatucci, J.M. Tarascon, L.C. Klein, *J. Electrochem. Soc.* 143 (1996) 1114.
- [17]G.G. Amatucci, J.M. Tarascon, L.C. Klein, *Solid State Ionics* 83 (1996) 167.
- [18]R. Yazami, Y. Ozawa, H. Gabrisch, B. Fultz, *Electrochim. Acta* 50 (2004) 385.
- [19]G.-K. Fey, J.-G. Chen, T.P. Kumar, *J. Appl. Electrochem.* 35 (2005)

177.

[20]B. Kim, J.-G. Lee, M. Choi, J. Cho, B. Park, *J. Power Sources* 126 (2004) 190.

[21]M. Okubo, J. Kim, T. Kudo, H. Zhou, I. Honma, *The Journal of Physical Chemistry C* 113 (2009) 15337.

[22]Z. Quan, T. Osokoshi, N. Sonoyama, *J. Alloys Compd.* 541 (2012) 137.

[23]K. Dokko, N. Nakata, K. Kanamura, *J. Power Sources* 189 (2009) 783.

[24]M.R. Palacin, D. Larcher, A. Audemer, N. Sac-Epee, G.G. Amatucci, J.M. Tarascon, *J. Electrochem. Soc.* 144 (1997) 4226.

[25]R. Kanno, H. Kubo, Y. Kawamoto, T. Kamiyama, F. Izumi, Y. Takeda, M. Takano, *J. Solid State Chem.* 110 (1994) 216.

[26]T. Ohzuku, A. Ueda, M. Nagayama, *J. Electrochem. Soc.* 140 (1993) 1862.

[27]M.G.S.R. Thomas, W.I.F. David, J.B. Goodenough, P. Groves, *Mater. Res. Bull.* 20 (1985) 1137.

[28]A. Hirano, K. Kanie, T. Ichikawa, N. Imanishi, Y. Takeda, R. Kanno, T. Kamiyama, F. Izumi, *Solid State Ionics* 152–153 (2002) 207.

[29]W. Li, J.N. Reimers, J.R. Dahn, *Physical Review B* 46 (1992) 3236.

[30]H. Arai, S. Okada, Y. Sakurai, J.-i. Yamaki, *Solid State Ionics* 109 (1998) 295.

[31]T. Ohzuku, A. Ueda, M. Nagayama, Y. Iwakoshi, H. Komori, *Electrochim. Acta* 38 (1993) 1159.

[32]C. Delmas, I. Saadoune, A. Rougier, *J. Power Sources* 44 (1993) 595.

[33]I. Saadoune, C. Delmas, *J. Solid State Chem.* 136 (1998) 8.

[34]M.D. Levi, K. Gamolsky, D. Aurbach, U. Heider, R. Oesten, *Electrochim. Acta* 45 (2000) 1781.

[35]N. Yabuuchi, T. Ohzuku, *J. Power Sources* 119–121 (2003) 171.

[36]Y. Koyama, N. Yabuuchi, I. Tanaka, H. Adachi, T. Ohzuku, *J. Electrochem. Soc.* 151 (2004) A1545.

[37]N. Yabuuchi, Y. Koyama, N. Nakayama, T. Ohzuku, *J. Electrochem.*

Soc. 152 (2005) A1434.

[38]F. Zhou, X. Zhao, J.R. Dahn, J. Electrochem. Soc. 156 (2009) A343.

[39]F. Zhou, X. Zhao, C. Goodbrake, J. Jiang, J.R. Dahn, J. Electrochem. Soc. 156 (2009) A796.

[40]J.B. Goodenough, Y. Kim, J. Power Sources 196 (2011) 6688.

[41]M.H. Rossouw, M.M. Thackeray, Mater. Res. Bull. 26 (1991) 463.

[42]A.D. Robertson, P.G. Bruce, Chem. Commun. 0 (2002) 2790.

[43]P. Kalyani, S. Chitra, T. Mohan, S. Gopukumar, J. Power Sources 80 (1999) 103.

[44]M.M. Thackeray, S.-H. Kang, C.S. Johnson, J.T. Vaughey, R. Benedek, S.A. Hackney, J. Mater. Chem. 17 (2007) 3112.

[45]C.S. Johnson, J.S. Kim, C. Lefief, N. Li, J.T. Vaughey, M.M. Thackeray, Electrochem. Commun. 6 (2004) 1085.

[46]A. van Bommel, L.J. Krause, J.R. Dahn, J. Electrochem. Soc. 158 (2011) A731.

[47]T. Ohzuku, M. Nagayama, K. Tsuji, K. Ariyoshi, J. Mater. Chem. 21 (2011) 10179.

[48]S.-H. Kang, V.G. Pol, I. Belharouak, M.M. Thackeray, J. Electrochem. Soc. 157 (2010) A267.

[49]J.M. Zheng, Z.R. Zhang, X.B. Wu, Z.X. Dong, Z. Zhu, Y. Yang, J. Electrochem. Soc. 155 (2008) A775.

[50]J. Liu, A. Manthiram, J. Mater. Chem. 20 (2010) 3961.

[51]S.-H. Kang, M.M. Thackeray, Electrochem. Commun. 11 (2009) 748.

[52]C. Julien, E. Haro-Poniatowski, M.A. Camacho-Lopez, L. Escobar-Alarcon, J. Jimenez-Jarquín, Materials Science and Engineering: B 72 (2000) 36.

[53]C.M. Julien, M. Massot, Mater. Sci. Eng., B 97 (2003) 217.

[54]C.M. Julien, M. Massot, Materials Science and Engineering: B 100 (2003) 69.

[55]Y.J. Park, J.G. Kim, M.K. Kim, H.T. Chung, H.G. Kim, Solid State

Ionics 130 (2000) 203.

[56]S. Bach, J. Farcy, J.P. Pereira-Ramos, Solid State Ionics 110 (1998) 193.

[57]R.J. Gummow, A. de Kock, M.M. Thackeray, Solid State Ionics 69 (1994) 59.

[58]A. Rougier, K.A. Striebel, S.J. Wen, E.J. Cairns, J. Electrochem. Soc. 145 (1998) 2975.

[59]Y. Xia, Y. Zhou, M. Yoshio, J. Electrochem. Soc. 144 (1997) 2593.

[60]Y. Xia, M. Yoshio, J. Electrochem. Soc. 144 (1997) 4186.

[61]Y. Xia, T. Sakai, T. Fujieda, X.Q. Yang, X. Sun, Z.F. Ma, J. McBreen, M. Yoshio, J. Electrochem. Soc. 148 (2001) A723.

[62]G.G. Amatucci, C.N. Schmutz, A. Blyr, C. Sigala, A.S. Gozdz, D. Larcher, J.M. Tarascon, J. Power Sources 69 (1997) 11.

[63]Y. Xia, M. Yoshio, J. Power Sources 57 (1995) 125.

[64]H. Shigemura, H. Sakaebe, H. Kageyama, H. Kobayashi, A.R. West, R. Kanno, S. Morimoto, S. Nasu, M. Tabuchi, J. Electrochem. Soc. 148 (2001) A730.

[65]J. Hassoun, K.-S. Lee, Y.-K. Sun, B. Scrosati, J. Am. Chem. Soc. (2011) null.

[66]J. Hassoun, S. Panero, P. Reale, B. Scrosati, Adv. Mater. 21 (2009) 4807.

[67]Y.-H. Huang, J.B. Goodenough, Chem. Mater. 20 (2008) 7237.

[68]C. Sun, S. Rajasekhara, J.B. Goodenough, F. Zhou, J. Am. Chem. Soc. (2011) null.

[69]P. Gibot, M. Casas-Cabanas, L. Laffont, S. Levasseur, P. Carlach, S. Hamelet, J.-M. Tarascon, C. Masquelier, Nat Mater 7 (2008) 741.

[70]H. Huang, S.-C. Yin, L.F. Nazar, Electrochem. Solid-State Lett. 4 (2001) A170.

[71]Z. Chen, J.R. Dahn, J. Electrochem. Soc. 149 (2002) A1184.

[72]C. Delmas, M. Maccario, L. Croguennec, F. Le Cras, F. Weill, Nat

Mater 7 (2008) 665.

[73]A. Yamada, M. Yonemura, Y. Takei, N. Sonoyama, R. Kanno, Electrochem. Solid-State Lett. 8 (2005) A55.

[74]A. Yamada, S.C. Chung, K. Hinokuma, J. Electrochem. Soc. 148 (2001) A224.

[75]M.S. Islam, D.J. Driscoll, C.A.J. Fisher, P.R. Slater, Chem. Mater. 17 (2005) 5085.

[76]S.-i. Nishimura, G. Kobayashi, K. Ohoyama, R. Kanno, M. Yashima, A. Yamada, Nat Mater 7 (2008) 707.

[77]V. Srinivasan, J. Newman, J. Electrochem. Soc. 151 (2004) A1517.

[78]A. Yamada, H. Koizumi, N. Sonoyama, R. Kanno, Electrochem. Solid-State Lett. 8 (2005) A409.

[79] <http://www.undp.org.cn>

[80]J.B. Goodenough, Y. Kim, Chem. Mater. 22 (2009) 587.

[81]H.-K. Song, K.T. Lee, M.G. Kim, L.F. Nazar, J. Cho, Adv. Funct. Mater. 20 (2010) 3818.

[82]A.S. Arico, P. Bruce, B. Scrosati, J.-M. Tarascon, W. van Schalkwijk, Nat Mater 4 (2005) 366.

[83]M. Okubo, E. Hosono, J. Kim, M. Enomoto, N. Kojima, T. Kudo, H. Zhou, I. Honma, J. Am. Chem. Soc. 129 (2007) 7444.

[84]M. Okubo, E. Hosono, T. Kudo, H.S. Zhou, I. Honma, Solid State Ionics 180 (2009) 612.

[85]P. Poizot, S. Laruelle, S. Grugeon, L. Dupont, J.-M. Tarascon, Nature 407 (2000/09/28/) 496.

[86]P. Poizot, S. Laruelle, S. Grugeon, L. Dupont, J. Tarascon, Ionics 6 (2000) 321.

[87]H. Li, G. Richter, J. Maier, Adv. Mater. 15 (2003) 736.

[88]N. Yamakawa, M. Jiang, B. Key, C.P. Grey, J. Am. Chem. Soc. 131 (2009) 10525.

[89]C.-H. Lai, K.-W. Huang, J.-H. Cheng, C.-Y. Lee, B.-J. Hwang, L.-J.

Chen, J. *Mater. Chem.* 20 (2010) 6638.

[90]A. Débart, L. Dupont, R. Patrice, J.M. Tarascon, *Solid State Sciences* 8 (2006) 640.

[91]N. Pereira, L.C. Klein, G.G. Amatucci, *J. Electrochem. Soc.* 149 (2002) A262.

[92]D. Larcher, C. Masquelier, D. Bonnin, Y. Chabre, V. Masson, J.-B. Leriche, J.-M. Tarascon, *J. Electrochem. Soc.* 150 (2003) A133.

[93]S. Ito, K. Nakaoka, M. Kawamura, K. Ui, K. Fujimoto, N. Koura, *J. Power Sources* 146 (2005) 319.

[94]M. Hibino, J. Terashima, T. Yao, *J. Electrochem. Soc.* 154 (2007) A1107.

[95]S. Kanzaki, T. Inada, T. Matsumura, N. Sonoyama, A. Yamada, M. Takano, R. Kanno, *J. Power Sources* 146 (2005) 323.

[96]S. Kanzaki, A. Yamada, R. Kanno, *J. Power Sources* 165 (2007) 403.

[97]S. Koike, K. Tatsumi, *J. Power Sources* 146 (2005) 241.

[98]Y. Uchimoto, K. Amezawa, T. Furushita, M. Wakihara, I. Taniguchi, *Solid State Ionics* 176 (2005) 2377.

[99]T. Lee, K. Cho, J. Oh, D. Shin, *J. Power Sources* 174 (2007) 394.

[100]T. Matsumura, N. Imanishi, A. Hirano, N. Sonoyama, Y. Takeda, *Solid State Ionics* 179 (2008) 2011.

[101]M. Hirayama, K. Sakamoto, T. Hiraide, D. Mori, A. Yamada, R. Kanno, N. Sonoyama, K. Tamura, J.i. Mizuki, *Electrochim. Acta* 53 (2007) 871.

[102]M. Hirayama, N. Sonoyama, T. Abe, M. Minoura, M. Ito, D. Mori, A. Yamada, R. Kanno, T. Terashima, M. Takano, K. Tamura, J.i. Mizuki, *J. Power Sources* 168 (2007) 493.

[103]M. Hirayama, N. Sonoyama, M. Ito, M. Minoura, D. Mori, A. Yamada, K. Tamura, J.i. Mizuki, R. Kanno, *J. Electrochem. Soc.* 154 (2007) A1065.

[104]Q. Wang, D. O'Hare, *Chem. Rev.* 112 (2012) 4124.

[105]X. Guo, F. Zhang, D.G. Evans, X. Duan, *Chem. Commun.* 46 (2010) 5197.

- [106]A.I. Khan, D. O'Hare, *J. Mater. Chem.* 12 (2002) 3191.
- [107]B. Sels, D.D. Vos, M. Buntinx, F. Pierard, A. Kirsch-De Mesmaeker, P. Jacobs, *Nature* 400 (1999) 855.
- [108]A.C.S. Alcantara, P. Aranda, M. Darder, E. Ruiz-Hitzky, *J. Mater. Chem.* 20 (2010) 9495.
- [109]B. Li, J. He, D. G. Evans, X. Duan, *Applied Clay Science* 27 (2004) 199.
- [110]J.-H. Choy, S.-Y. Kwak, J.-S. Park, Y.-J. Jeong, J. Portier, *J. Am. Chem. Soc.* 121 (1999) 1399.
- [111]J.X. He, K. Kobayashi, M. Takahashi, G. Villemure, A. Yamagishi, *Thin Solid Films* 397 (2001) 255.
- [112]J. Han, D. Yan, W. Shi, J. Ma, H. Yan, M. Wei, D.G. Evans, X. Duan, *The Journal of Physical Chemistry B* 114 (2010) 5678.
- [113]L. Li, R. Ma, Y. Ebina, K. Fukuda, K. Takada, T. Sasaki, *J. Am. Chem. Soc.* 129 (2007) 8000.
- [114]T. Kameyama, K.-i. Okazaki, K. Takagi, T. Torimoto, *PCCP* 11 (2009) 5369.
- [115]T. Sato, S. Onai, T. Yoshioka, A. Okuwaki, *Journal of Chemical Technology & Biotechnology* 57 (1993) 137.
- [116]F.M. Labajos, V. Rives, P. Malet, M.A. Centeno, M.A. Ulibarri, *Inorg. Chem.* 35 (1996) 1154.
- [117]D. Tichit, M.N. Bennani, F. Figueras, J.R. Ruiz, *Langmuir* 14 (1998) 2086.
- [118]M. Osada, Y. Ebina, K. Takada, T. Sasaki, *Adv. Mater.* 18 (2006) 295.
- [119]T. Sasaki, M. Watanabe, H. Hashizume, H. Yamada, H. Nakazawa, *J. Am. Chem. Soc.* 118 (1996) 8329.
- [120]A.K. Geim, K.S. Novoselov, *Nat Mater* 6 (2007) 183.
- [121]Y. Omomo, T. Sasaki, Wang, M. Watanabe, *J. Am. Chem. Soc.* 125 (2003) 3568.
- [122]T. Sasaki, M. Watanabe, *J. Am. Chem. Soc.* 120 (1998) 4682.

[123]L. Li, R. Ma, Y. Ebina, N. Iyi, T. Sasaki, Chem. Mater. 17 (2005) 4386.

[124]J. Liang, R. Ma, N. Iyi, Y. Ebina, K. Takada, T. Sasaki, Chem. Mater. 22 (2009) 371.

[125]T. Shibata, K. Fukuda, Y. Ebina, T. Kogure, T. Sasaki, Adv. Mater. 20 (2008) 231.

[126]T. Shibata, T. Ohnishi, I. Sakaguchi, M. Osada, K. Takada, T. Kogure, T. Sasaki, The Journal of Physical Chemistry C 113 (2009) 19096.

[127]M. Osada, T. Sasaki, Adv. Mater. 24 (2012) 210.

[128]M. Onoda, Z. Liu, Y. Ebina, K. Takada, T. Sasaki, The Journal of Physical Chemistry C 115 (2011) 8555.

[129]M. Hibino, M. Ugaji, A. Kishimoto, T. Kudo, Solid State Ionics 79 (1995) 239.

[130]T. Matsumura, N. Sonoyama, R. Kanno, M. Takano, Solid State Ionics 158 (2003) 253.

Chapter 2

Synthesis and Electrochemical Property of LiCoO₂ Thin Films Composed of Nanosize Compounds Synthesized via Nanosheet Restacking Method

2.1 Introduction

Rechargeable thin film batteries have attracted much attention of many researchers and market as important power source for various small electronic devices such as smart card, micro electromechanical system, and so on. Recently, various kinds of synthesis methods of lithium battery cathode material thin films, such as sol-gel method [1], aerosol flame deposition (AFD) [2], r.f. sputtering [3] and pulsed laser deposition (PLD) [4] have developed. Among these methods, sol-gel and AFD method can produce cathode films with lower cost. However, the performance of the film is not much improved from that of the bulk materials in spite of the comparatively smaller particle size (30 ~ 120 nm). Contrary to these methods, it was reported that high performance cathode films could be obtained by using the vacuum deposition methods [3, 4]. Especially, cathode thin films synthesized by PLD method is composed of extremely small particle (10~30 nm) with high density and high surface flatness. This film shows excellent electrochemical performance: Matsumura et al. reported that LiMn₂O₄ thin film synthesized by PLD method shows charge-discharge ability even at over 500 C-rate [4]. The weak point of this film is synthesis cost for most of vacuum deposition methods require highly vacuum condition. This vacuum process raises the total fabrication cost of thin film cell.

Besides the study of such a thin films, synthesis method of nanosize fine grain of powder cathode material has developed in the last decade [5-7]. In order to obtain higher charge-discharge rate capability, shorter Li-ion diffusion length, d , or higher chemical Li-ion diffusion coefficient, D_{Li} , is necessary. Commercial cathodes with

long d (ca. $1\mu\text{m}$) are not suitable for high power batteries, while particles with nanometer order size d should contribute to achieve the rate capability. As an example, Okubo et al. reported that an excellent high rate capability was observed in nanocrystalline LiCoO_2 with an appropriate particle size of 17 nm, synthesized by hydrothermal method [5].

Lately, a variety of unilamellar two-dimensional crystallites with chemically delaminating a layered compound into molecular single layers have been actively studied [8-10]. The resulting elementary layers so called “nanosheets”, with the thickness of a nano- or sub nanometer, have well-defined composition and highly crystalline nature as a single layer material. Using the nanosheets of metal oxide like TiO_2 [8] and MnO_2 [9], new types of metal oxide layered compounds were synthesized and applied as the electrodes of lithium battery. These nanosheets show charge-discharge feature as cathode materials.

In the present study, LiCoO_2 films composed of nanosize compounds attempted to be synthesized by electrochemical deposition of nanosheet and subsequent hydrothermal treatment, and electrochemical property of obtained films were examined.

Table 2.1 Synthesis methods for cathode of thin-film Lithium battery.

	Sol-gel [1]	Aerosol flame deposition [2]	RF magnetron sputtering [3]	Pulsed laser deposition [4]
Particle size (nm)	50~120	30~70	20~30	10~20
Electrochemical property	Comparatively smaller particle size		High quality dense thin film Show excellent electrochemical performance	
Cost	Low	Low	High	High

2.2 Experimental

2.2.1 Synthesis and characterization of LiCoO₂ thin film on Au substrate

The procedure of the synthesis of LiCoO₂ films was summarized in Figure 2.1. Co(OH)_{1.72}(DBS)_{0.27}·1.06 H₂O was prepared by anion exchange reaction with sodium dodecylbenzenesulfonate (NaDBS) solution at 70 °C, starting from layered compound Co(OH)_{1.62}(CH₃COO)_{0.38}·0.53 H₂O [11]. The precipitate was filtered, dried, and then mixed with 1-butanol (99.5%, Kishida chemical) to give colloidal suspensions of cobalt hydroxide nanosheets. Restacked nanosheets were obtained by electrophoretic deposition (EPD) in the colloidal suspensions with the current density of 20 μA/cm² controlled by galvanostat (Hokuto HABF-501) for 5, 15, 30, 60 and 240 min on Au substrates (10×10 mm). For the observation of the surface morphology of the deposited nano sheet, 10 seconds deposited film on the Au coated mica substrates were used. LiCoO₂ thin films were prepared by hydrothermal reaction of restacked nanosheet films in 1M LiOH solution at 170 °C for 12 h. After the hydrothermal reaction, the as-prepared LiCoO₂ thin films were annealed at 500 °C for 1 min in air to improve crystallinity.

The crystal structure of the thin films was characterized by X-ray diffraction (Rigaku RAD-C) using Cu Kα1 radiation in steps of 0.03° for the range of 10-90°. Raman spectra were recorded on a Laser Raman Spectroscopy (JASCO NR-1100) in the range of 200 to 800 cm⁻¹, using Ar ion laser (λ=514 nm).

The morphology of thin film was observed by scanning electron microscope (JEOL JSM-5610). Elemental analysis for the Co(OH)_x nanosheet is carried out using EDS (JOEL JSM-7001FF) equipped with SEM system. The surface areas of the thin films were measured by laser microscope (KEYENCE VK-9700). AFM measurement was performed by JEOL JSPM-5200 SPM microscope in AC mode, using Si cantilevers tip with the spring constant 42 N/m.

2.2.2 Electrochemical measurements

Electrochemical measurement of the LiCoO_2 thin film was performed using self designed cell for thin film electrode at 25 °C. The main body of the cell with the shape of hollow cuboid is made by DIFLON. A small hole with the area of 0.64 cm^2 is on the main body and opposite side is opened. Anode and cathode are fixed on the two stainless steel plates, and located at two opposite sides of the main body so that electrodes contact with the electrolyte. Lithium metal was used as anode and 1 M solution of LiPF_6 in EC:DEC (1:1, v/v) was used as the electrolyte. Charge-discharge measurement was carried out in the potential range between 3.5 V and 4.3 V by a potentiogalvanostat (Hokuto HA-501) and a function generator (Hokuto HB-105). Electrochemical impedance spectroscopy measurements of the cells were performed using an impedance analyzer (Solatron 1255). The frequency range was from 10^{-2} Hz to 10^6 Hz with the applied voltage of 10 mV. The voltage imposed on the electrode was controlled by potentiostat (Solatron 1280 C).

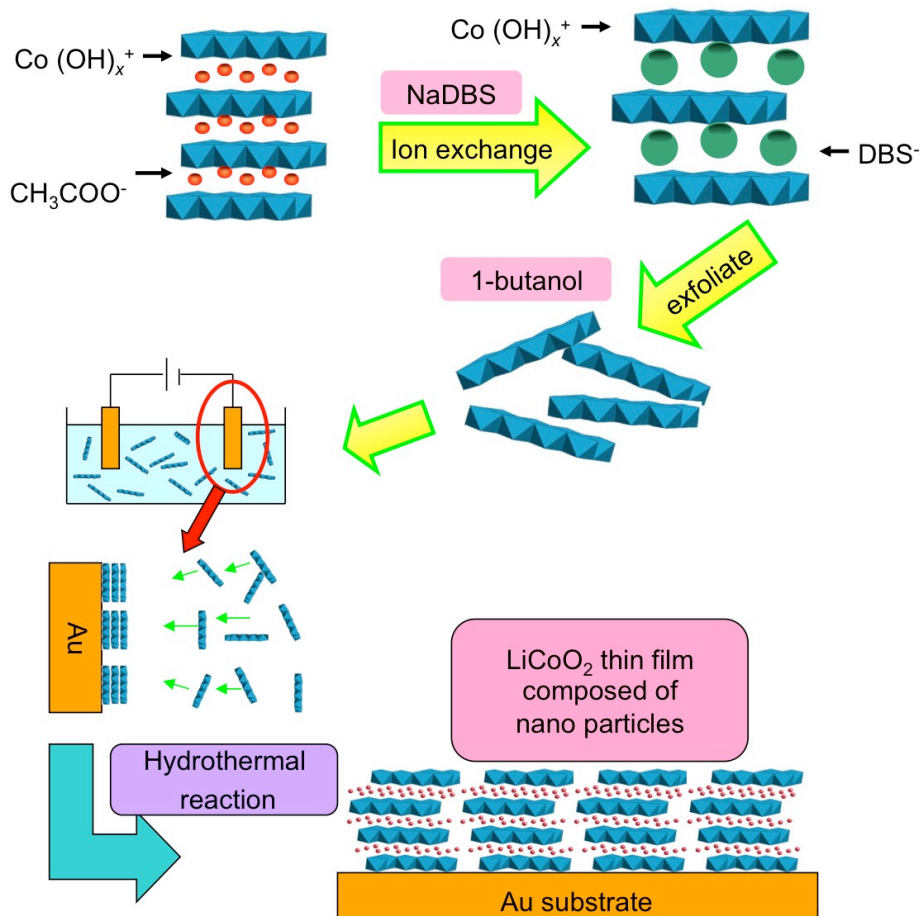


Figure 2.1 Synthesis of nanosize LiCoO_2 by nanosheet restacking and subsequent hydrothermal method.

2.3 Results and discussion

2.3.1 Characterization of the LiCoO_2 thin film

Figure 2.2 shows XRD patterns for the precursor and products in the synthesis process. As were seen in Figure 2.2 (a), the interlayer reflections of $\text{Co(OH)}_{1.72}(\text{DBS})_{0.27} \cdot 1.06 \text{H}_2\text{O}$ shifted to lower angle by exchanging CH_3COO^- ion to DBS^- ion, for the distance between cobalt hydroxide layers increased by exchanging to bulky anion. By dispersing DBS^- exchanged cobalt hydroxide, Co(OH)_x nanosheets emulsion can be obtained. In Figure 2.2 (b), XRD pattern

for hydrothermal treated $\text{Co}(\text{OH})_x$ films after 240 min EPD was shown. 003, 101, 105 and 009 reflections can be observed and agreed with the position of LiCoO_2 (ICSD No. 29225), though the reflections of impurities phase containing Co_3O_4 were also observed. Figure 2.3 is the XRD patterns for LiCoO_2 films electroplated with deposition time of 5, 15, 30 and 60 min. Comparing with pattern in Figure 2.2 (b), for the films with shorter time electroplated, only the 003 reflection of LiCoO_2 can be observed because of the reflection of Au substrate that locates near other reflections of LiCoO_2 . The grain size, estimated from the full width at half maximum of 003 reflection of LiCoO_2 thin films synthesized on Au substrates, are about 14.8, 14.9 16.9 and 15.6 nm, respectively. This indicates the grain size of the thin films is independent of the thickness of precursor cobalt hydroxide films. These crystallite sizes were near the particle size of nanosize LiCoO_2 powder (17 nm) synthesized under the same hydrothermal reaction condition reported by Okubo et al. [5].

In Figure 2.4, Raman scattering spectra for thin film hydrothermal treated after 5 min EPD was shown. Characteristic scatterings those can be assigned to A_{1g} and E_g of LiCoO_2 were observed at around 484 and 594 cm^{-1} , respectively [12, 13]. Scatterings of Co_3O_4 , which exist as impurity in the LiCoO_2 thin films reported at previous work [2, 14], were also observed. However, the amount of the Co_3O_4 in the thin films was considered to be very few because XRD reflection of Co_3O_4 was not found in the thinner films (Figure 2.3). From these data, it was concluded that LiCoO_2 film composed of the nano size grain could be synthesized via a cobalt hydroxide nanosheet electroplating and subsequent hydrothermal treatment.

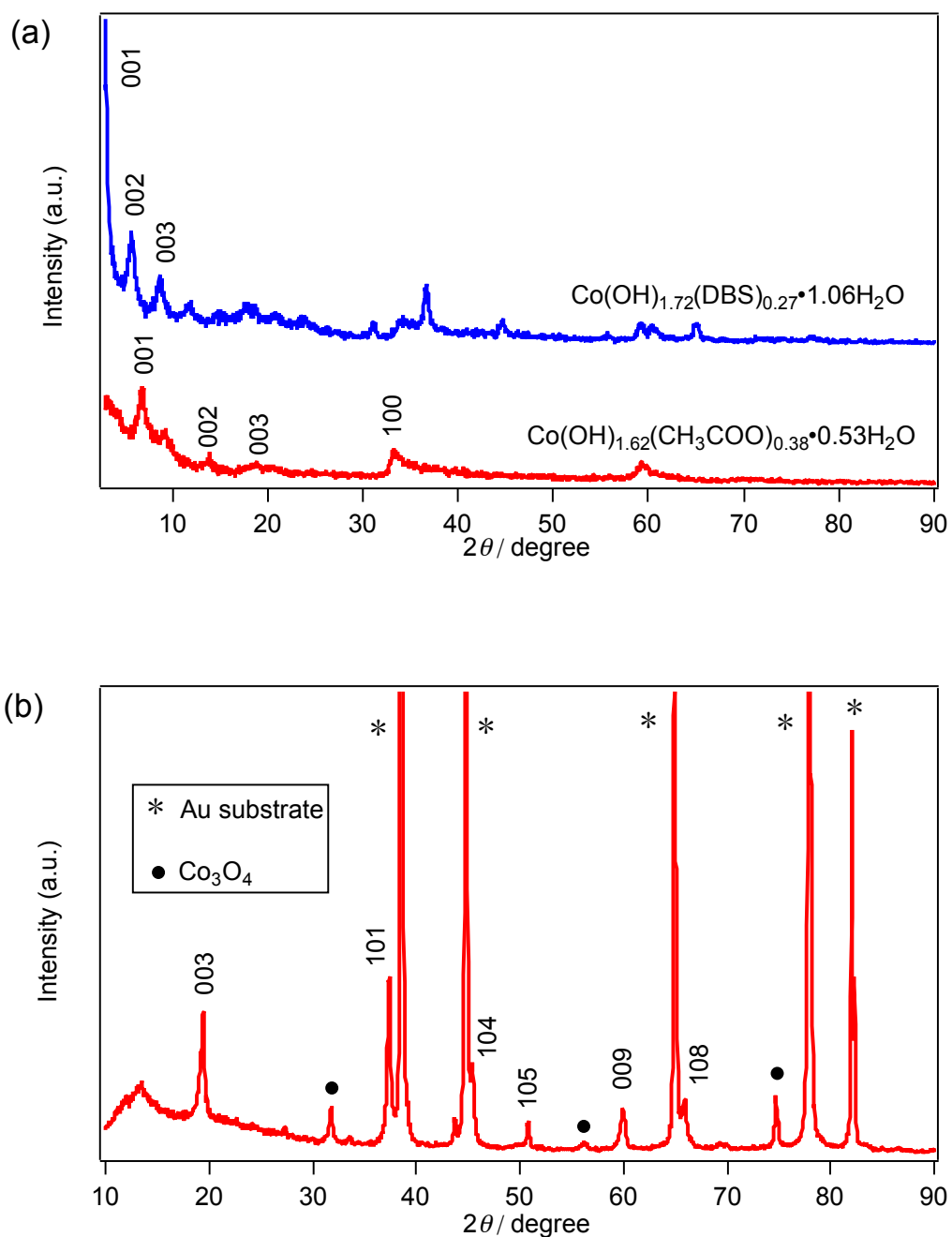


Figure 2.2 (a) XRD pattern for layered compounds before and after ion exchange. (b) XRD pattern of LiCoO_2 thin film synthesized by hydrothermal reaction after electroplating for 240 min.

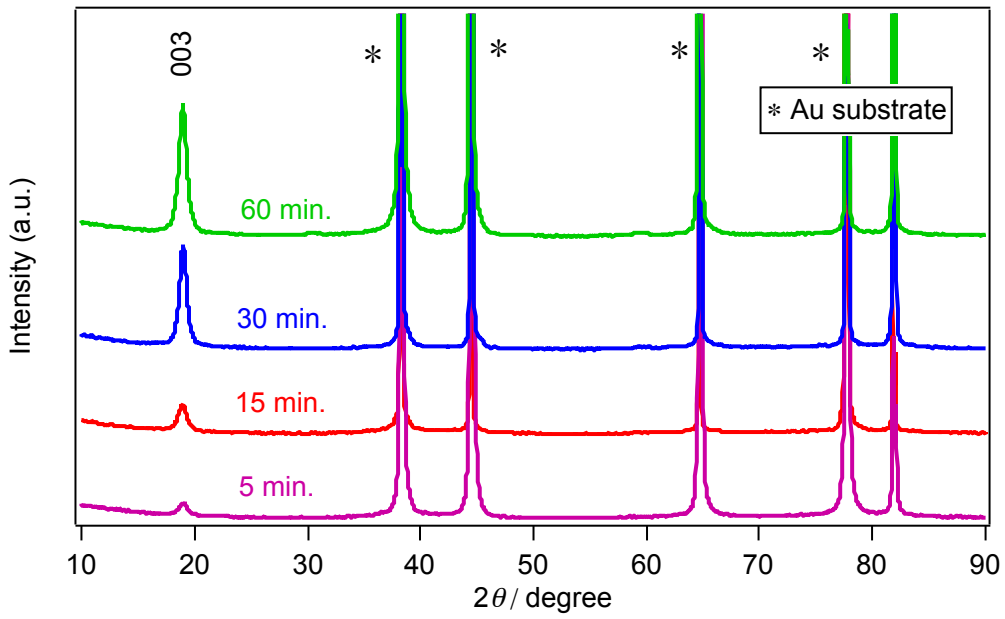


Figure 2.3 XRD patterns of the LiCoO₂ thin film synthesized from precursor cobalt hydroxide films with different cathodic electroplating period.

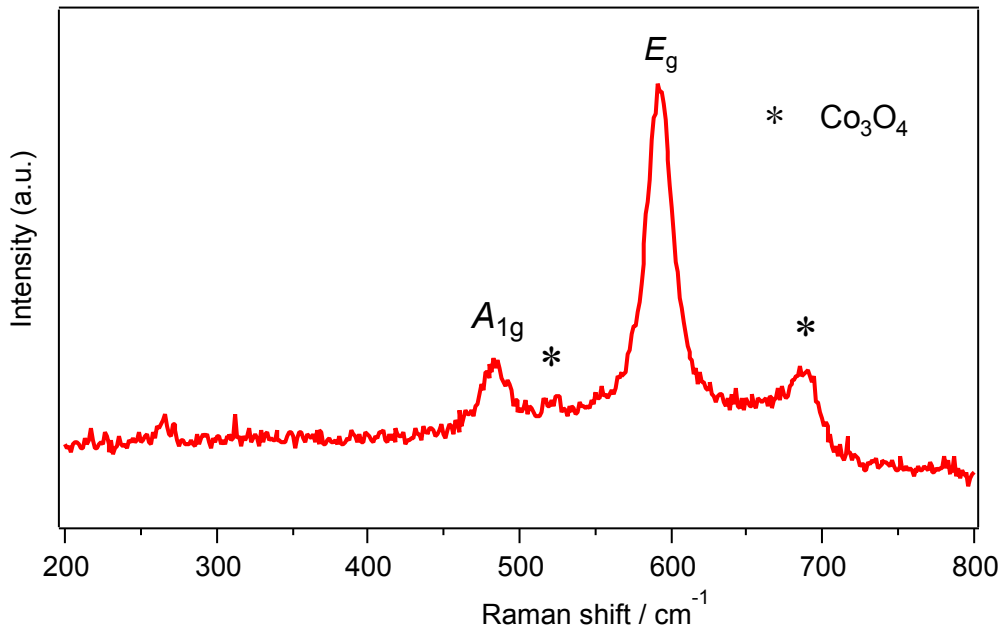


Figure 2.4 Raman spectra for LiCoO₂ thin film electroplated for 5 min on Au substrate.

Figure 2.5 (a) shows SEM image of deposited compound on the surface of Au coated mica substrate after 10 seconds electro-deposition. A disc like sheet with a diameter of about 100 nm was observed. In Table 2.1, the composition of this sheet analyzed by EDS was listed. The deposited sheet is mainly consisted with cobalt, carbon, sulfur and oxygen. This composition agreed with that of DBS⁻ ion exchanged Co(OH)_x sheet. AFM image of the surface of the film with deposition time of 10 sec was shown in Figure 2.5 (b). Large masses with height of 110 nm and scaly sheets with height of 30 nm were found. Scaly sheets would be the deposited Co(OH)_x nanosheet that were observed by SEM (Figure 2.5 (a)) and larger masses would be the clusters of Co(OH)_x sheets that were not fully dispersed in the solution. Figure 2.5 (c) and (d) show the SEM images of the surface of the films with 5 min electro-deposition before and after the hydrothermal treatment. Before hydrothermal treatment, the configuration of the stacked nanosheet can be confirmed. After the treatment, aggregates of spherical particles were found whereas the secondary particles can be seen that consist of grain with the size of about 10-20 nm. The size of the primary particles is almost consistent with the estimated grain size from the half bandwidth of X-ray reflection (Figure 2.3). Figure 2.6 (a)-(d) show the surface morphologies of LiCoO₂ films with different deposition time. Evident surface morphology change was perceived with the deposition time. For the films with shorter deposition time (5-15 min), the surface of film is much rugged with three-dimensional surface structure, whereas the denser and smoother surface was observed for the films with longer deposition time (30-60 min).

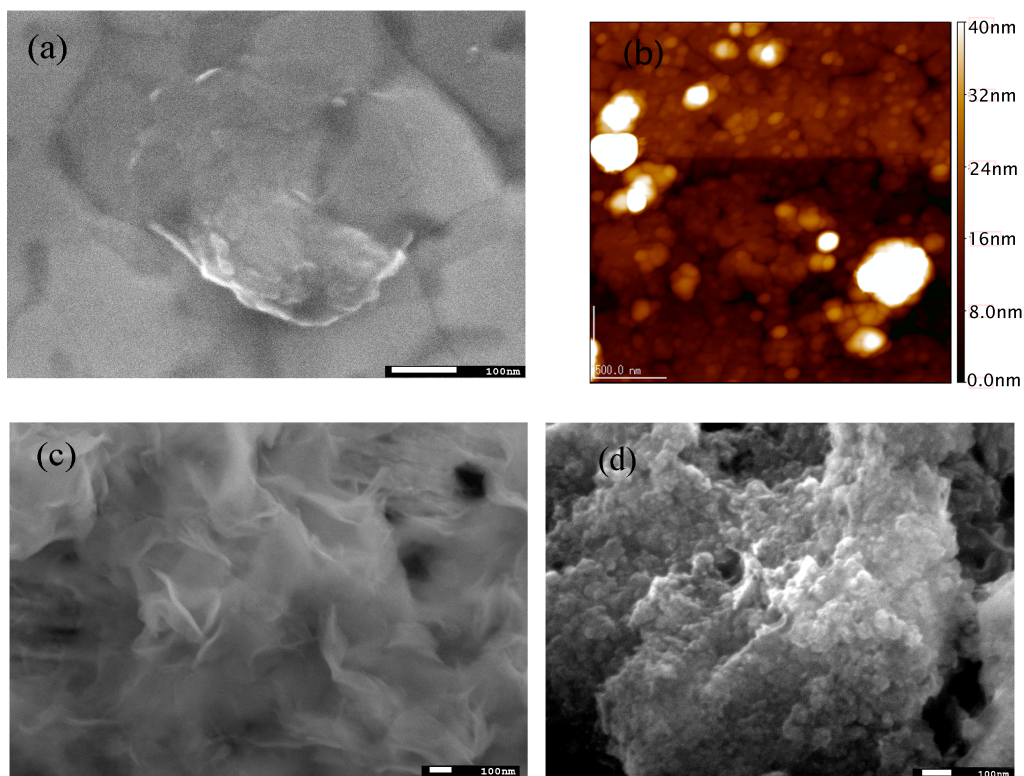


Figure 2.5 (a) SEM image of deposited compounds on the surface of Au coated mica substrate after 10 sec electro-deposition. (b) AFM image of cobalt nanosheets deposited on Au substrate with 10 sec deposition time.

SEM images of the thin film surface with 5 min electro-deposition (c) before and (d) after the hydrothermal treatment.

Table 2.2 Composition of Co(OH)_x nanosheet analyzed by EDS.

Element	Wt (%)	At (%)
Co	48.75	20.94
C	14.07	29.65
O	28.77	45.51
S	4.26	3.37
Au	4.15	0.53

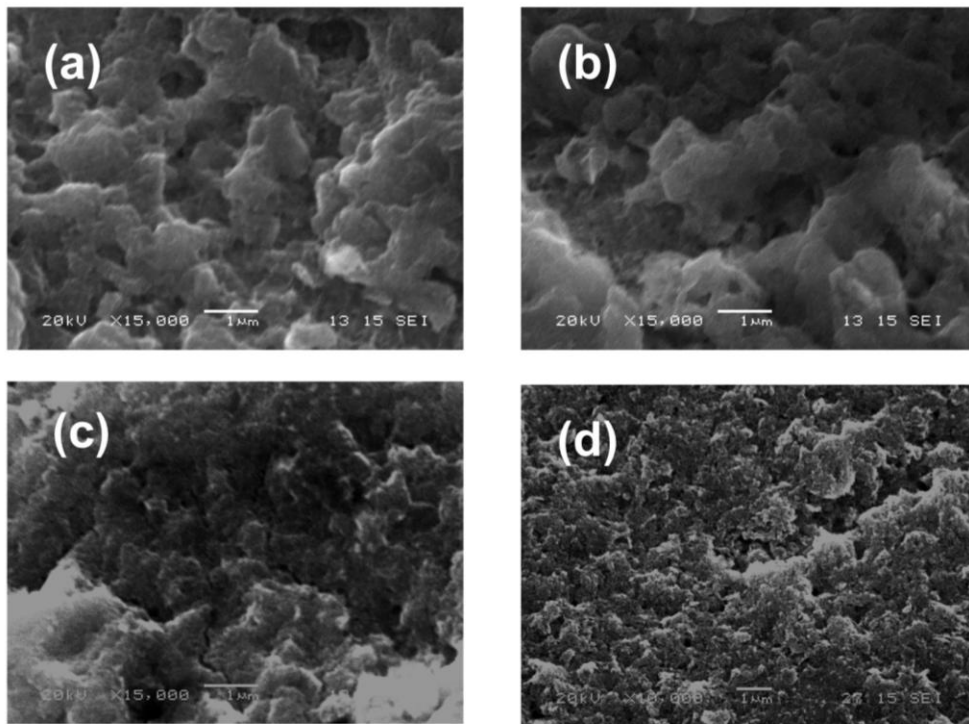


Figure 2.6 The surface morphologies of LiCoO_2 films with different deposition time. (a) 5 min (b) 15 min (c) 30 min (d) 60 min.

2.3.2 Electrochemical measurements

The charge-discharge curves for the LiCoO_2 film with the deposition time of 5 min were shown in Figure 2.7 (a). Evident plateaus were observed both in the charging and discharging processes. Okubo et al. reported that with decreasing the particle size of LiCoO_2 , the plateaus became indistinct in the region of the size below 10 nm. They explained this reason that the impurity phase $\text{Co}(\text{II})$ compounds, that are contained at the surface of LiCoO_2 increases with the increasing the surface area by the size reduction of LiCoO_2 . In the present study, the particle size estimated from XRD is 14~17 nm. This size is almost consistent with the most appropriate size of LiCoO_2 nano particle Okubo et al. reported: around 17 nm [5]. In the discharging process, ohmic potential drop was observed with raising discharge rate. As shown in Table 2.3, increasing C-rate from 20 C to

to 200 C for the LiCoO₂ thin film with the deposition time of 5 min, the discharge potential drop was 0.12V, whereas the same ohmic potential drop occurred by raising the C-rate from 3 C to 21 C for the films with the deposition time of 60 min. This result suggests that electric conductivity decreases with the increasing deposition time.

In Figure 2.7 (b), relationship between the discharge rate and the utilization efficiency of discharge capacity for LiCoO₂ thin films with various thickness was plotted, where the capacity with the current 10 μ A is assumed to be obtained with 100% utilization efficiency. For the LiCoO₂ films with lower thickness (5 and 15 min deposition), showed good rate performance. Especially, film with 5min deposition sustained 74% efficiency over 200 C-rate. LiCoO₂ powder with nano particle size was reported to show high rate performance: about 63% with 100 C-rate [5]. Increasing the deposition time, for the LiCoO₂ film in the present study, utilization efficiency steeply decreased with the increase in the C-rate. This steep decrease in utilization efficiency with deposition time is presumed to be caused by the decrease in electric conductivity, because no conducting aid was added in the fabrication process. Despite considering these factors, the difference between the films with deposition time of 15 and 30 min appears to be too large. For the analysis of this electrode reaction, AC impedance spectroscopy measurements were carried out.

Table 2.3 The relationship between increased discharge C-rate and ohmic potential drop.

Electroplating time	The change of the C-rate	Ohmic drop (V)
5 min	20 C to 200 C	0.12
15 min	36 C to 108 C	0.12
30 min	7 C to 50 C	0.11
60 min	3 C to 21 C	0.13

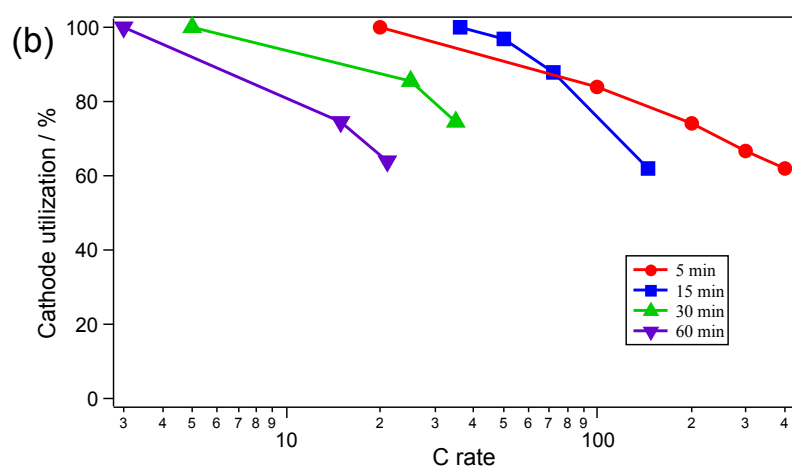
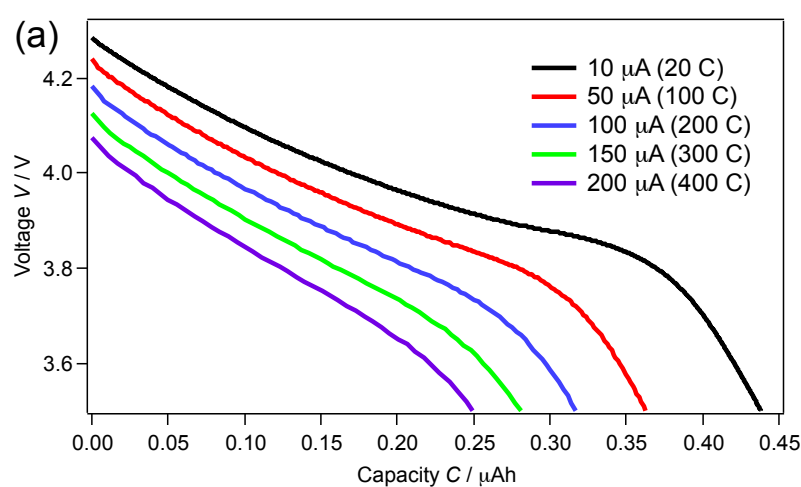


Figure 2.7 (a) Charge-discharge curve of 5 min deposited sample at various current and (b) the relationship between the utilization efficiency of the discharge capacity and discharging rate for LiCoO_2 film with various thickness.

In Figure 2.8, Nyquist plots of LiCoO₂ film on Au substrate with the 5 min deposition time in the frequency range 10⁻² to 10⁶ Hz at various potentials in the discharge process are shown. At the potential of 3.6 V, only blocking electrode behavior was observed. Above 3.9 V, two depressed semi-circles appeared in the high frequency region and a straight line with 45° slope was obtained in the lower frequency region. The semi-circles at high frequency could be due to the solid electrolyte interface and charge-transfer resistance, respectively. The straight line of 45° slope is related to Warburg region where the transition process shifts from charge transfer control to diffusion control. The obtained impedance spectra were analyzed using the equivalent circuit shown in the inset of Figure 2.8. The relationship between the charge-transfer resistance R_{ct} estimated from the Nyquist plots and the imposed voltage on the LiCoO₂ films was shown in Figure 2.9. For all films, R_{ct} increased with decreasing the potential. The extent of R_{ct} increase was largely dependent on the film thickness: thinner film trends to show higher R_{ct} at the lower voltage region. In Table 2.4, the diffusion constants of lithium ion estimated from the AC impedance spectra at 4.2V were listed. As previous work [15-17] reported that D_{Li} values measured by EIS were in the range of 10⁻⁹ to 10⁻¹³ cm²s⁻¹, it is difficult to determine the accurate value of the diffusion constants of thin film. Because of EIS method contains some error for calculating the diffusion constants, it is not reliable and can only be considered as the apparent value. In the present work, although the thin film with electroplating 30 min deposition shows highest value, these estimated values seems can not be used for discussion of diffusion constant dependence on the film thickness for the error they contain. In the present stage, D_{Li} seems to be independent on the film thickness, because the size of particle that consists the film is almost the same in any films synthesized in this study. This estimated diffusion constant agreed with that of LiCoO₂ nanoparticle reported by Okubo et al. (9×10⁻¹³ cm²s⁻¹) [6]. This result seems reasonable, considering particle size of these LiCoO₂ is almost the same. The higher R_{ct} for thinner films seems ascribable to the surface area of the films that can be confirmed by the

(d)). This larger surface area for thinner LiCoO₂ nanoparticle film is consistent with the rate dependence of the utilization efficiency of discharge capacity (Figure 2.5 (d)). The surface area ratios of the LiCoO₂ films with deposition time of 15 min, 30 min and 60 min, which measured by laser microscope, were 2.1814, 1.1658 and 1.3882 $\mu\text{m}^2/\mu\text{m}^2$, respectively. The sample of 15min shows the largest surface area, as estimated in Figure 2.6 (b)-(d). The surface area of the thin film with the deposition time of 5 min can't be measured because much Au substrate exposed among the thin film, but as shown in the SEM image, the surface area of the thinnest film would larger than the thicker ones. For thinner films, larger surface area of LiCoO₂ film with three-dimensional construction would make the fast charge-discharge possible. Increasing the film thickness, surface morphology changed smoother and flatter. This morphology change would make the surface area smaller and fast charge-discharge disable.

Table 2.4 The Li-ion chemical diffusion coefficient of LiCoO₂ thin film with various thickness.

Cathodic electroplating time	D_{Li} by EIS (cm^2s^{-1})
5 min	1.66×10^{-12}
15 min	4.80×10^{-12}
30 min	1.16×10^{-11}
60 min	8.01×10^{-12}

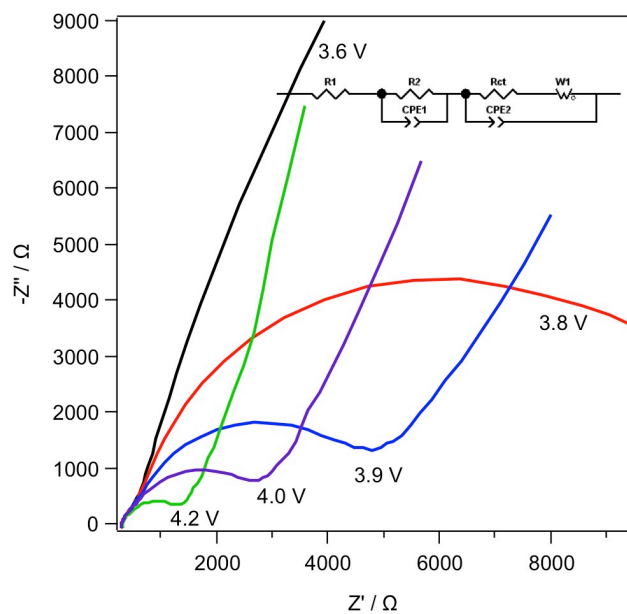


Figure 2.8 Nyquist plots for LiCoO_2 film on Au substrate with 5 min deposition time at various voltages.

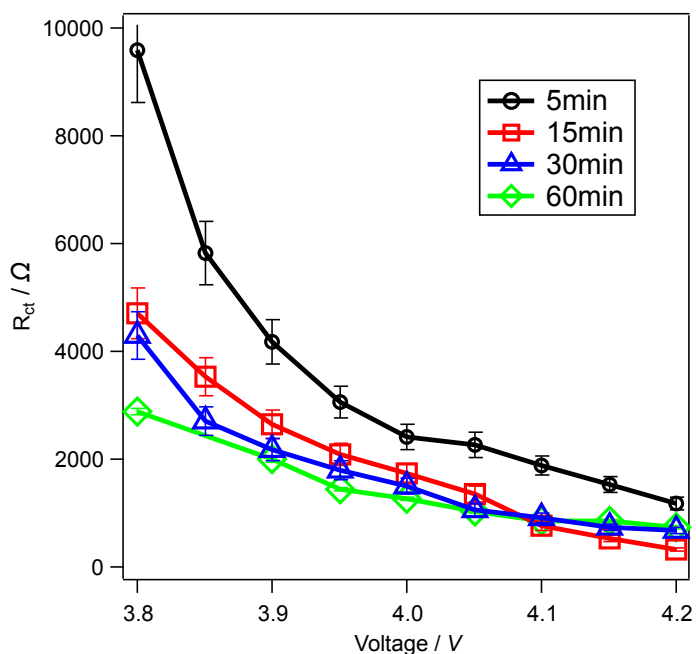


Figure 2.9 Charge-transfer resistance R_{ct} of LiCoO_2 thin films at various voltages.

2.4 Conclusion

LiCoO₂ thin films composed of nano particles can be prepared by nanosheet restacking and subsequent hydrothermal reaction on the Au substrate. We compared the structures and electrochemical behaviors among the thin film with various thicknesses. Surface morphology of these films observed by SEM for thinner film has three-dimensional surface structure, whereas surface of thicker films become flatter. Optimum high rate performance was obtained by the thinnest film with deposition time of 5 min with large surface area. By optimizing of this method, cathode material films with high performance would be obtained with low cost.

Reference

- [1]Q. Wu, W. Li, Y. Cheng, Z. Jiang, Mater. Chem. Phys. 91 (2005) 463.
- [2]T. Lee, K. Cho, J. Oh, D. Shin, J. Power Sources 174 (2007) 394.
- [3]J.K. Lee, S.J. Lee, H.K. Baik, H.Y. Lee, S.W. Jang, S.M. Lee, Electrochem. Solid-State Lett. 2 (1999) 512.
- [4]T. Matsumura, N. Imanishi, A. Hirano, N. Sonoyama, Y. Takeda, Solid State Ionics 179 (2008) 2011.
- [5]M. Okubo, E. Hosono, J. Kim, M. Enomoto, N. Kojima, T. Kudo, H. Zhou, I. Honma, J. Am. Chem. Soc. 129 (2007) 7444.
- [6]M. Okubo, E. Hosono, T. Kudo, H.S. Zhou, I. Honma, Solid State Ionics 180 (2009) 612.
- [7]M. Okubo, Y. Mizuno, H. Yamada, J. Kim, E. Hosono, H. Zhou, T. Kudo, I. Honma, ACS Nano 4 (2010) 741.
- [8]S. Suzuki, N. Sakai, M. Miyayama, Key Eng. Mater. 388 (2009) 37.
- [9]Wang, K. Takada, A. Kajiyama, M. Onoda, Y. Michiue, Zhang, M. Watanabe, T. Sasaki, Chem. Mater. 15 (2003) 4508.
- [10]Y. Omomo, T. Sasaki, Wang, M. Watanabe, J. Am. Chem. Soc. 125 (2003) 3568.
- [11]L. Poul, N. Jouini, F. Fievet, Chem. Mater. 12 (2000) 3123.
- [12]S.W. Song, K.S. Han, I. Sasagawa, T. Watanabe, M. Yoshimura, Solid State Ionics 135 (2000) 277.
- [13]E.I. Santiago, A.V.C. Andrade, C.O. Paiva-Santos, L.O.S. Bulhões, Solid State Ionics 158 (2003) 91.
- [14]K.-S. Han, S.-W. Song, T. Watanabe, M. Yoshimura, Electrochem. Solid-State Lett. 2 (1999) 63.
- [15]H. Xia, L. Lu, G. Ceder, J. Power Sources 159 (2006) 1422.
- [16]J. Xie, N. Imanishi, A. Hirano, M. Matsumura, Y. Takeda, O.

Yamamoto, *Solid State Ionics* 178 (2007) 1218.

[17]J. Xie, N. Imanishi, T. Matsumura, A. Hirano, Y. Takeda, O. Yamamoto, *Solid State Ionics* 179 (2008) 362.

Chapter 3

Synthesis and Electrochemical Property of LiCoO₂ Thin Film Coated on the Surface of Carbon and Anatase TiO₂ Powders

3.1 Introduction

LiCoO₂ is the most reliable cathode material for the lithium ion battery due to the excellent stability and longevity. Accompanied with the development of high power applications such as the electric vehicle, a high rate capability for the cathode materials of Li rechargeable batteries comes to be required. Recently, some conventional approaches were taken to achieve a high rate charge-discharge capability. One is making active materials composed of a highly dispersed cathode materials and the conductive additives by sol-gel [1], electrostatic spray deposition [2] methods. The other approach is adding highly conductive carbon nanotube as a conductive additive [3]. In spite of these approaches, the high rate performance was still insufficient. In order to achieve a fast discharge performance, shortening the diffusion length of lithium ion in the materials by nano-sizing of cathode material is the most efficient way, because the slow lithium diffusion limits the rate of the whole battery reaction. For example, the thin film cathode composed of nanoparticles synthesized by the sputtering [4], the pulsed laser deposition [5] can deliver excellent electrochemical properties. But highly vacuum condition, which is necessary for the synthesis of the excellent thin films, raises the total fabrication cost of thin film battery.

Lately, electrochemical properties of lithium metal oxide powders synthesized by the hydrothermal reaction with low cost and less energy

consuming have been actively studied [6]. Okubo et al. reported that nanocrystalline LiCoO_2 can be controlled by adjusting the hydrothermal reaction condition, concentration of LiOH solution, temperature and reaction time, and they also reported that an excellent high rate capability was obtained by using hydrothermally synthesized LiCoO_2 with particle size of 17 nm. In spite of such a merit of nanoparticles, it is very easy to aggregate and difficult to mix with the conducting additives homogeneously.

Besides, synthesis methods of various kinds of nano-size materials using nanosheet, such as the flocculation restack method [7], the layer-by-layer self assemble method [8], and the Langmuir-Blodgett deposition method [9], have been developed in the last decade. Nanosheet is a two-dimensional crystal, which is chemically delaminated single layered compound with the thickness of several nanometers and has a well-defined composition with high crystallinity [10]. This nanosheet is known to be restacked and reform a layered material by neutralizing its negative charge. Utilizing the characteristics of the nanosheet, it will be possible to coat the exfoliated nanosheet on the surface of material particles with various shape and size such as carbon, semiconductor and metal particles homogeneously. Furthermore, it would be possible to directly synthesis the well-designed active material nanoparticles on the surface of current collectors by hydrothermal treatment using these deposited nanosheet as a precursor for the Li rechargeable battery with high rate discharging capability and low cost.

In Chapter 2, we investigated the electrochemical property of LiCoO_2 films composed of nanosize compounds on Au substrate synthesized by the nanosheet restacking method and the hydrothermal treatment [11]. A high rate capability (74% of its capacity was maintained at 200 C-rate compared with the capacity at 20 C-rate) was observed in LiCoO_2 film electro-deposited for 5 min. By using this method, it will be possible to coat nanosize LiCoO_2 on the various materials. In the present study, we have attempted at coating LiCoO_2 on the surface of carbon materials that is a cheap material applicable to the commercial battery.

In the first step, we synthesized LiCoO₂ film on the glassy carbon substrate to optimize the synthesis condition of LiCoO₂ layer on the carbon material by examining the electrochemical property of the synthesized LiCoO₂ film. Next, we coated the precursor nanosheet on two kinds of acetylene black (AB) carbon materials, Toka Black (TB) carbon and Denka Black (DB) carbon powder, by the electrostatic self-assembly deposition (ESD) method. LiCoO₂ layer was obtained on the carbon material surface via the hydrothermal treatment. Surface observation and the examination of electrochemical properties for synthesized films were carried out. We also attempted at coating LiCoO₂ on the surface of anatase TiO₂ nanoparticle and for the identification of obtained film and the examination of electrochemical properties.

3.2 Experimental

3.2.1 Synthesis and characterization of LiCoO₂ thin film on glassy carbon substrate and powder materials

The colloidal suspension of the nanosheet precursor was prepared by the procedure reported in the previous paper [11]. The distance between cobalt hydroxide layers of layered Co(OH)_{1.62}(CH₃COO)_{0.38}·0.53 H₂O is extended by stirring with sodium dodecylbenzenesulfonate (NaDBS) (0.05 M, Kishida chemical) at 70°C for 10 h to form Co(OH)_{1.72}(DBS)_{0.27}·1.06 H₂O. The precipitate was collected by filtration, washed by acetone and mixed with 1-butanol (99.5%, Kishida chemical) violently to give colloidal suspensions of cobalt hydroxide nanosheets. The film of the precursor was obtained by the electrophoretic deposition (EPD) method on glassy carbon substrates (10×10×1.0 mm³, BAS Inc) in the colloidal suspension with the current density of 20 μA/cm² controlled by the galvanostat (Hokuto HABF-501) for 5, 15 and 60 min.

For the nanosheets coating on the surface of powder materials, such as Toka

Black carbon #4500 (Tokai Carbon Co, Ltd), Denka Black carbon (Denki Kagaku Kougyou Co, Ltd) and anatase TiO₂ (Ishihara Sangyo, Ltd), the electrostatic self-assembly deposition (ESD) method was used as shown in Figure 3.1. 10 ml of LiOH in 1-butanol solution (1 g/L) was added in the mixture of the target powder (0.1 g) and the nanosheet colloidal suspension (200 ml) to neutralize the charge of the nanosheets to deposit the precursor on the surface of the carbon and TiO₂ by restacking nanosheets. LiCoO₂ films were prepared by the hydrothermal reaction of restacked nanosheet films in the 1 M LiOH solution in autoclave at 170°C for 12 h.

The crystal structure of the films was characterized by the X-ray diffraction measurement (Rigaku Ultima IV) using Cu K α 1 radiation in steps of 0.03° for the range of 10-90°. Raman spectra were recorded with a Laser Raman spectrophotometer (JASCO NRS-3300) in the range of 370 to 800 cm⁻¹, using DPSS laser at the wavelength of 532 nm with a laser power of 100 mW and the integration time of 45 sec. The morphology of film was observed by the scanning electron microscope (JEOL JSM-5610 and Hitach S-4800). Thermal gravimetric analysis (TGA) was carried out on a differential scanning calorimeter (Rigaku DSC 8230) at a 5°C/min rate from room temperature to 700°C under air.

3.2.2 Electrochemical measurements

For the electrochemical measurements, LiCoO₂ film on glassy carbon substrate was set in thin film cell. The main body of the cell with the shape of hollow cuboid is made of Diflon. Anode and cathode are fixed on the two stainless steel plates, and located at two opposite sides of the main body so that electrodes contact with the electrolyte. The actual surface area of cathode film was 0.64 cm². The powder samples were assembled to the CR2032 coin cell for electrochemical measurement. TiO₂ powder coated with LiCoO₂ (80 wt %) was mixed with 15 wt % acetylene black and 5 wt % polytetrafluoroethylene (PTFE) binder to prepare cathode active materials. The powder samples of LiCoO₂ on

carbon materials were mixed with PTFE binder with the weight ratio of 98:2 to prepare active materials without adding a furthermore carbon conducting additive. These cathode active materials were pressed to pellet shape, and no additional current collector was used. For both type of cells, lithium metal and 1 M solution of LiPF_6 in EC:DEC (3:7, v/v) were used as the anode electrode material and the electrolyte, respectively. Charge-discharge measurement was carried out at 25°C by a potentio-galvanostat (Solartron 1280C) for the thin film cell and a battery tester (Interface model 0Z0-A19) controlled by CDS current control program (Sharp Corp.) for the coin cell. The electrochemical impedance spectroscopy measurements of the cells at 25°C were performed at various electrode voltages using an impedance analyzer (Solatron 1255) over the frequency range from 10^{-2} Hz to 10^{-6} Hz with the applied voltage of 10 mV. The voltage imposed on the electrode was controlled by a potentiostat (Solatron 1280 C).

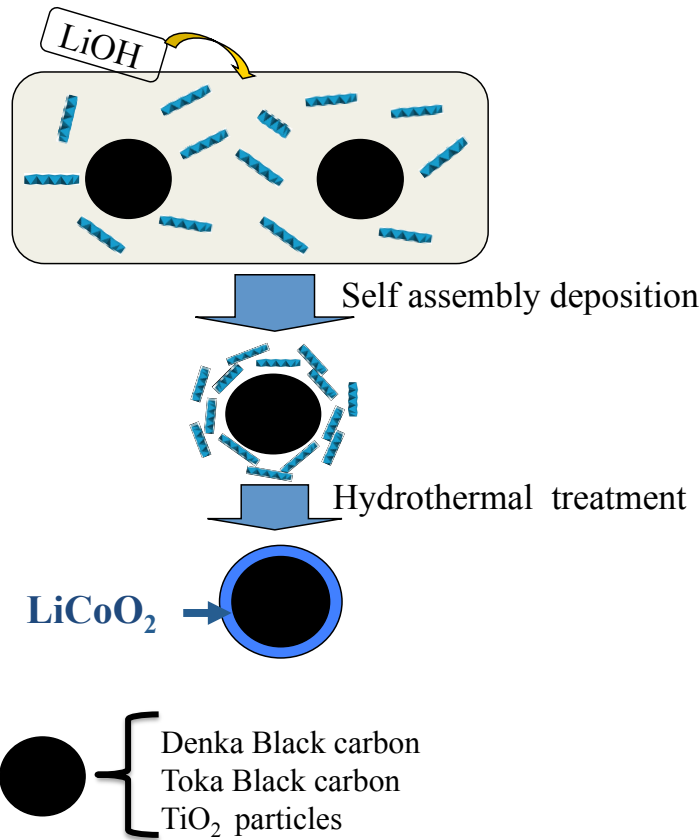


Figure 3.1 Synthesis of LiCoO_2 thin film on the surface of various powder materials by the electrostatic self-assembly deposition and the hydrothermal treatment.

3.3 Results and discussion

3.3.1 LiCoO_2 film on glassy carbon substrate

Figure 3.2 shows X-ray diffraction patterns for the LiCoO_2 film on glassy carbon substrate and LiCoO_2 nanoparticles synthesized by electrostatic self-assembly deposition and hydrothermal treatment. From Figure 3.2 (c), we can confirm the main reflections such as 003, 101,104 and 110 of LiCoO_2 (JCPDS-16-0427). The crystallite size of the LiCoO_2 nanoparticle was estimated from full width at half maximum (FWHM) of 003 and 110 reflections.

The value estimated from 003 reflection, which indicates the thickness of the layer material was 16.3 nm, whereas the width of the particle obtained from 110 reflection was 27.6 nm. This grain size was much smaller than the disc like cobalt hydroxide nanosheet (The thickness measured by AFM and width observed from SEM were about 30 and 200 nm, respectively) that was reported in the previous paper [11]. The decline of the grain size demonstrated that a dissolution-recrystallization reaction occurring during the hydrothermal process that was pointed out by Okubo et al [6]. The unit cell parameters were estimated from reflection positions. The values obtained from the position of 003 and 101 reflections are $a = 2.8283(4) \text{ \AA}$, $c = 14.0584(2) \text{ \AA}$ and $V = 97.3913(3) \text{ \AA}^3$. From the ratio between the two-lattice parameters c/a , a hexagonal layered type structure and a cubic spinel type structure of same stoichiometric LiCoO_2 can be well distinguished. In this sample, the c/a value is 4.97, where the values for a cubic and for a hexagonal are 4.90 and 5.00, respectively [12]. This indicates that the layered LiCoO_2 nanoparticle synthesized by nanosheet restacking method and hydrothermal reaction has a hexagonal structure.

In the XRD pattern for LiCoO_2 film on glassy carbon substrate, shown in Figure 3.2 (a), only weak 003 reflection of the LiCoO_2 can be observed and other main reflections of LiCoO_2 such as 101, 006 and 104 were not obtained because of the strong background of amorphous glassy carbon. The weak reflection would be due to the low thickness of the film and extremely small size of the LiCoO_2 particle. In our previous study [11], the grain size of the LiCoO_2 films synthesized on Au substrates at the same condition was independent from thickness of precursor film with about 15.5 nm.

For the further identification of the film on glassy carbon substrate, Raman scattering spectroscopy measurement was carried out. As shown in Figure 3.3, two strong peaks at 487 and 597 cm^{-1} are assigned to A_{1g} and E_g modes for hexagonal LiCoO_2 phase with the space group $R-3m$ [13]. Other two weak peaks observed around 522 and 671 cm^{-1} are assigned to spinel phase of LiCoO_2

[14]. This result indicates that the samples synthesized in the present study have hexagonal structure but a little amount of spinel phase is also contained as an impurity. This result is consistent with the report by Song et al. that showed that spinel LiCoO_2 phase is tend to be produced in lower LiOH concentration than 4 M in the hydrothermal reaction process [14].

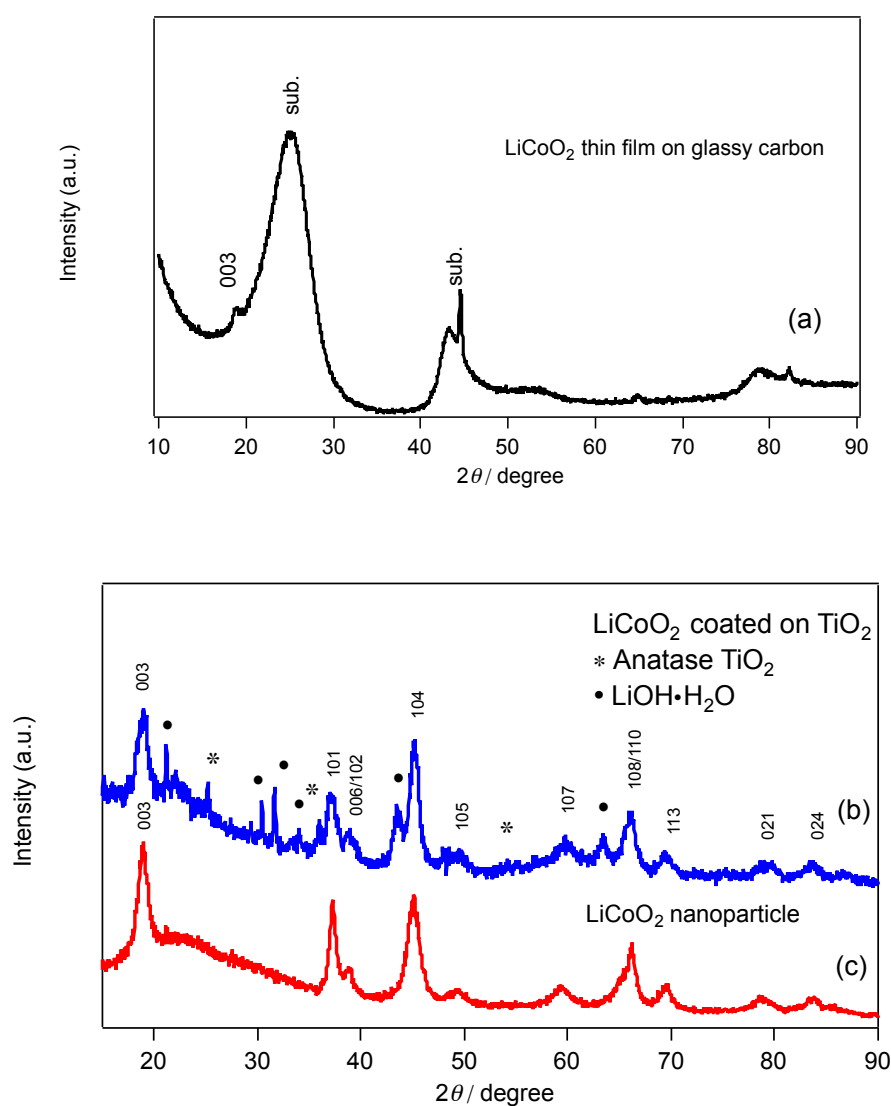


Figure 3.2 (a) XRD patterns for the LiCoO_2 film on the glassy carbon substrate and (b) The XRD pattern for LiCoO_2 coated on the particles of anatase TiO_2 powder. (c) LiCoO_2 nanoparticle synthesized by the electrostatic self-assembly deposition and the hydrothermal treatment.

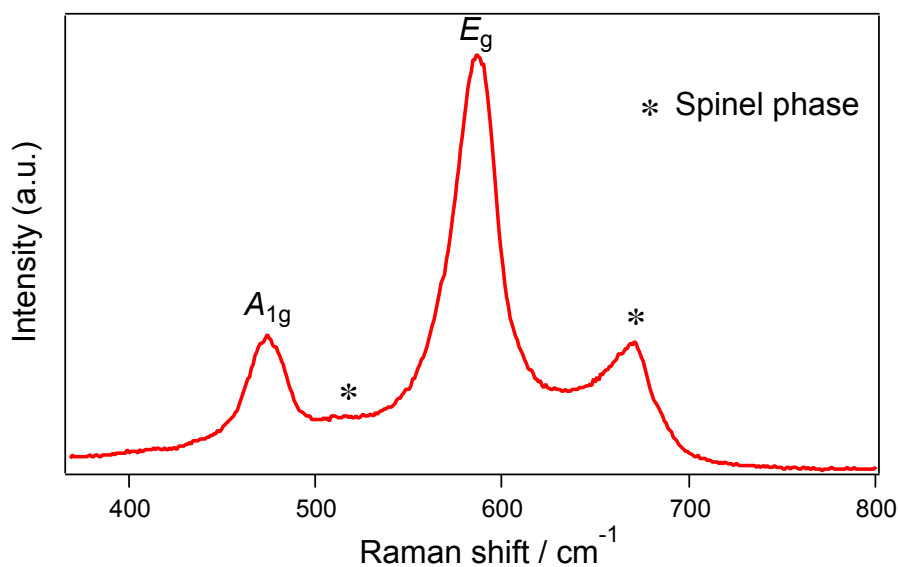


Figure 3.3 Raman spectra for LiCoO_2 film obtained by the electro-deposition for 5 min on the glassy carbon substrate.

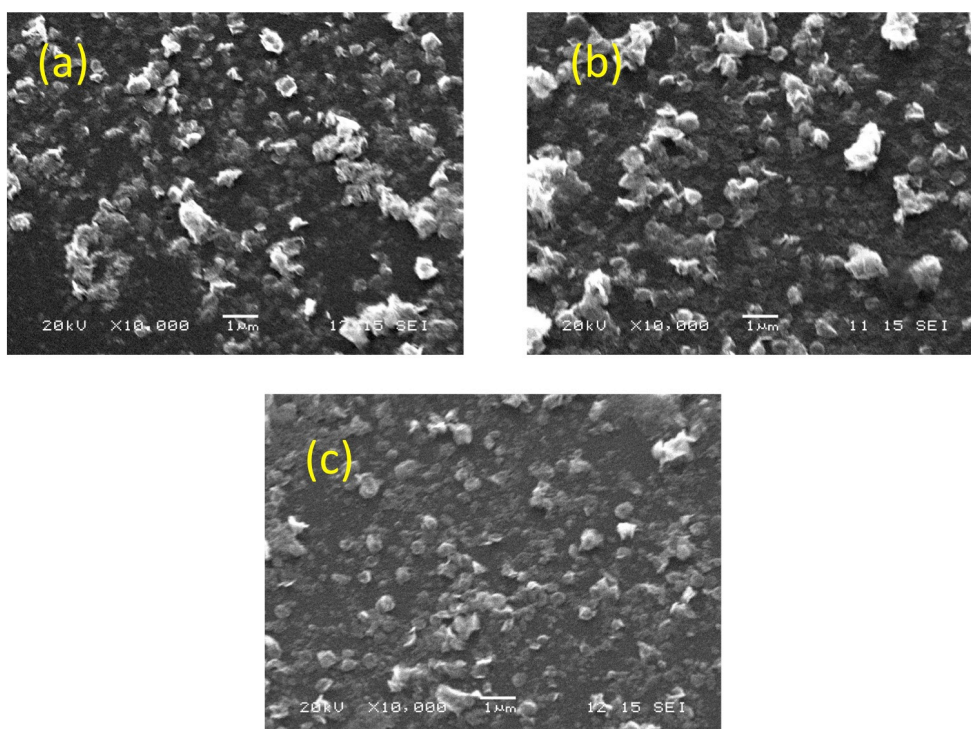


Figure 3.4 SEM images of the surface of LiCoO_2 film on the glassy carbon substrate obtained by various electro-deposition time: (a) 5 min, (b) 15 min, (c) 60 min.

Figure 3.4 shows the surface morphologies of LiCoO₂ films on glassy carbon substrates with the electro-deposition time of 5, 15 and 60 min, respectively. Increasing the electro-deposition time, the morphologies of the film surface changed evidently from rugged three-dimensional structure (Figure 3.4 a) to denser and smoother structure (Figure 3.4 c). In spite of the change of the surface shape with the deposition time, the size of secondly particle of these films is almost the same: about 1 μm.

The discharge curves for the LiCoO₂ films with various deposition time at the range of 3.6~4.2 V vs. Li with discharge current of 7.8 μA/cm² were shown in Figure 3.5 (a). The discharge plateaus, which are characteristic for LiCoO₂, were observed in the potential range of 3.9~4.0 V, and the capacity increased with the process time for electro-deposition. We roughly estimated the thickness of films from the discharge capacities, using the true density of LiCoO₂ 4.87 g/cm³ and theoretical capacity of LiCoO₂ 137 mAh/g. The estimated mass of the films was plotted in inset of Figure 3.5 (a) as a function of deposition time. The mass of the film and the deposition time are in a linear relationship at the depositing rate with 0.2 μg/min. In other words, we can handle the amount of the LiCoO₂ film by controlling electro-deposition time of precursor nanosheet. In Figure 3.5 (b), the capacity utilization efficiency of LiCoO₂ cathode films with various thickness is plotted as a function of logarithmic discharge current C-rate. Here, we assumed the capacity obtained at the discharge current 7.8 μA/cm² has 100% of utilization efficiency. Although the discharge capacity decreased with increasing the discharge current, the film with 5 min deposition sustained 72% efficiency at a very high rate of 300 C-rate. LiCoO₂ powder consisted of the nanoparticle with almost the size about 17 nm, which is the size reported to exhibit excellent high rate performance [6]. This demonstrates that a good electric contact can be obtained at the interface between the carbon substrate and LiCoO₂ film synthesized via the nanosheet restacking method and subsequent hydrothermal treatment and also that the short diffusion length of nanoparticle benefits for obtaining the high rate capability of the cathode materials. The

thicker films, on the other hand, showed poorer rate performance. Comparing the utilization efficiency of the LiCoO_2 film with deposition time of 5 min with the film deposition time of 60 min, thinner film showed 10 times higher discharge rate. This difference in discharge rate performance seems to be caused by the film surface morphology, which is dependent on the deposition time. As was observed in Figure 3.4, shorter electro-deposition time gave the film surface with much more holes and gaps. The large surface area obtained by the 3D structural surface would make the fast discharge reaction rate possible, on the other hand, thick film with the dense and flat surface has insufficient reaction area. For the further analysis of this electrode reaction, we carried out the electrochemical impedance spectroscopy (EIS) at various voltages in the discharge process.

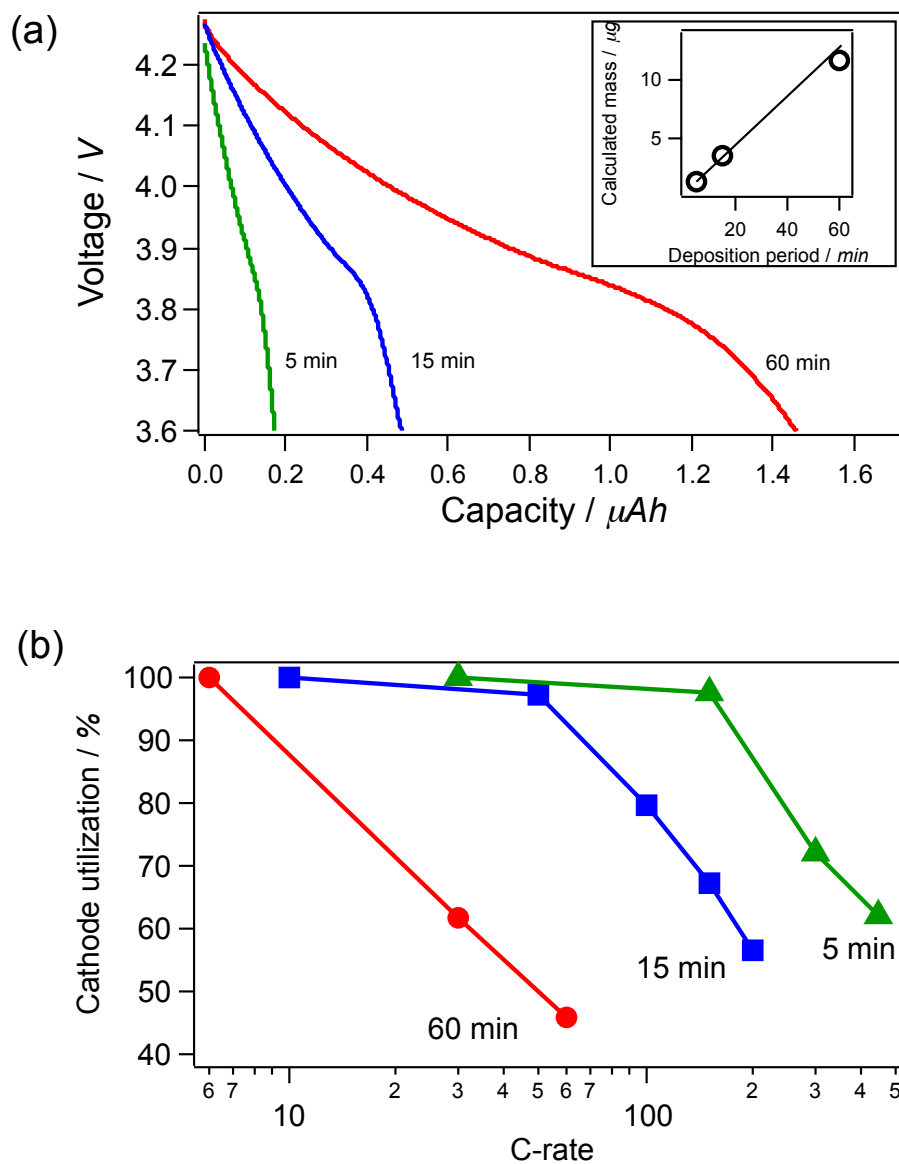


Figure 3.5 (a) Discharge curves of LiCoO₂ films on the glassy carbon substrate obtained by 5 min, 15 min, 60 min electro-deposition time with the discharge current of 7.8 $\mu A/cm^2$. (Inset) The relationship between the deposition time and the mass of the LiCoO₂ film estimated from the discharge capacity. (b) Discharge curves of LiCoO₂ films with various thickness at various discharging rates.

Figure 3.6 (a) shows the Nyquist plots for LiCoO₂ film electro-deposited for 5 min /EC-DEC with 1 M LiPF₆/Li cell at voltage range of 3.8~4.2 V. All curves consisted of two semi-circles at high and medium frequency region and straight line with 45° slope at lower frequency region. Two semi-circles are related to solid electrolyte interface (SEI) and charge-transfer resistance (R_{ct}), and the straight line is attributed to Warburg region [15]. It is clear that R_{ct} increased with insertion of Li-ion at discharge process (decreasing the cell voltages). Previously, our group reported the electrochemical property of the epitaxial LiMn₂O₄ thin film synthesized by pulsed laser deposition (PLD) method on various substrates [16]. In the EIS measurement, the Nyquist plots of epitaxial LiMn₂O₄ thin film showed similar tendency with LiCoO₂ thin film on glassy carbon substrate (Figure 3.6 a), but only one circle related to charge-transfer resistance observed at high and medium frequency region. For LiMn₂O₄ epitaxial thin film electrode, the effect of SEI resistance was very small in the electrochemical process because the epitaxial film has a very low surface roughness (few nano meters), small grain boundary and ordered orientation. On the other hand, as shown in Figure 3.4 (a), the rugged surface of LiCoO₂ film electro-deposited for 5 min on glassy carbon has large surface area so that the effect of SEI resistance cannot be ignored and another semi-circle appeared in high frequency region. Nyquist plots for LiCoO₂ films with 15 min and 60 min deposition time also showed similar tendency. The obtained impedance spectra were analyzed using the equivalent circuit shown in the inset of Figure 3.6 (a). Figure 3.6 (b) shows the relationship between the R_{ct} and cell voltage on the LiCoO₂ films/EC-DEC with 1 M LiPF₆/Li cell. The extent of R_{ct} increase was largely dependent on the film thickness: thicker film shows higher resistance in all the voltage range. The higher resistance with increasing film thickness seems to be caused by the decrease in electronic conductivity in the LiCoO₂ film. In the commercial Li-ion rechargeable batteries, electrodes contain 5 wt% of conductive additives, and for electrochemical measurement, up to 50 wt% of conductive materials are added in order to improve electronic conductivity [17].

However, the cell employed in our electrochemical measurement was assembled by using the as-synthesized LiCoO₂ film on the glassy carbon substrate. The electronic conductivity of LiCoO₂ film would decrease with increasing film thickness for no addition of the conducting aid.

Li-ion chemical diffusion coefficient D_{Li} in LiCoO₂ film can be estimated according to the equation $D = l^2 / \tau$ [18], where l is diffusion length and τ is diffusion time. We assume that the Li-ion diffusion length l is 13.8 nm, which corresponds to particle width along the <110> direction that was estimated from the full width at a half maximum of the XRD reflection in Figure 3.2 (c). Diffusion time τ is directly obtained from the simulated result. The estimated diffusion coefficients at 4.2 V are 2.91×10^{-13} , 3.32×10^{-13} and 5.78×10^{-13} cm²/s for the 5 min, 15 min and 60 min sample, respectively. These values were in the same order with the diffusion constant of nanocrystalline LiCoO₂ report by Okubo et al. [17] using EIS method. In spite of the scattering in the diffusion constants estimated in the present study, the diffusion coefficient is considered to be independent from the film thickness, because the simulated diffusion constants contain a certain extent of error [19].

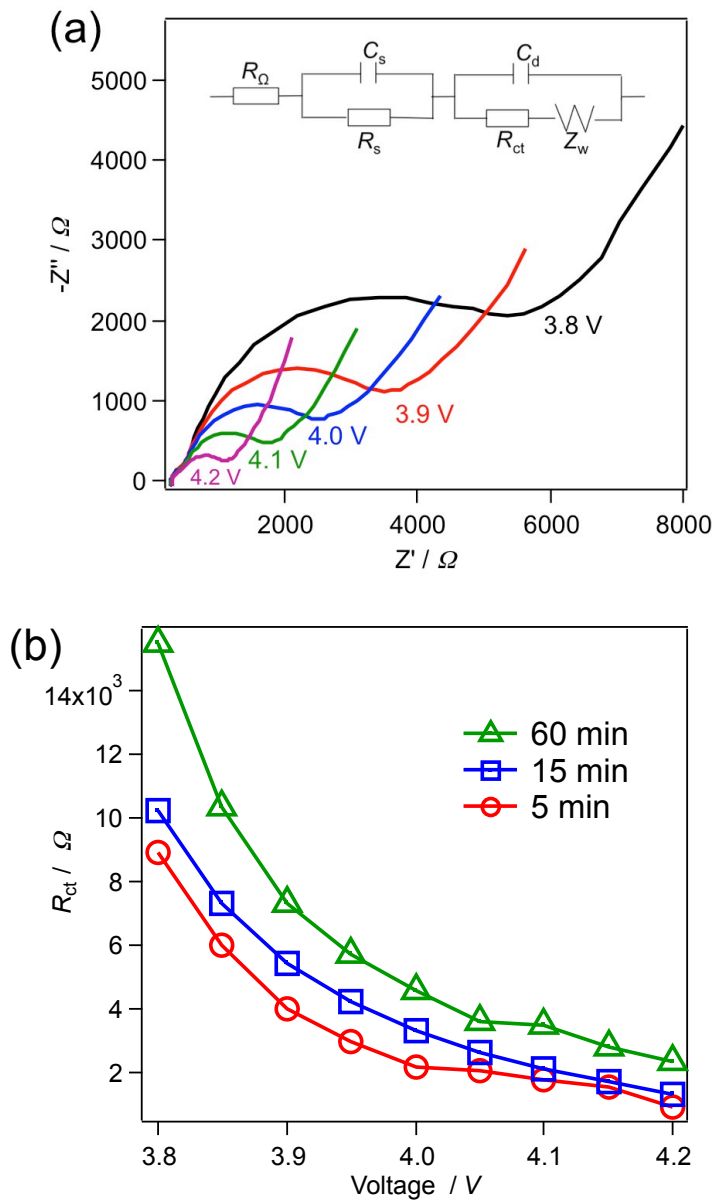


Figure 3.6 (a) Nyquist plots for the cell: LiCoO_2 film on glassy carbon substrate with 5 min deposition time/EC-DEC (7:3) with 1M LiPF_6/Li metal at various cell voltages. (b) The charge-transfer resistance R_{ct} of LiCoO_2 films plotted as a function of cell voltages.

3.3.2 LiCoO₂ coating on the surface of the powder materials

As discussed above, LiCoO₂ film that consists of nanosize particles, synthesized by nanosheet restacking method and subsequent hydrothermal treatment shows a high rate discharge capability on the carbon substrates. Furthermore, the thinner LiCoO₂ film has higher reaction surface and lower charge transfer resistance. Considering these advantages of LiCoO₂ nanoparticle synthesized via nanosheet restructuring method, this method would be appropriate to prepare a high rate charge-discharge battery system. For the improvement of the high rate capability, thinner film with lower charge-transfer resistance is desirable. However, reduction in the film thickness on the limited surface area of the glassy carbon substrate will sacrifice the discharge capacity, and the supports of cathode materials with much larger surface area is disable. As the next step, we have attempted at coating LiCoO₂ film on the surface of the conducting material fine powder. Carbon powders, in this paper, Toka Black powder (TB) and Denka Black (DB) powder were used, would be candidates of substrates because these nanosize carbons have much higher surface area, high electronic conductivity and their much lower cost is appropriate for the commercial battery use. In addition to these carbon powders, we also used semiconducting anatase TiO₂ powder for checking LiCoO₂ film coating on the support by the XRD measurement. The XRD measurement of the compounds coated on carbon is difficult for the high and broad background of the carbon support. For cobalt hydroxide nanosheet coating on the surface of powder anatase TiO₂, TB and DB, the electrostatic self-assembly deposition (ESD) method was employed instead of the electrophoretic deposition method used in previous section.

Figure 3.2 (b) shows the XRD pattern of LiCoO₂ coated on anatase TiO₂ powder by the ESD method. All of the main reflections agree with the reference of layered LiCoO₂ (JCPDS-16-0427). Other reflections are assigned to anatase TiO₂ support and LiOH impurity phase. The particle size of the LiCoO₂

estimated from 003 and 101 reflections with Scherrer equation are 25.9 and 36.6 nm, respectively. From these results, we have confirmed that nanosize LiCoO_2 was successfully synthesized on powder surface with nanosheet restacking method and subsequent hydrothermal reaction.

Surface morphologies of before and after coating LiCoO_2 on DB powder are shown in Figure 3.7 (a) and (b). The diameter of DB particle is about 100 nm. Figure 3.7 (b) is the SEM image of the LiCoO_2 coated DB. Smaller LiCoO_2 particles than DB are coated uniformly on the surface of DB. The particle size seen from SEM image roughly agrees with the grain size of LiCoO_2 nanoparticle estimated from the FWHM of XRD reflection in Figure 3.2 (b). On the other hand, LiCoO_2 particles were not found on the surface of the TB particle showed in Figure 3.7 (c), and same nanosize particles, which is supposed to be LiCoO_2 particle, presents as a separate particle. This difference in the surface condition would be caused by the extent of interaction between the nanosheet and carbon materials. In the first step of the nanosheet coating on the surface of the supports, nanosheets will be adsorbed on the surface that has affinity to the hydroxide nanosheet and then nanosheets will stack layer by layer. At the deposition process of nanosheets, DB powder was dispersed into the nanosheet dispersing 1-butanol solution, whereas TB carbon still deposited as a solid. This affinity of DB to 1-butanol would make adsorption of cobalt hydroxide nanosheets on the hydrophobic carbon material possible. In the case of TB, cobalt hydroxide nanosheets could not adsorb on the hydrophobic surface of TB without the aid of amphipathic 1-butanol and nanosheets deposited as a separate particle.

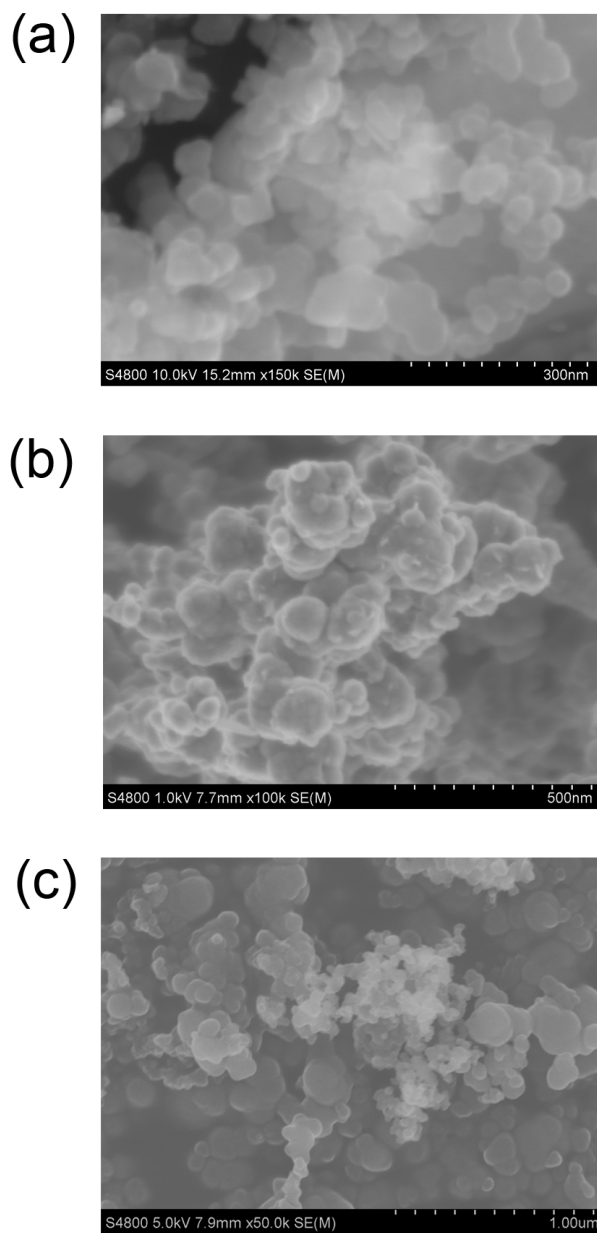


Figure 3.7 SEM images of the surface of (a) Denka Black powder, (b) LiCoO₂ coated Denka Black powder and (c) LiCoO₂ coated Toka Black powder.

To determine the weight ratio of LiCoO_2 and carbon powder in these composites, Thermogravimetric analysis (TGA) was carried out. Figure 3.8 shows the TGA diagram of two LiCoO_2 /carbon composites. For the sample of LiCoO_2 on DB (solid line), the mass of the sample decreased over 400°C , then a weight loss of 93.7% was observed when the sample was heated up to 700°C . This results indicated that there was 6.3 wt% of the LiCoO_2 coated on the surface of DB powder. Compared with the LiCoO_2 on DB, only 2.75 wt% of the LiCoO_2 coated on the TB powder (dashed line). Therefore, the coverage of LiCoO_2 on the TB carbon would much lower than that on DB because less amount of LiCoO_2 aggregated on the TB powder.

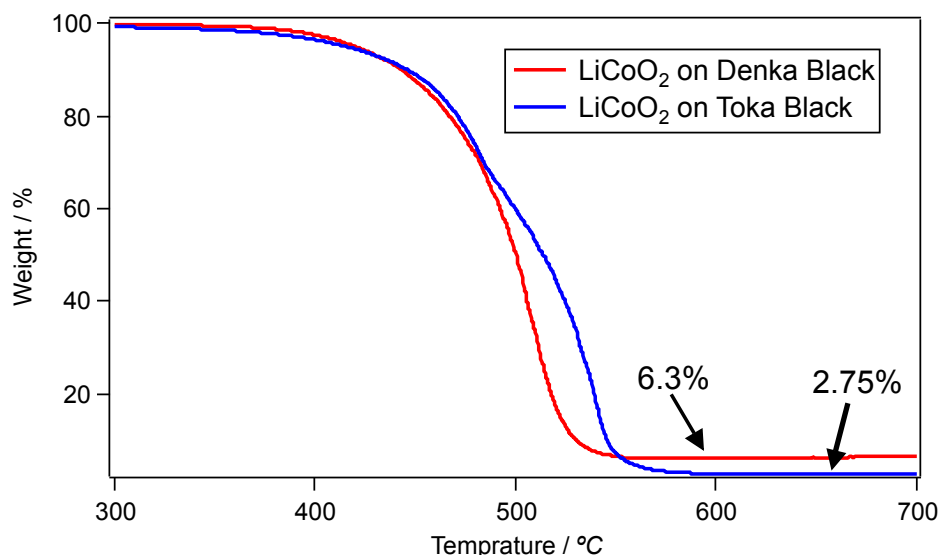


Figure 3.8 Thermogravimetry analysis (TGA) diagram of LiCoO_2 coated Denka Black and Toka Black carbon powder.

The charge-discharge curves of LiCoO_2 coated on TiO_2 and TB were shown in Figure 3.9 (a). The discharge voltage of $\text{LiCoO}_2/\text{TiO}_2$ shifted to lower voltage in both of charging and discharging processes compared with LiCoO_2/TB . This decrease in the voltage would be caused by the interaction between the semiconductor TiO_2 and LiCoO_2 . For both of TiO_2 and TB system, the

discharge capacity was larger than that for LiCoO₂ films on the glassy carbon substrate, while the plateau at 3.9 V disappeared. This disappearance of the plateau seems to be attributed to the poor electronic contact to LiCoO₂ nanoparticles. For TiO₂ support, the high interfacial resistance between TiO₂ and LiCoO₂ would have prevented the efficient electron transfer between TiO₂ and LiCoO₂. For LiCoO₂/TB system, (de-) intercalation reaction did not proceed efficiently for the insufficient contact with the carbon support caused by the aggregation of LiCoO₂ nanoparticles, as was observed in SEM image in Figure 3.7 (c). Thus, compare with theoretical capacity, only about 30% of the discharge capacity of LiCoO₂ was obtained. For the detailed discussion, further investigation of the surface contact is necessary.

Figure 3.9 (b) shows discharge curves with various discharge current for the LiCoO₂ coated on DB powder. By using DB as a support, the capacity was increased to 120 μ Ah that corresponds to 117mAh/g and voltage plateau at 3.9 V can be observed. This discharge capacity over 115 mAh/g under the comparatively high discharge current of 1.7 C is close to the practical capacity for bulk LiCoO₂. The capacity of LiCoO₂nanoparticle with same level of particle size was reported to be similar value. [6, 17] This discharge capability for LiCoO₂ nanoparticles on DB would be achieved by the excellent electronic conduction at the interface between DB and the uniformly coated nanosize LiCoO₂. Concerning the rate performance, 92.0%, 82.5%, and 66.0% of the capacity retained at 4.25 C, 8.5 C and 17 C in comparison with that at 1.7 C as plotted in inset of Figure 3.9 (b). This cathode utilization efficiency of the discharge capacity is superior to LiCoO₂ active materials synthesized by the conventional methods, *eg.* the highly porous LiCoO₂ film prepared by electrostatic spray deposition (ESD) method [2] and multi-walled carbon nanotubes (MWCNTs)/LiCoO₂ cathode active material using carbon nanotubes (CNTs) as the conductive additive [3]. Using carbon nanotube as conductive additive, the utilization of active materials of the cathode can be improved, 91% of discharge capacity was sustained at 3 C. Our results suggest that nanosize

LiCoO₂ coating on DB is a more effective way to improve the rate capability than adding highly conductive additive. Highly porous layered LiCoO₂ films with large surface area synthesized by electrostatic spray deposition method showed relatively high rate performance: 79% and 57% at 10 C and 20 C [2]. Our result is almost in the same level of cathode utilization to this highly porous layered LiCoO₂ films. Considering that our nanosize coating method does not require any apparatus and is easily applicable to the mass production, the uniform LiCoO₂ nanoparticles coating on the DB surface proposed in the present paper is a practical way for the rate capability improvement. However, as was observed in the SEM image of Figure 3.7 (b) and TGA data in Figure 3.8, the coverage of LiCoO₂ on the carbon surface was still not so high. If the LiCoO₂ cover the almost area of the DB surface homogeneously and thinly, rate discharge capability and its capacity would be greatly improved. Therefore, searching for more suitable supports and optimization of coating conditions would be necessary for the further development of this coating method.

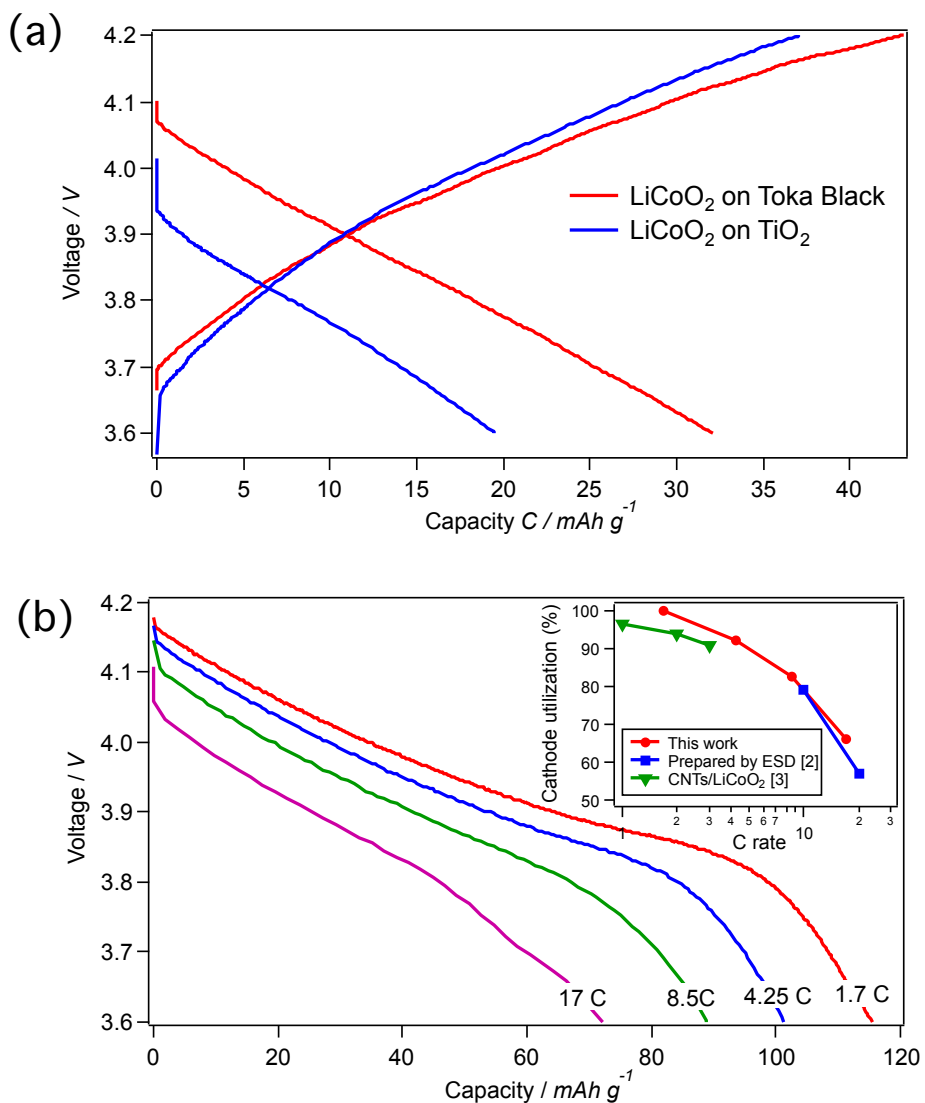


Figure 3.9 (a) Charge-discharge curves of LiCoO₂ on TiO₂ and Toka Black carbon with the applied current of 2 C. (b) Discharge curves of LiCoO₂ nanoparticle coated on Denka Black powder at various discharging rates. (Inset) Comparison of high rate capability of LiCoO₂ on Denka Black, highly porous layered LiCoO₂ prepared by electrostatic spray deposition [2] and carbon nanotube/LiCoO₂ composite [3].

3.4 Conclusion

LiCoO₂ consists of nanoparticles was successfully coated on the surface of DB powder by the electrostatic self-assembly deposition method and the hydrothermal treatment on the basis of the synthesis technique of LiCoO₂ films consist of nanoparticle on the glassy carbon substrate via the nanosheet deposition method. LiCoO₂ coated on DB showed a high rate charge-discharge capability due to the high electronic conduction between LiCoO₂ and DB powder. By further study in the mechanism of nanosheet deposition and restacking, this method will be able to prepare high rate cathode active materials for the lithium ion battery.

Reference

- [1] Q. Wu, W. Li, Y. Cheng, Z. Jiang, *Mater. Chem. Phys.* 91 (2005) 463.
- [2] S. Koike, K. Tatsumi, *J. Power Sources* 174 (2007) 976.
- [3] G. Wang, H. Li, Q. Zhang, Z. Yu, M. Qu, *J. Solid State Electrochem.* 15 (2011) 759.
- [4] J.K. Lee, S.J. Lee, H.K. Baik, H.Y. Lee, S.W. Jang, S.M. Lee, *Electrochem. Solid-State Lett.* 2 (1999) 512.
- [5] T. Matsumura, N. Imanishi, A. Hirano, N. Sonoyama, Y. Takeda, *Solid State Ionics* 179 (2008) 2011.
- [6] M. Okubo, E. Hosono, J. Kim, M. Enomoto, N. Kojima, T. Kudo, H. Zhou, I. Honma, *J. Am. Chem. Soc.* 129 (2007) 7444.
- [7] Wang, K. Takada, A. Kajiyama, M. Onoda, Y. Michiue, Zhang, M. Watanabe, T. Sasaki, *Chem. Mater.* 15 (2003) 4508.
- [8] L. Li, R. Ma, Y. Ebina, K. Fukuda, K. Takada, T. Sasaki, *J. Am. Chem. Soc.* 129 (2007) 8000.
- [9] M. Muramatsu, K. Akatsuka, Y. Ebina, K. Wang, T. Sasaki, T. Ishida, K. Miyake, M. Haga, *Langmuir* 21 (2005) 6590.
- [10] Y. Omomo, T. Sasaki, Wang, M. Watanabe, *J. Am. Chem. Soc.* 125 (2003) 3568.
- [11] Z. Quan, K. Iwase, N. Sonoyama, *J. Power Sources* 196 (2011) 6762.
- [12] R.J. Gummow, M.M. Thackeray, W.I.F. David, S. Hull, *Mater. Res. Bull.* 27 (1992) 327.
- [13] E.I. Santiago, A.V.C. Andrade, C.O. Paiva-Santos, L.O.S. Bulhões, *Solid State Ionics* 158 (2003) 91.
- [14] S.W. Song, K.S. Han, I. Sasagawa, T. Watanabe, M. Yoshimura, *Solid State Ionics* 135 (2000) 277.
- [15] P.J. Bouwman, B.A. Boukamp, H.J.M. Bouwmeester, P.H.L. Notten, *J. Electrochem. Soc.* 149 (2002) A699.
- [16] N. Sonoyama, K. Iwase, H. Takatsuka, T. Matsumura, N. Imanishi, Y. Takeda, R. Kanno, *J. Power Sources* 189 (2009) 561.

[17]M. Okubo, E. Hosono, T. Kudo, H.S. Zhou, I. Honma, Solid State Ionics 180 (2009) 612.

[18]M.D. Levi, G. Salitra, B. Markovsky, H. Teller, D. Aurbach, U. Heider, L. Heider, J. Electrochem. Soc. 146 (1999) 1279.

[19]J. Xie, N. Imanishi, T. Matsumura, A. Hirano, Y. Takeda, O. Yamamoto, Solid State Ionics 179 (2008) 362.

Chapter 4

Preparation of Nanocrystalline LiMn_2O_4 Thin Film by Electrodeposition Method and Its Electrochemical Performance for Lithium Battery

4.1 Introduction

In chapter 2, LiCoO_2 thin film consisted with nanoparticle synthesized by electrophoretic deposition (EPD) and hydrothermal treatment showed reversible charge-discharge ability even at 400 C discharge current [1]. However, the contact between thin film and current collector of obtained by EPD method is still insufficient for long cycle. It is need to improve in the cycle performance of the thin film while maintaining the high rate capability by more stable fabrication method.

Electrochemical deposition is another way to synthesis of thin film with the advantage of low synthesis temperature, low costs, and high purity in the product [2, 3]. This method also enables rigid control of film thickness, uniformity and deposition rate. Moreover, the good electric contact between the film and substrate is expected, because the product directly formed on the substrate electrochemically. For example, manganese dioxide cathodes synthesized by electrodeposition method are reported to show good electrochemical property for the application of super capacitors [4, 5] and lithium batteries [6, 7].

Among the cathode materials, LiMn_2O_4 is the promising candidate for the thin film battery, because the feature of low cost, environmentally benign and has 3D frame work that benefits for the Li ion diffusion [8, 9]. The synthesis techniques of LiMn_2O_4 thin films have been reported by many groups, such as, sol-gel method [10, 11], electrostatic spray deposition (ESD) [12, 13], radio

frequency (r.f.) magnetron sputtering [14, 15] and pulse laser deposition (PLD) [16, 17].

In the present study, LiMn_2O_4 thin film composed of nanoparticle is attempted to synthesize by electrodeposition of manganese oxide precursor and subsequent sintering treatment, and its electrochemical properties of the thin film were investigated.

4.2 Experimental

4.2.1 Synthesis and characterization of LiMn_2O_4 thin film on Au substrate

The synthesis process of LiMn_2O_4 thin film on Au substrate was shown in Figure 4.1. Manganese oxide precursor was deposited on anode Au substrate in the potentiostatic mode with an Au sheet as counter electrode. The pH of electrolyte solution containing 3 mol/L $\text{MnSO}_4 \cdot 5 \text{H}_2\text{O}$ (99%, Kishida chemical) was adjusted to be 2.3 by adding H_2SO_4 acid (98%, Kishida chemical), under flowing oxygen gas. Manganese oxide precursor film was electrodeposited on the Au substrate (1 cm \times 1 cm \times 0.01 cm) under the cathodic polarization of 1.7 V by oxidation of Mn^{2+} ion in the solution (kept at 40°C). The film thickness was changed by controlling the electric charge flowed (5, 10, 50 mili-coulomb) under the control of potentio-galvanostat (Hokuto HABF 501). The precursor covered ca. 0.65 cm² on the surface of Au substrate. Then the films were rinsed with distilled water, dried at room temperature followed by dipping 0.03 M LiOH (99%, High purity chemical) solution on the surface of the films. The LiMn_2O_4 thin films were prepared through sintering manganese oxide thin films at 750°C for 12 h under air atmosphere. The three as-prepared LiMn_2O_4 thin films with different film thickness were named as 5 mC, 10 mC and 50 mC, respectively, indicating the flowed electric charge of the electrodeposited precursor hereafter.

The crystal structure of the thin films were characterized by X-ray diffractometer (Ultima IV, Rigaku) using Cu $K\alpha$ radiation and Laser Raman

spectrophotometer (NSR-3300, JASCO) using DPSS laser at the wavelength of 532 nm. Electrochemical quartz crystal microbalance (ECQCM) controller (HQ 101D, Hokuto) was employed to measure the mass of the precursor by directly depositing on the gold surface (1.33 cm^2) coated on AT cut quartz 6 MHz of crystal. The morphologies of thin films were observed by the scanning electron microscope (SEM) (S-4800, Hitachi).

4.2.2 Electrochemical measurements

For electrochemical measurements, LiMn_2O_4 thin films on Au substrates were assembled in HS cell (Hohsen) with lithium metal as anode and 1M solution of LiPF_6 in EC:DEC (3:7, v/v) as the electrolyte. The charge–discharge and CV measurements were performed on potentiogalvanostat (Solartron 1280C). The electrochemical impedance spectroscopy (EIS) measurement was carried out with an impedance analyzer (Solartron 1255) connected to potentiostat (Solartron 1280C) over the frequency range from 10^6 Hz to 10^{-2} Hz at cell voltage with the applied voltage of 10 mV. All of the electrochemical measurements were carried out at 25°C .

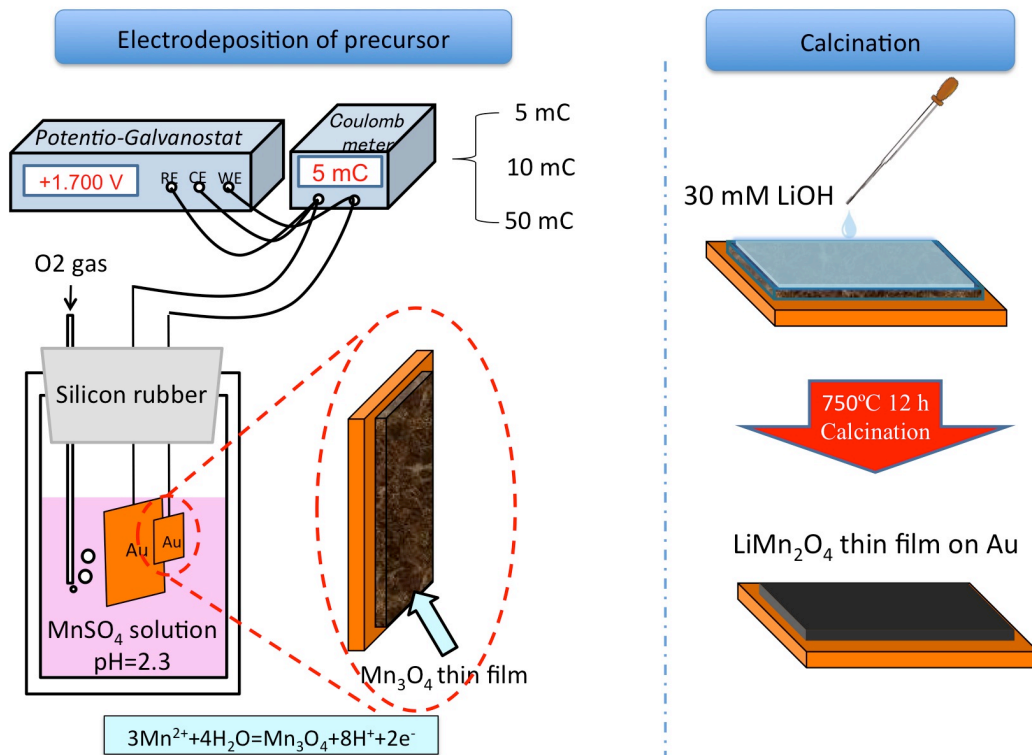


Figure 4.1 Synthesis process of LiMn_2O_4 thin film on Au substrate

4.3 Results and discussion

4.3.1 Characterization of the LiMn_2O_4 thin film on Au substrate

X-ray diffraction patterns for precursor and LiMn_2O_4 thin films were shown in Figure 4.2. For the XRD measurement, the manganese oxide precursor film was deposited under flowing 250 mC of electric charge in order to increase the intensity of the reflection. However, only indistinct peaks near 40° and 42° were observed. It might be due to the extremely small particle size or amorphous nature of the precursor. For the thin films reacted with LiOH at 750°C , three reflections appeared at 18° , 40° , 42° except the reflection of the Au substrate. The small reflection at 18° seems to be corresponding to the 111 reflection of spinel LiMn_2O_4 (ICSD No. 40485), but other reflections of spinel were too weak to confirm. The two sharp reflections at 40° and 42° , roughly agreed with MnO_2 phase. By Scherrer's equation, the crystallite sizes of the LiMn_2O_4 estimated from 111 reflection, were 51.3, 55.7 and 52.3 nm respectively. This result suggests that as-synthesized LiMn_2O_4 thin films composed of nanoparticle with the size of ca. 50 nm, and the particle size was independent of the electrodeposition time and thickness of precursor. Although the size of the LiMn_2O_4 nanoparticle obtained in this method was slightly bigger than 20~30 nm [18] compared with pulsed laser deposition method, it is much smaller than that of synthesized by other preparing roots, 100~200 nm for sol-gel method [11], 200 nm for laser spark atomizer method [19] or 10 μm for electrostatic spray deposition method [20]. In general, nano sized particle of the cathode thin film leads short Li ion diffusion length and large surface area to facilitate lithium diffusion in the host phase, so the LiMn_2O_4 thin film prepared by sintering electrodeposited precursor is expected to derive high rate charge-discharge performance.

The Raman spectra of the precursor on Au that electrodeposited by flowing 5, 10 and 50 mC are shown in Figure 4.3 (a). For the precursor of 50 mC, a

significant peak at 656 cm^{-1} and three smaller peaks at 309 cm^{-1} , 362 cm^{-1} , 478 cm^{-1} are indexed for the spinel structure of Mn_3O_4 with good agreement to the literature data [21, 22]. Absence of Mn_3O_4 reflection in the XRD pattern of the precursor indicates that the Mn_3O_4 electrodeposited on the Au substrate is amorphous state. Two weak bands at 510 cm^{-1} and 569 cm^{-1} were near the signals attributed to Mn-O lattice vibration in MnO_2 [21]. The presence of MnO_2 in the precursor phase is consistent with the result of XRD measurement. Although the RS spectra were weakened seriously, the similar pattern also observed in the precursor of 5 and 10 mC. Figure 4.3 (b) displayed the Raman spectra of the thin film reacted with LiOH at 750° C . All of the three thin films represented the same pattern with the similar peak intensity. The strongest band located at 623 cm^{-1} and two weak bands at 576 cm^{-1} and 480 cm^{-1} in accordance with the A_{1g} and F_{2g} modes of spinel LiMn_2O_4 [23]. Based on the XRD and RS spectra, it is demonstrated that amorphous Mn_3O_4 and a little amount of MnO_2 with low crystallinity were electrodeposited on the Au substrate according to the reaction (1) and (2).



In the sintering stage at air atmosphere, Mn_3O_4 reacted with LiOH to form LiMn_2O_4 though the MnO_2 remained as impurity and its crystallinity increased. Absence of other bands attributable to Mn_3O_4 or MnO_2 precursor in Figure 4.3 (b), indicates that the thin film mainly consisted of LiMn_2O_4 nanoparticle and contains just a little amount of MnO_2 as impurity.

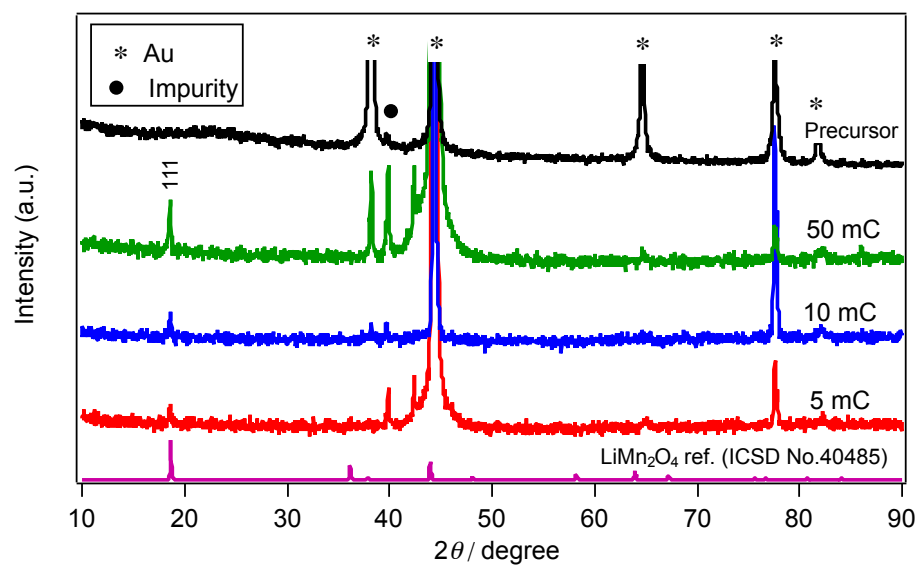


Figure 4.2 The XRD pattern of the precursor and LiMn₂O₄ thin films with various film thickness.

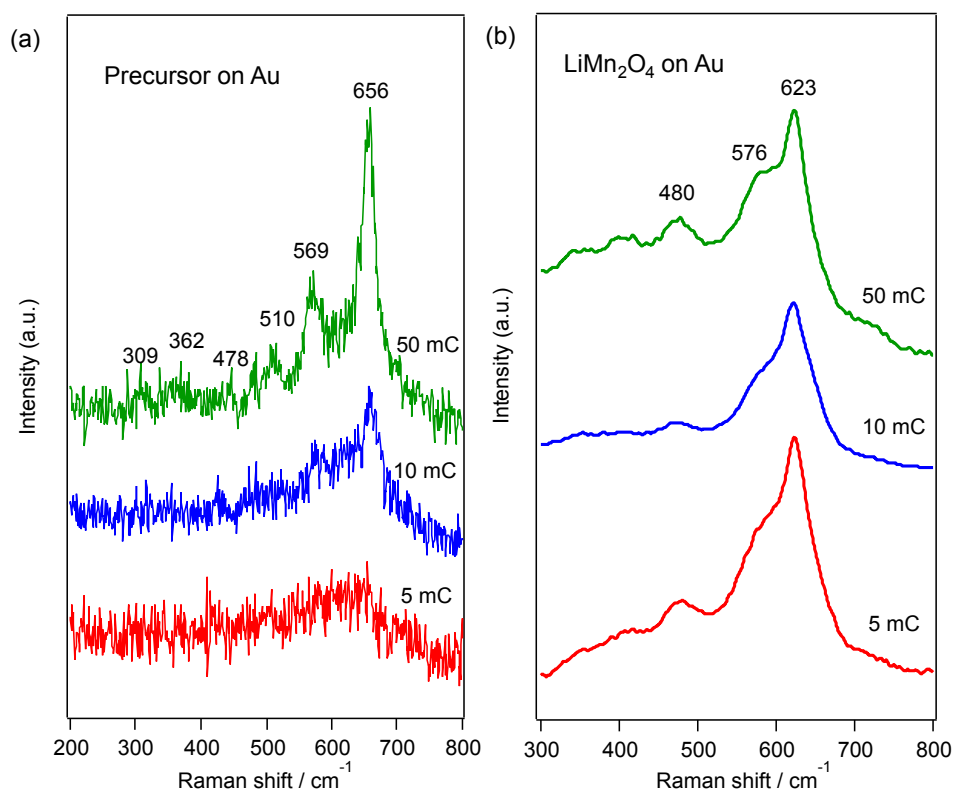


Figure 4.3 The Raman spectra of (a) precursor and (b) LiMn₂O₄ thin films with various film thickness on Au substrate.

The mass of the precursor films with various thickness was carefully measured by QCM method. In order to obtain the film with same thickness, 2 times of electric charge, 10, 20, and 100 mC was flowed due to the twice area of gold surface on crystal (1.33 cm²) of the each sample (0.65 cm²) for the electrochemical measurement. The mass of manganese oxide precursor was calculated by Sauerbrey equation (3):

$$\Delta f = -\frac{2f_0^2}{A\sqrt{\rho\mu}} \cdot \Delta m \quad (3)$$

Where f_0 is resonant frequency (Hz), Δf is frequency change (Hz), Δm is mass of deposited precursor (g), A is active crystal area (1.33 cm²), ρ is density of quartz (2.648 g cm⁻³), μ is shear modulus of quartz for AT-cut crystal (2.947×10^{11} g cm⁻¹ s⁻¹). We presumed that precursor film is composed of Mn₃O₄, and reacts with LiOH to form LiMn₂O₄ with 100% efficiency. The thickness of the thin film was roughly estimated from theoretical density of LiMn₂O₄ (4.3 g cm⁻³). The obtained mass and thickness were shown in Table 4.1. Very thin films were obtained for 5 and 10 mC sample with the thickness of ~10 and ~20 nm. This very small film thickness will contribute in decreasing in the resistance that will benefit for the acceleration of lithium (de) intercalation. As shown in Figure 4.4 (b), the mass of electrodeposited precursor was proportional to the flowed electric charge with the rate of 0.56 µg/mC.

Figure 4.5 showed the surface morphology of 5, 10, 50 mC sample observed by SEM. For the 5 mC sample shown in Figure 4.5 (a), very uniform thin film covered on Au substrate surface was observed. As deposition time increase, the thin film become thicker and denser as shown in Figure 4.5 (b) and (c). In addition, some aggregates of LiMn₂O₄ nanoparticles are distributed on the surface of 50 mC sample. These aggregates could hinder the smooth diffusion of Li⁺ and increase the resistance of thin film.

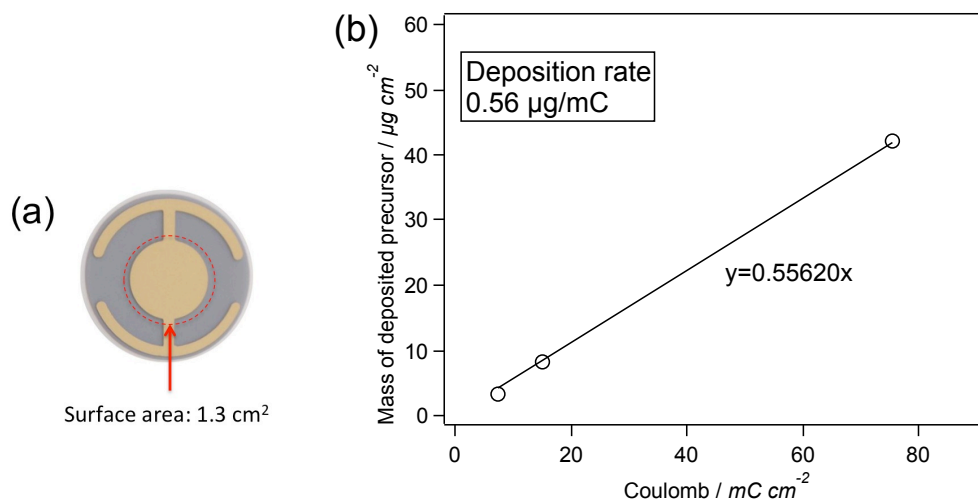


Figure 4.4 (a) The QCM electrode used in this study. (b) Relationship between mass of deposited precursor and flowing amount of electric charge.

Table 4.1 The mass of the precursor and LiMn₂O₄ thin film and estimated thickness.

	f_0 (Hz)	f_{MO} (Hz)	Δf (Hz)	Δm (μg)	M_{LMO} (μg)	T (nm)
10 mC	5966396.942	5966124.267	272.675	4.458	2.968	9.26
20 mC	5971099.213	5970430.051	669.162	10.940	9.046	22.70
100 mC	5965172.500	5961761.095	3411.405	55.775	46.123	115.90

* The density of LiMn₂O₄ was estimated at 4.3 g/cm⁻³. The f_0 , f_{MO} , Δf , Δm , M_{LMO} , T represent resonant frequency of crystal electrode, frequency of crystal electrode deposited by manganese oxide precursor, frequency change, mass of deposited precursor, mass of estimated LiMn₂O₄, thickness of LiMn₂O₄ thin film, respectively.

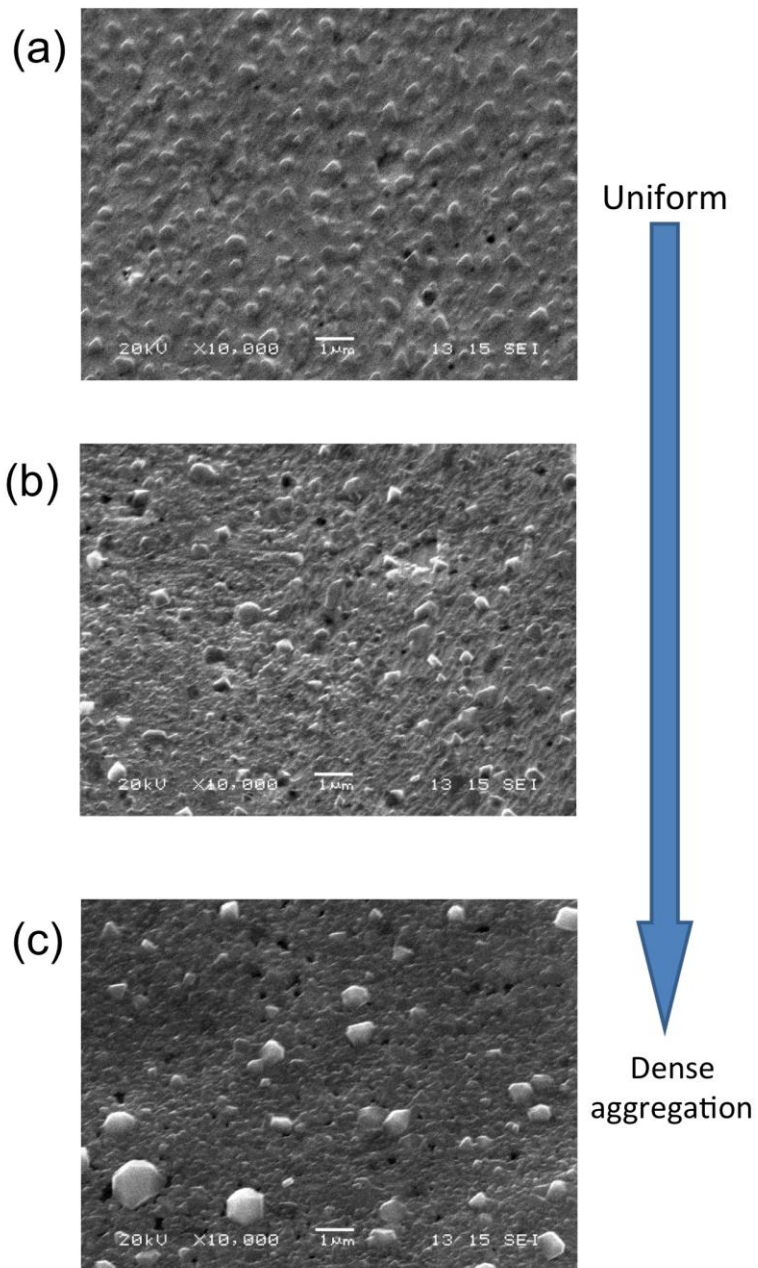


Figure 4.5 SEM image of surface morphology for (a) 5 mC, (b) 10 mC, (c) 50 mC sample.

4.3.2 Electrochemical properties of LiMn₂O₄ thin film on Au substrate

The high rate discharge performance of LiMn₂O₄ thin films with various film thickness was shown in Figure 4.6. The charge-discharge experiments performed with charge current of 10 $\mu\text{A}/\text{cm}^2$ and discharge current of 10, 100, 200 and 300 $\mu\text{A}/\text{cm}^2$ at the voltage range of 3.5~4.3 V. In Figure 4.6 (a-c), two clear plateaus are appeared at 4.16 V and 4.0 V in the discharge curves plotted at discharge current of 10 $\mu\text{A}/\text{cm}^2$ for the three samples. These two plateaus were characteristic with redox progress of LiMn₂O₄ [24]. The relationship between discharge capacity retention and current density was plotted in Figure 4.7. It should be mentioned that the capacity measured at low rate was a little higher than the maximum value for the 5 and 10 mC sample, but it is a reproducible phenomenon. A similar behavior was reported by Rougier et al. [25], and they explained that it was probably due to the interference from the interface between the film and current collector. Nevertheless, the 5 and 10 mC samples showed excellent high rate discharge performance: 104% and 98.2% of discharge capacity retained when the current density increased from 10 to 300 $\mu\text{A}/\text{cm}^2$ respectively. The discharge capacity essentially unchanged from 10 $\mu\text{A}/\text{cm}^2$ up to 300 $\mu\text{A}/\text{cm}^2$ and the two plateaus still can be observed until at high current density of 300 $\mu\text{A}/\text{cm}^2$ for the 5 and 10 mC samples. It has been widely acknowledged that the fade of the discharge capacity and disappearance of plateaus are due to the increasing cell polarization with the increase in current density that arises from the Li⁺ diffusion process. This high capacity retention would be attributable to the small particle size of LiMn₂O₄ thin film with short Li⁺ diffusion distance. For the thicker film of 50 mC sample, the discharge capacity was gradually decreased to 76 % of the initial capacity with increasing the discharge current to 300 $\mu\text{A}/\text{cm}^2$ and two plateaus tend to indistinct from the current of 200 $\mu\text{A}/\text{cm}^2$. From the capacity fading of 50 mC sample with the similar particle size of 50 nm, it can be conformed that the film thickness also play important role in high rate discharge performance in the case of film

electrode owing to the increase in electric resistance. In addition, the lithium intercalation/deintercalation process requires longer time to reach the equilibrium for the thicker film because larger amount of materials are contained than thinner films [25]. In the present study, thickness of the films with 5 and 10 mC samples estimated from the theoretical mass of LiMn_2O_4 was only 9.26 nm and 22.7 nm, respectively. This theoretical thickness lower than the particle size suggests the rough surface of the film and this is consistent with the surface SEM image shown in Figure 4.5 (a). For the further investigation of the high rate discharge performance of the thin films, CV measurements were carried out.

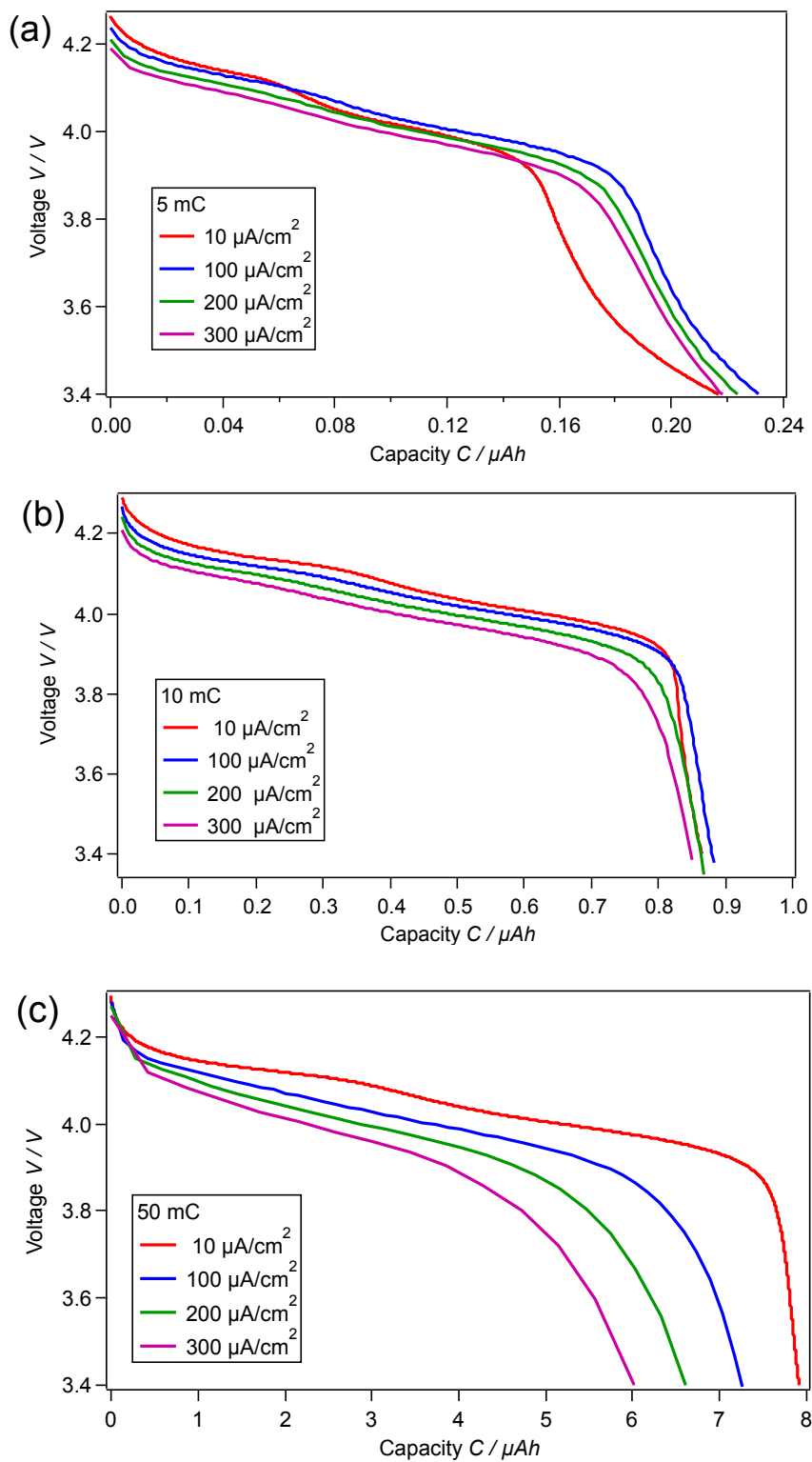


Figure 4.6 The charge-discharge curves with various discharge current of LiMn_2O_4 on Au substrate. (a) 5 mC, (b) 10 mC, (c) 50 mC.

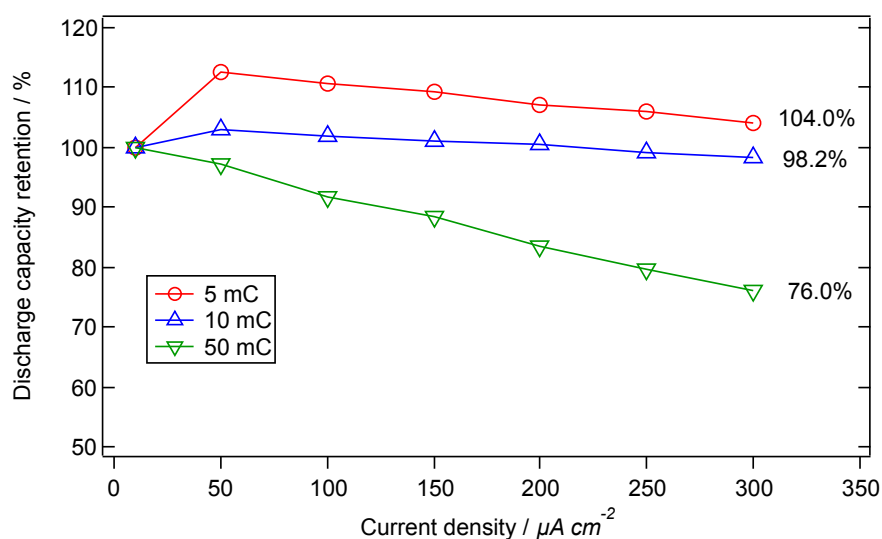


Figure 4.7 Relationship between discharge capacity retention and discharge current density.

Figure 4.8 (a-c) shows the cyclic voltammogram of $LiMn_2O_4$ thin film on Au substrate with various thickness recorded at the scan rate from 0.5 mV/s to 20 mV/s. The location of two peaks on charge and discharge are corresponding to the potential of plateaus, respectively. For the cyclic voltammetry plotted under the scan rate of 0.5 mV/s, the separation between a pair of peaks for three samples at 4.0 V is all about 30 mV. Previously, our group reported that the epitaxial $LiMn_2O_4$ thin film showed very small peak separation of 18 mV at the scan rate of 1 mV/s in the CV measurement associating to very low surface roughness, small grain boundary and ordered orientation [17]. Although the peak separation of the $LiMn_2O_4$ prepared in this work is a little bigger than epitaxial $LiMn_2O_4$ thin film, small ohmic drop in discharge curves and the high electric conductivity of the thin films are deserved for further electrochemical measurements [26].

It is well known that the change in peak shape with scan rate reflects the kinetics of Li^+ intercalation/deintercalation process. Well resolved reversible peaks both in the cathodic and anodic scan step until the high scan rate of 20

mV/s indicate good reversibility even at high rate redox reaction. Progressive shift of cathodic peaks in the discharge was observed with increasing scan rate ν as well as in height. The relationship of peak current change at 4.0 V of cathodic scan (corresponding to the plateau region at 4.0 V) and the root of scan rate was in Figure 4.9. For the thinner films of 5 and 10 mC samples, the cathodic current peaks increased in almost direct proportion to the potential sweep rate continued to 20 mV/s. This is typical behavior of the equilibrium at the intercalation electrode [12]. Comparatively, the peak current increased proportionally to square root of the scan rate $\nu^{1/2}$ for the 50 mC sample when the scan rate was faster than 10 mV/s, as shown in Figure 4.9, which is characteristic of a solid state diffusion controlled situation in the LiMn_2O_4 [27]. Based on a square root linear relationship between the peak current and the scan rate in the diffusion controlled region (10 mV/s~20 mV/s), diffusion coefficient of Li^+ into the 50 mC sample can be estimated from the classical Randles-Sevchik equation [28] as below,

$$I_p = 0.4663 F A C_R \left(\frac{n F \nu D}{RT} \right)^{1/2} \quad (4)$$

Where I_p is the peak current (A), F is the Faraday's constant, A is the surface area of the electrode (cm^2), C_R is the Li-ion concentration, n is the charge transfer number, R is the gas constant, T is the absolute temperature (K), D is the Li-ion chemical diffusion coefficient ($\text{cm}^2 \text{s}^{-1}$), and the ν is the scanning rate (V s^{-1}). As a result, the Li ion chemical diffusion coefficient estimated by the Eq. (4) is $2.516 \times 10^{-9} \text{ cm}^2/\text{s}$, which is higher than $10^{-10} \sim 10^{-11} \text{ cm}^2/\text{s}$ for the LiMn_2O_4 thin film prepared by PLD method [23] and $4 \times 10^{-10} \text{ cm}^2/\text{s}$ for r.f. sputtered LiMn_2O_4 films [29]. According to the previous reports, the chemical diffusion coefficient Li^+ ion in LiMn_2O_4 powder (ca. $10^{-9} \text{ cm}^2/\text{s}$) [30] is higher than that at PLD or r.f. sputtered LiMn_2O_4 thin film. The difference between the powder form and the thin film prepared by physical vapor deposition (PVD) technology was reported to be caused by the difference in static disorder or short chains with undistorted $16c-8a-16c$ Li ion diffusion pass [23]. In this work, the electrodeposited

manganese oxide precursor was sintered at elevated temperature with LiOH to form LiMn_2O_4 thin film, which is consisted of nanoparticle. It is considered that the LiMn_2O_4 thin film synthesized by electrodeposition and subsequent sintering method has some feature of power form, including high Li^+ ion diffusion coefficient. Therefore, it is considered that the high diffusion coefficient and short diffusion length led to the high rate discharge capability.

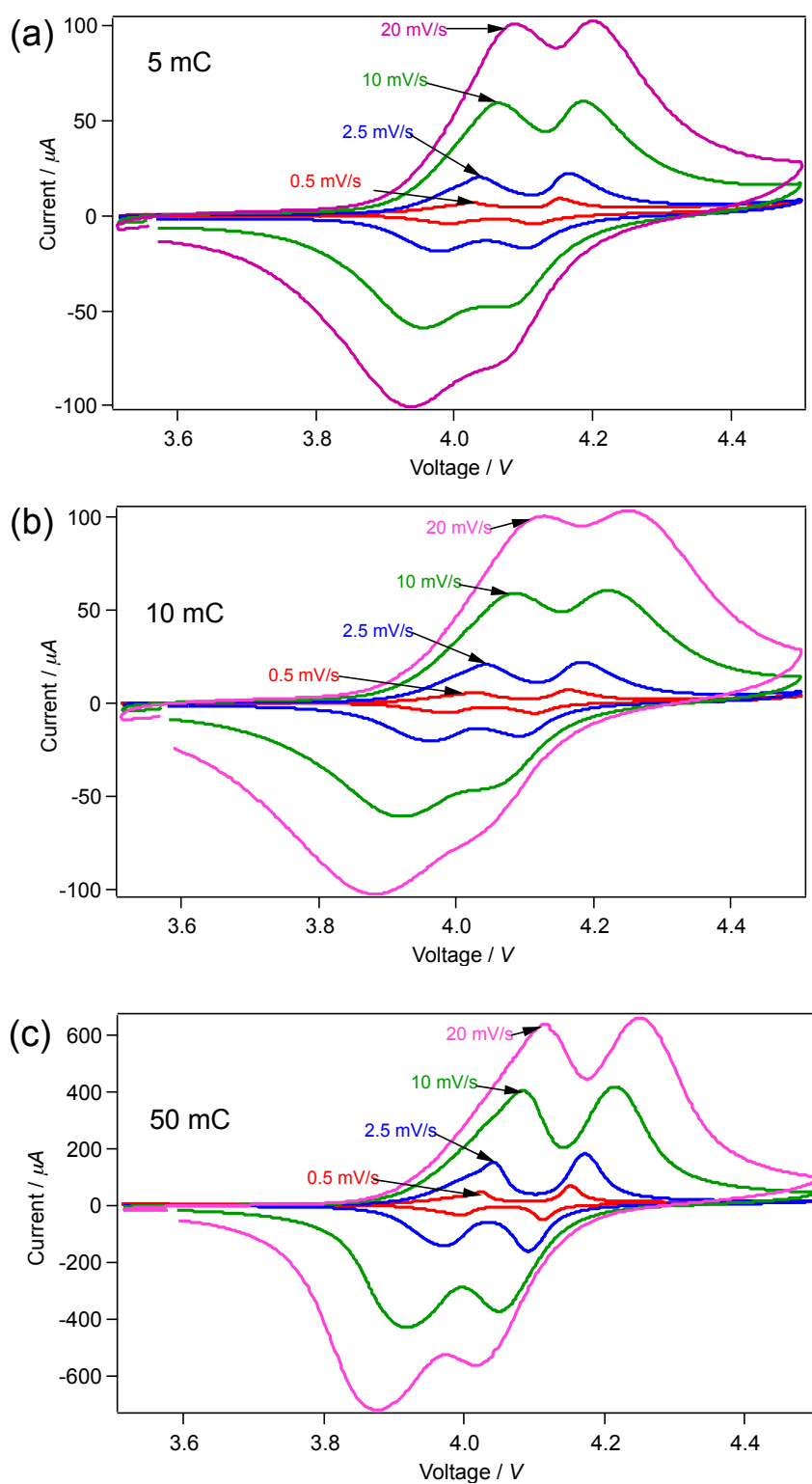


Figure 4.8 Cyclic voltammety curves of the LiMn_2O_4 at various scan rate of 0.5 mV/s to 20 mV/s. (a) 5 mC (b) 10 mC (c) 50 mC.

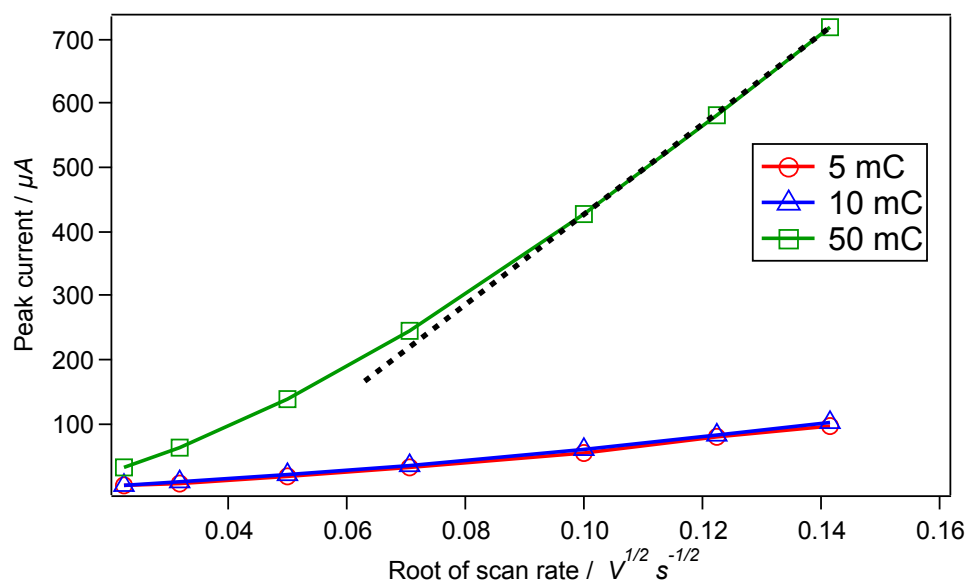


Figure 4.9 The relationship between peak current change at 4.0 V and the scan rate. The broken line indicates the slope of $I_p \propto v^{1/2}$.

Li ion diffusion coefficient in the 50 mC sample at 4.0 V was also estimated from electrochemical impedance spectroscopy. Nyquist plot in the frequency range of $10^6 \sim 10^{-2}$ Hz was shown in Figure 4.10. A semi-circle in high-middle frequency region and a straight line about 45° slope in the low frequency region were observed. The semi-circle in the high-middle frequency would be attributed to charge-transfer resistance and the straight line is attributed to Warburg region that related Li^+ diffusion in the bulk $LiMn_2O_4$ thin film [26]. Therefore, the Nyquist plot can be fitted using equivalent circuit that composed of R_Ω : bulk resistance of electrode, R_{ct} : charge-transfer resistant, C_d : double-layer capacitance, Z_w : Warburg impedance as shown in inset of Figure 4.10. The agreement of the solid line indicates the good fitting result. The chemical diffusion coefficient can be estimated from Eq. (5) [31]:

$$D_{Li} = \frac{1}{2} \left[\left(\frac{Vm}{FS\sigma} \right) \left(\frac{dE}{d\delta} \right) \right]^2 \quad (5)$$

Where Vm , F , S , σ and $dE/d\delta$ represent molar volume of $LiMn_2O_4$ (cm^3/mol), The Faraday's constant, the surface area of the electrode (cm^2), Warburg factor

and slope of the electrode potential E vs composition δ (V), respectively. The Warburg factor σ can be obtained from slop of real impedance Z' and frequency $\omega^{-1/2}$ that plotted in inset of Figure 4.10. The diffusion coefficient D_{Li} calculated from Eq. (5) is $1.49 \times 10^{-11} \text{ cm}^2/\text{s}$. This value is two orders lower than the result of CV measurement. In this case, the chemical diffusion maybe contains some error due to the unclear Warburg region (not strictly 45°). Nevertheless, the chemical diffusion coefficient of $10^{-9} \sim 10^{-11} \text{ cm}^2/\text{s}$ denoted high rate of the diffusion of Li ion in the bulk LiMn_2O_4 thin film.

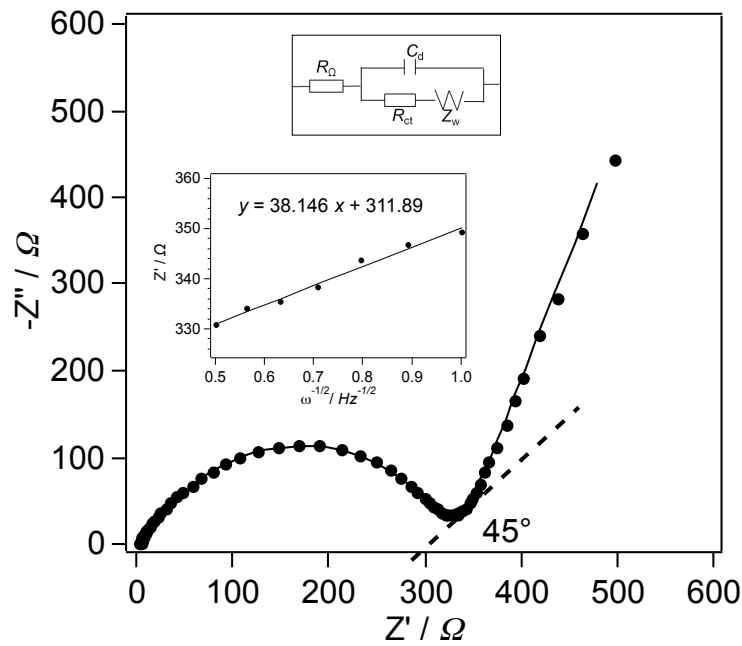


Figure 4.10 The Nyquist plot of 50 mC sample at 3.996 V at the frequency range of $10^6 \sim 10^{-2}$ Hz. (inset) The relationship between Z' and $\omega^{-1/2}$. The fitting model was also shown in inset.

The cyclability of LiMn_2O_4 thin films with various thickness was shown in Figure 4.11. The charge-discharge was carried out at the voltage range of 4.3 ~3.6 V with the charge-discharge current of $50 \mu\text{A}/\text{cm}^2$. It should be noted that, the thinner films of 5 and 10 mC samples showed superior cycle performance without capacity fading during 500 cycles while the discharge retention of 50mC sample gradually descend to 31.22 %. As was reported by Tang et al.[32], the thinner films with comparatively lower crystallinity may be able to endure the mechanical stress due to the volume change during charge-discharge process and show good cyclability.

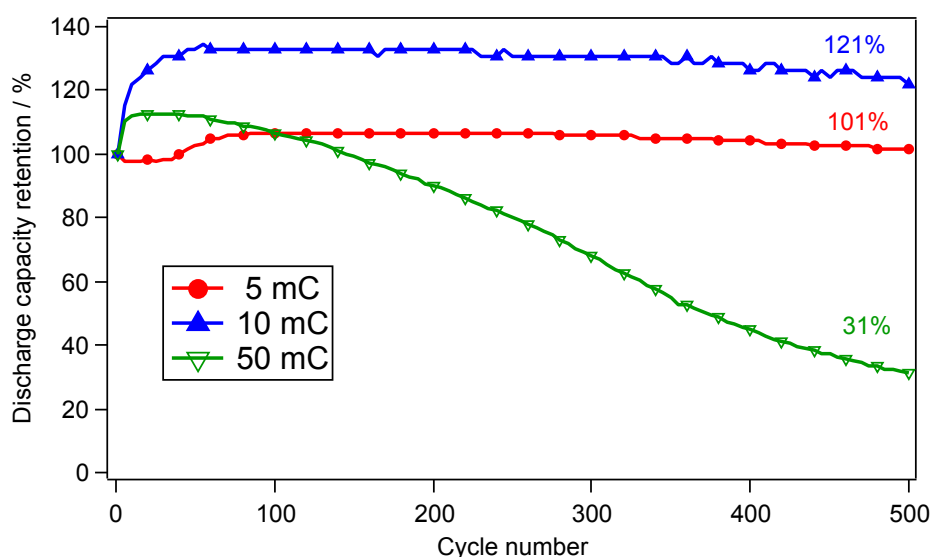


Figure 4.11 The comparison of the cycle performance for the LiMn_2O_4 with various film thickness.

4.4 Conclusion

LiMn₂O₄ thin films with various thickness were prepared by sintering electrodeposited manganese oxide precursor on the Au substrate. The LiMn₂O₄ thin films composed of nanoparticle with the size of 50 nm that independent of film thickness. In particular, thinner film derived excellent high rate performance and cyclability. Almost 100 % of the capacity preserved when discharge current density is raised from 10 $\mu\text{A}/\text{cm}^2$ to 300 $\mu\text{A}/\text{cm}^2$ and showed superior cycle performance without capacity fading during 500 cycles. From the CV and EIS measurement, it is confirmed that the LiMn₂O₄ thin film has good electric conductivity with substrate and high lithium diffusion coefficient of $10^{-9}\sim 10^{-11}$ cm^2/s .

Reference

- [1]Z. Quan, K. Iwase, N. Sonoyama, J. Power Sources 196 (2011) 6762.
- [2]J. Morales, L. Sanchez, S. Bijani, L. Martinez, M. Gabas, J.R. Ramos-Barrado, Electrochem. Solid-State Lett. 8 (2005) A159.
- [3]V. Georgieva, M. Ristov, Sol. Energy Mater. Sol. Cells 73 (2002) 67.
- [4]I. Zhitomirsky, M. Cheong, J. Wei, JOM Journal of the Minerals, Metals and Materials Society 59 (2007) 66.
- [5]D. Zhao, Z. Yang, L. Zhang, X. Feng, Y. Zhang, Electrochem. Solid-State Lett. 14 (2011) A93.
- [6]L. My Loan Phung, L. Thi Xuan Binh, P. Quoc Trung, N. Thi Phuong Thoa, Advances in Natural Sciences: Nanoscience and Nanotechnology 2 (2011) 025014.
- [7]S. Suzuki, K. Fujita, Y. Asami, F. Honma, JPN.Kokai Tokkyo Koho JP 61171062 (1986) A19860801.
- [8]M.M. Thackeray, W.I.F. David, P.G. Bruce, J.B. Goodenough, Mater. Res. Bull. 18 (1983) 461.
- [9]R.J. Gummow, A. de Kock, M.M. Thackeray, Solid State Ionics 69 (1994) 59.
- [10]Y.J. Park, J.G. Kim, M.K. Kim, H.T. Chung, W.S. Um, M.H. Kim, H.G. Kim, J. Power Sources 76 (1998) 41.
- [11]Y.J. Park, J.G. Kim, M.K. Kim, H.T. Chung, H.G. Kim, Solid State Ionics 130 (2000) 203.
- [12]M. Mohamedi, D. Takahashi, T. Itoh, M. Umeda, I. Uchida, J. Electrochem. Soc. 149 (2002) A19.
- [13]N. Anzue, T. Itoh, M. Mohamedi, M. Umeda, I. Uchida, Solid State Ionics 156 (2003) 301.
- [14]K.H. Hwang, S.H. Lee, S.K. Joo, J. Electrochem. Soc. 141 (1994) 3296.
- [15]S. Komaba, N. Kumagai, M. Baba, F. Miura, N. Fujita, H. Groult, D. Devilliers, B. Kaplan, J. Appl. Electrochem. 30 (2000) 1179.
- [16]M. Hirayama, N. Sonoyama, M. Ito, M. Minoura, D. Mori, A. Yamada,

- K. Tamura, J.i. Mizuki, R. Kanno, *J. Electrochem. Soc.* 154 (2007) A1065.
- [17]N. Sonoyama, K. Iwase, H. Takatsuka, T. Matsumura, N. Imanishi, Y. Takeda, R. Kanno, *J. Power Sources* 189 (2009) 561.
- [18]T. Matsumura, N. Imanishi, A. Hirano, N. Sonoyama, Y. Takeda, *Solid State Ionics* 179 (2008) 2011.
- [19]D. Singh, R. Houriet, R. Giovannini, H. Hofmann, V. Craciun, R.K. Singh, *J. Power Sources* 97-98 (2001) 826.
- [20]F. Cao, J. Prakash, *Electrochim. Acta* 47 (2002) 1607.
- [21]F. Buciuman, F. Patcas, R. Craciun, D. R. T. Zahn, *PCCP* 1 (1999).
- [22]T. Gao, H. Fjellvag, P. Norby, *Anal. Chim. Acta* 648 (2009) 235.
- [23]C. Julien, E. Haro-Poniatowski, M.A. Camacho-Lopez, L. Escobar-Alarcon, J. Jimenez-Jarquin, *Materials Science and Engineering: B* 72 (2000) 36.
- [24]T. Ohzuku, M. Kitagawa, T. Hirai, *J. Electrochem. Soc.* 137 (1990) 40.
- [25]A. Rougier, K.A. Striebel, S.J. Wen, E.J. Cairns, *J. Electrochem. Soc.* 145 (1998) 2975.
- [26]I. Yamada, T. Abe, Y. Iriyama, Z. Ogumi, *Electrochem. Commun.* 5 (2003) 502.
- [27]E. Levi, E. Zinigrad, H. Teller, M.D. Levi, D. Aurbach, E. Mengeritsky, E. Elster, P. Dan, E. Granot, H. Yamin, *J. Electrochem. Soc.* 144 (1997) 4133.
- [28]J. Xie, N. Imanishi, T. Matsumura, A. Hirano, Y. Takeda, O. Yamamoto, *Solid State Ionics* 179 (2008) 362.
- [29]K.H. Hwang, S.H. Lee, S.K. Joo, *J. Power Sources* 54 (1995) 224.
- [30]A. Dell'Era, M. Pasquali, *J. Solid State Electrochem.* 13 (2009) 849.
- [31]C. Ho, I.D. Raistrick, R.A. Huggins, *J. Electrochem. Soc.* 127 (1980) 343.
- [32]S.B. Tang, M.O. Lai, L. Lu, *Electrochim. Acta* 52 (2006) 1161.

Chapter 5

Synthesis and Electrochemical Property of Multiple Metal Oxide Nanoparticles as Cathode of Lithium Battery

5.1 Introduction

Lithium batteries are the most important energy storage source of electronic devices for the mobile systems. The performance of current lithium ion battery system is limited mainly by the cathode materials in many points (e.g, capacity, safety, etc.). Among them, serious points are low capacity, high cost and toxicity of cobalt, the main component. Iron based materials are excellent candidates for next generation electrode of lithium battery for its excellent characteristics, low cost, nontoxic and high energy power density. For iron oxides, control of the particle size is the key point for the improvement of electrochemical performance, because simple iron oxides exhibited poor reversibility due to the irreversible structure change during charge-discharge process induced by Li insertion. Since it has been reported that the capacity retention significantly improved by downsizing the iron oxide to nano size level[1, 2], iron oxides nanoparticles such as α -Fe₂O₃ [3], γ -Fe₂O₃ [4, 5], Fe₃O₄ [6, 7] are actively studied for the application of cathode material for lithium battery. Recently, Koo et al. reported hollow iron oxide nanoparticles, that contain high concentration of cation vacancy, show high capacity in high voltage region (~132 mAh/g at 2.5 V) and excellent stability (no fading until over 500 cycles) [8]. They emphasized the importance of cation vacancy that can efficiently improve the stability of structure. However, this kind of cathode is not suitable for the practical use, because the complicated preparation process for these materials raises its

production cost. On the other hand, there is a possibility that nano particles of other metal oxides and solid solutions with cation vacancies show high performance as cathode materials for lithium battery. In order to extend the scope for further improvement in the electrochemical property of metal oxide nano particles, the synthesis method of the oxide containing multiple metal ions and cation vacancy is desired.

Layered double hydroxides (LDH), represented in the general formula of $[M^{II}_{1-x}M^{III}_x(OH)_2] (A^{m-})_{x/m}$ are hydrotalcite-like materials with the structure based on brucite $Mg(OH)_2$ layered material [9, 10]. The brucite layers are positively charged because of partial substitution of M^{II} cation by M^{III} cation, and A^{m-} anion are inserted between the layers for the neutralization. LDHs have some attractive features as below. (1) Abundant kinds of metal cation and anion can be used as the component of the LDH: *e.g.* M^{II} : Ni^{2+} , Mg^{2+} , Zn^{2+} , Cu^{2+} , *etc.*, M^{III} : Fe^{3+} , Al^{3+} , V^{3+} , Co^{3+} *etc.*, A^{m-} : NO_3^- , Cl^- , CO_3^{2-} , *etc.* (2) The synthesis method of LDH is simple and low cost. Usually, LDHs are prepared in the alkaline aqueous solution containing M^{II} and M^{III} ion without any special equipment. (3) Calcination of LDH at low temperature gives rise to form the homogeneous solid solution of metal oxides with extremely small particle size and large specific surface areas [11, 12]. Additionally, some cation vacancy sites are generated during LDHs transformation to rock-salt metal oxide for the neutralization of the solid, because trivalent cations are partially substituted to the divalent cations: $\square_{1-x-y}M^{2+}_xM^{m+}_yO$, where \square indicates cation vacancy. The cation vacancies are expected to be utilizable as a diffusion path and storage sites of Li ion.

In this paper, electrochemical property of multiple metal oxides containing Mg^{II} , Ni^{II} , Fe^{III} and V^{III} ion (represent as Mg-Fe, Ni-Fe and Ni-V multiple oxides hereafter) prepared by calcination of the LDH precursors (represent as Mg-Fe LDH, Ni-Fe LDH and Ni-V LDH) were examined as cathode of lithium battery and the charge-discharge mechanism was also investigated.

5.2 Experimental

5.2.1 Synthesis and characterization of multiple metal oxide nanoparticles

All chemicals used in this study were purchased from Kishida chemical (GR grade). Three precursors of Mg-Fe LDH, Ni-Fe LDH, Ni-V LDH were synthesized by co-precipitation method using metal nitrate or chloride as starting materials. (See Table 5.1) The synthesis process of the LDH precursors and multiple metal oxide nanoparticles was shown in Figure 5.1. Aqueous solution containing 1 M NaOH and 0.1 M Na₂CO₃ was dropwised into the aqueous solution containing $M^{II}:M^{III}$ with ratio of 2:1, a total cation concentration of 0.6 M. The obtained gel was stirred violently for 12 h. After precipitating and washing with copious amounts of water, the obtained LDHs were dried at 120°C for overnight. Then the LDHs were calcined at 400°C for 12 h to obtain multiple metal oxides.

The X-ray powder diffraction (XRD) patterns were recorded on Rigaku RAD-C with Cu K α radiation. The morphology of powder samples was observed by scanning electron microscope (SEM, Hitachi S-4800) and transmission electron microscope (JEOL JSM z2500). Nitrogen adsorption-desorption measurements were performed on a micromeritics Tristar 3000 system. Elemental analyses for metal ion in the multiple metal oxides were carried out by multi-type inductively coupled plasma emission spectrometer (Shimadzu ICPE-9000). X-ray absorption spectroscopy measurements were performed at the BL-7C beam line with the electron storage ring operating at electron energy of 2.5 GeV and a stored current of 450 mA using Si (111) monochromator at High Energy Accelerator Research organization. For the measurement of Fe and V *K*-edge, the monochromator was detuned to 50% of its original intensity to minimize the harmonic-content of the beam. Energy calibration was carried out using the first inflection point of the spectrum of Ni, Fe and V metal foil as a reference. Each sample was mixed with acetylene black powder with the mass ratio of 1:1, and

then pressed to pellet shape for measurement.

5.2.2 Electrochemical measurements

The electrochemical performance of the multiple metal oxides was examined using CR 2032 coin cell at 25°C. The cathode electrode consisted of 32 wt% of active material, 64 wt% of acetylene black and 4 wt% of PTFE binder. Lithium metal was used as anode and 1 M LiPF₆ in EC:DEC (3:7 v/v) was used as electrolyte. Charge-discharge measurement was carried out in the potential range of 4.2 ~ 1.0 V with current of 10 mA/g controlled by a battery test system (interface model 0Z0-A19). Electrochemical impedance spectroscopy (EIS) measurement was performed using a potentiostat / galvanostat (VersaSTAT 4) in the frequency range 10⁻² to 10⁶ Hz with the applied AC potential of 10 mV to the cell voltage.

Table 5.1 Starting materials and synthesis condition of LDHs

LDH	Starting materials (purity)	Additional Condition
Mg-Fe	Mg(NO ₃) ₂ • 6H ₂ O (99%)	80°C
	Fe(NO ₃) ₃ • 6H ₂ O (99%)	
Ni-Fe	Ni(NO ₃) ₂ • 6H ₂ O (98%)	r. t.
	Fe(NO ₃) ₃ • 6H ₂ O (99%)	
Ni-V	NiCl ₂ •6H ₂ O (98%)	r. t.
	VCl ₃ (99%)	

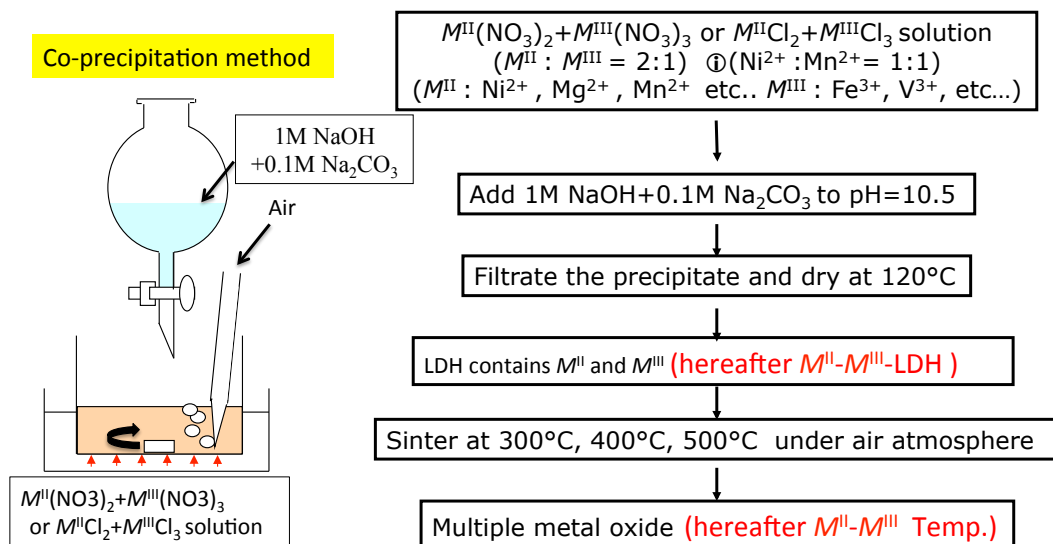


Figure 5.1 Synthesis process of LDH precursor and multiple metal oxide nanoparticles.

5.3 Results and discussion

5.3.1 Characterization of multiple metal oxide nanoparticles

Powder diffraction patterns of Ni-Fe LDH, Mg-Fe LDH and Ni-V LDH precursors were shown in Figure 5.2 (a). The similar XRD patterns of three samples, that are indexed for the rhombohedral $R\bar{3}m$ structure, are agreed with layered Mg-Al LDH (JCPDS No. 14-0191). In addition, the broader XRD reflections of Ni-V LDH than other two LDHs indicate the disordered nature of this material, that is consistent with the results other group proposed [13]. Figure 5.2 (b) are the XRD patterns of calcined LDH at 400°C. Only five reflections could be observed in the XRD patterns of Mg-Fe and Ni-Fe and these patterns agree with that of NiO with rock-salt structure (JCPDS No.01-1239). It is well known that M^{II} and M^{III} cations located homogeneously in the hydrotalcite (Mg-Al LDH) and calcination of hydrotalcite provides the solid solution with the

rock-salt structure where M^{II} and M^{III} cations are distributing homogeneously (Figure 5.3 a). Slight shift of reflection positions would be due to the different ion radii between Mg^{II} , Ni^{II} , Al^{III} and Fe^{III} . On the other hand, the reflection of Ni-V presented the pattern indexed for $\text{Ni}_3\text{V}_2\text{O}_8$ with orthorhombic $Cmca$ symmetry (JCPDS No. 37-0353). This compound is based upon $\text{Ni}_3\text{V}_2\text{O}_8$ has cubic closest packing of oxygen atoms, consisting of $[\text{NiO}_6]$ octahedral linked to $[\text{VO}_4]$ tetrahedral, whereas in the rock-salt structure, metal cation occupied octahedral sites as shown in Figure 5.3 (b) [14].

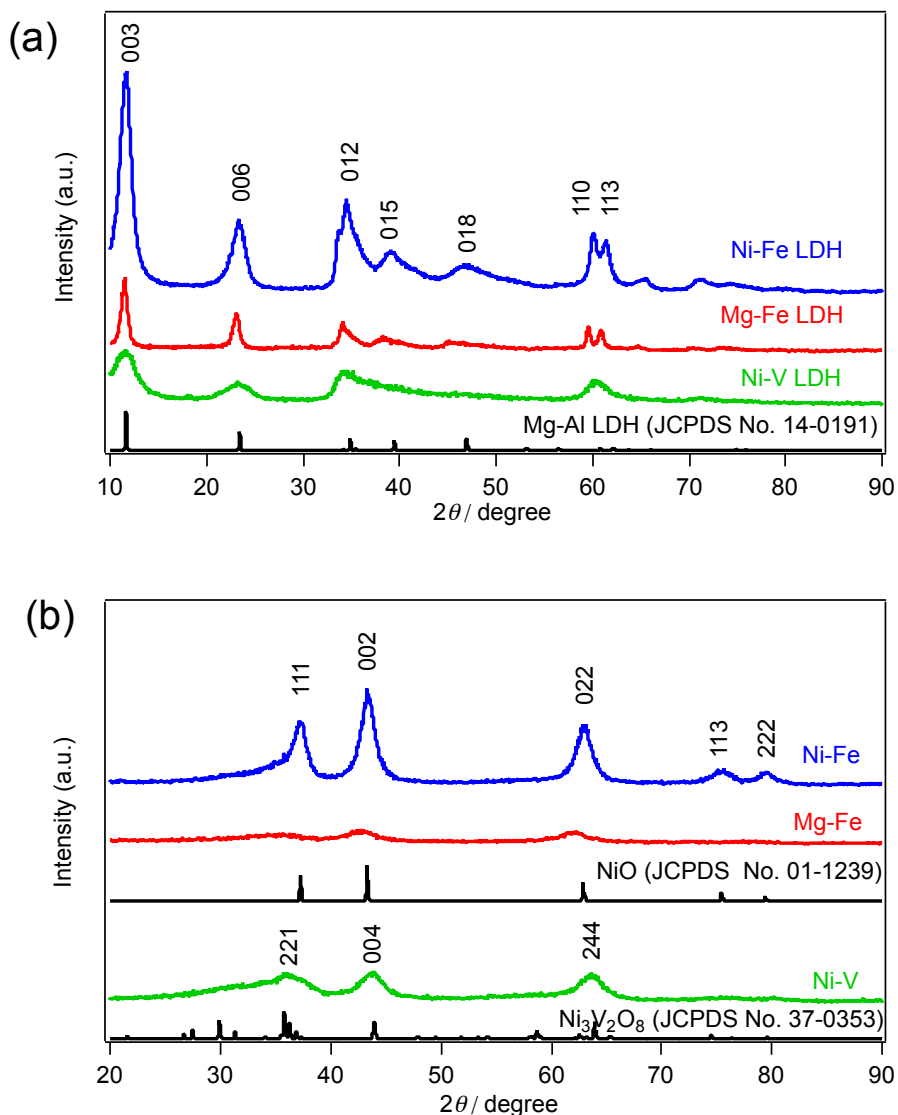


Figure 5.2 XRD patterns of (a) as-synthesized LDHs and (b) multiple metal oxides prepared by calcination of LDH at 400°C.

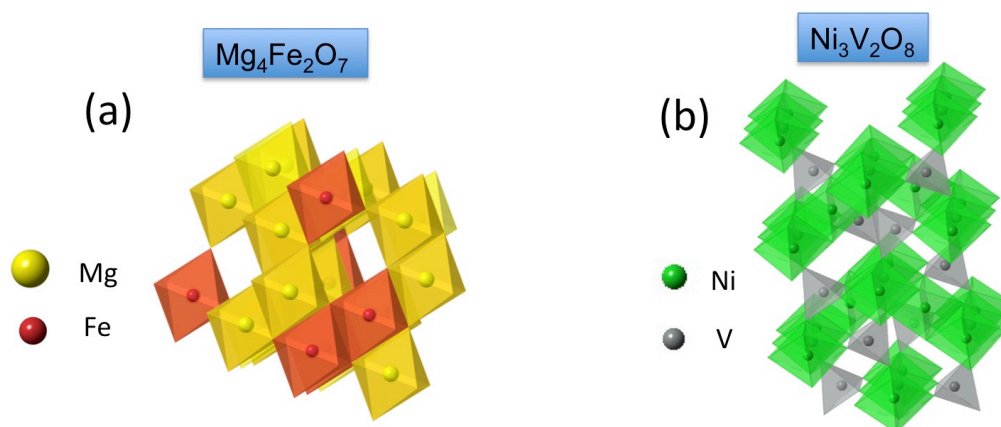


Figure 5.3 The structure of (a) $Mg_4Fe_2O_7$ and (b) $Ni_3V_2O_8$.

Figure 5.4 (a)-(c) showed SEM images of LDH precursors. The surface of LDHs looks like aggregates crumpled sheets and any definite shape was not observed. Figure 5.4 (d)-(f) is the TEM image of calcined multiple metal oxides. It clearly can be seen that multiple metal oxides consist of the uniform particles with the size from 8 to 20 nm. The specific BET surface area and particle size of three multiple metal oxides estimated from TEM images were summarized in Table 2. The multiple metal oxides that consist of nano size fine particles and have extremely large surface area over $110 \text{ m}^2/\text{g}$. This result demonstrates that nano sized fine particles of multiple metal oxides with large surface area can be obtained easily by simple calcination of LDH.

In order to determine the valence state of metal ion in multiple metal oxides, XANES measurement was carried out for the Mg-Fe, Ni-Fe and Ni-V samples in Figure 5.5. XANES spectra of as-prepared multiple oxides and standard samples are shown. As a result, we can confirm that divalent state of Ni in Ni-Fe and trivalent state of Fe in both Mg-Fe and Ni-Fe are maintaining the valence before calcination even after Fe^{3+} dissolution into the rock-salt NiO and MgO without any structural change of frame work. Figure 5.5 (d) and (e) showed XANES

spectra of Ni and V in Ni-V multiple oxide. For V *K*-edge, the absorption edge of Ni-V presents near that of V₂O₅, whereas for Ni *K*-edge, the absorption edge of Ni-V locates near that of NiO. The results demonstrated that Ni also maintains divalent state whereas V ion is oxidized to +5 during calcination of precursors. It is considered that highly oxidized V⁵⁺ could not dissolve into the NiO rock salt structure and forms Ni₃V₂O₈ as was observed XRD pattern in Figure 5.2 (b) [11].

In Table 5.2, the ratios of $M^{II}:M^{III}$ or $M^{II}:M^V$ that estimated by ICP measurement and the chemical formulas for multiple metal oxides are summarized. As we have surmised above, many cation vacancies are present in the compounds and these cation vacancies are expected to act as diffusion path and storage site of Li ion. If Li ion fully inserted to the cation vacancy, it is estimated that theoretical discharge capacities of 76.4, 81.5 and 151.4 mAh/g could be derived from the chemical formula of Ni-Fe, Mg-Fe and Ni-V, respectively.

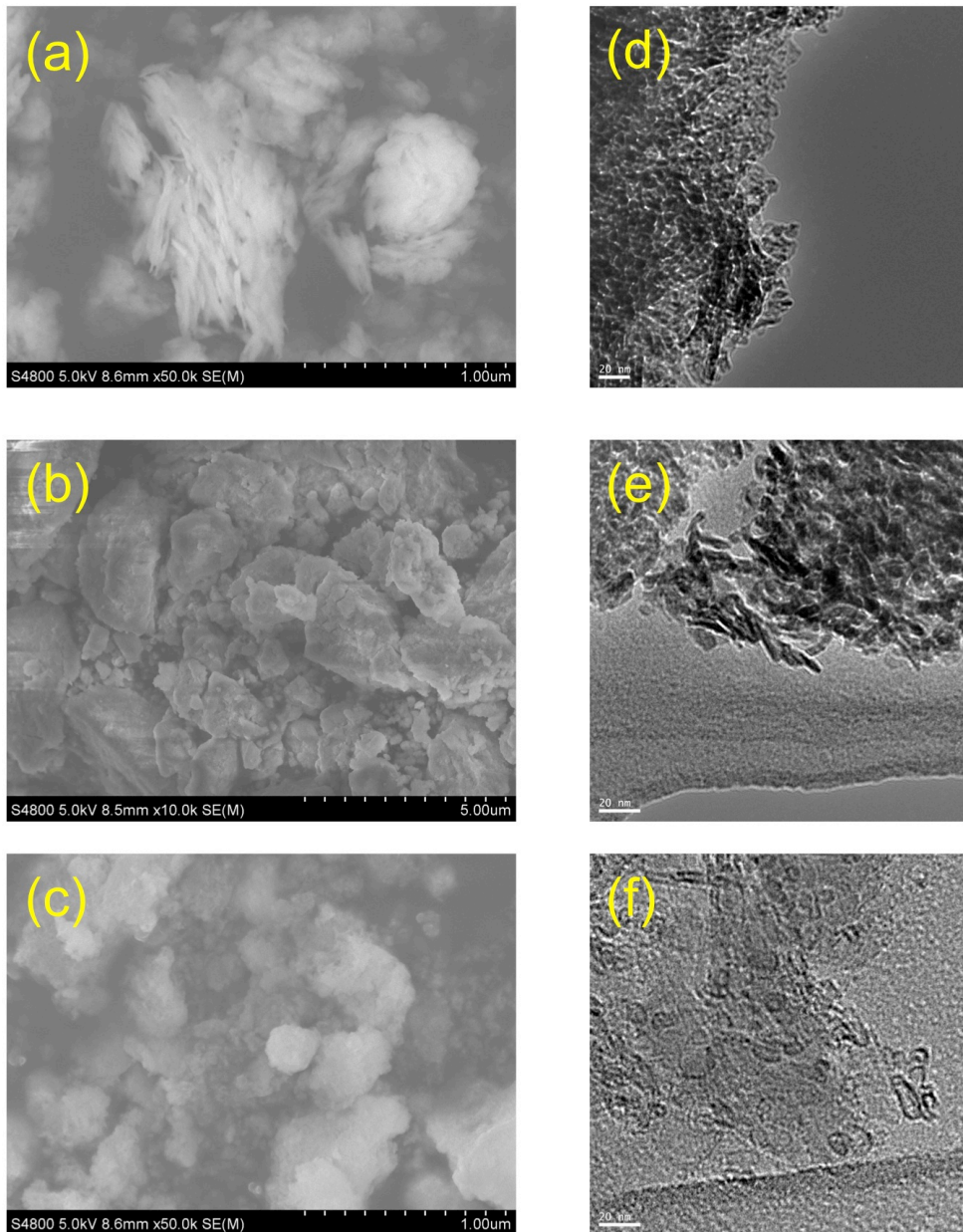


Figure 5.4 SEM images of as-synthesized LDHs (a) Ni-Fe LDH, (b) Mg-Fe LDH, (c) Ni-V LDH and TEM images of multiple metal oxides nanoparticles (d) Ni-Fe (e) Mg-Fe (f) Ni-V. The scale bar of TEM represents 20 nm.

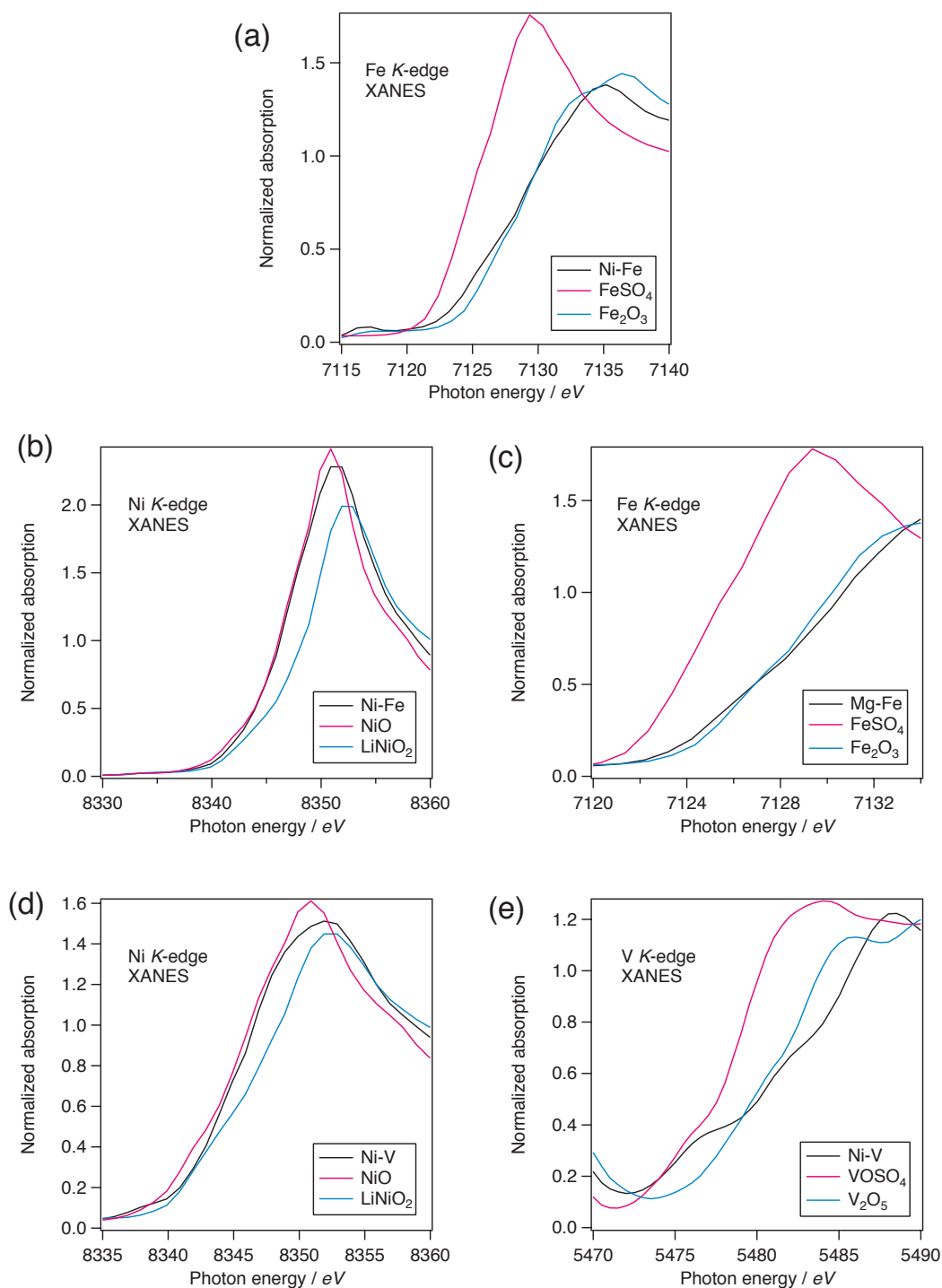


Figure 5.5 XANES spectra of as-prepared multiple metal oxide nanoparticles: (a) Mg-Fe at Fe *K*-edge, (b)-(c) Ni-Fe at Ni *K*-edge and Fe *K*-edge, (d-e) Ni-V at Ni *K*-edge and V *K*-edge.

Table 5.2 Chemical formula and characterization of multiple metal oxides

	$M^{\text{II}}:M^{\text{III}}$ or $M^{\text{II}}:M^{\text{V}}$	Chemical formula* (□: vacancies)	Theoretical intercalation capacity (mAh/g)	Particle size estimated from TEM (nm)	BET specific surface area (m ² /g)
Ni-Fe	1.34 : 1	□ _{0.18} Ni _{0.47} Fe _{0.35} O	76.4	14	121.3
Mg-Fe	2 : 1	□ _{0.14} Mg _{0.57} Fe _{0.29} O	81.5	9	120.5
Ni-V	2.28 : 1	□ _{0.31} Ni _{0.48} V _{0.21} O	151.3	20	110.5

*: □ represents cation vacancies. The chemical formula was normalized by stoichiometric coefficient of oxygen as unity.

5.3.2 Electrochemical property of multiple metal oxide nanoparticles

The charge-discharge curves of Mg-Fe, Ni-Fe, Ni-V in the voltage range of 4.2~1.0 V were shown in Figure 5.6 (a) to (c). In the first discharge, the cell potential of three samples decreased rapidly from the open circuit voltage to 2.5 V. From 2.5 V, a plateau-like step appeared around 1.7 V and a smooth voltage drop follows that until 1.5 V. Subsequently, the second plateaus appeared around 1.2 V. The first discharge capacity until 1V of Mg-Fe, Ni-Fe and Ni-V multiple metal oxide nanoparticles reached 254, 261 and 369 mAh/g, respectively. It should be noted that the theoretical Li insertion capacities are corresponding to the capacities for the steep voltage-dropping region until 1.5 V. (76.4, 81.5 and 151.4 mAh/g for Mg-Fe, Ni-Fe and Ni-V, respectively). Larcher et al. proposed that Li^+ inserted to the corundum $\alpha\text{-Fe}_2\text{O}_3$ nanoparticle until 1.5 V without phase transformation [3]. Koo et al. reported that Li intercalation to the cation vacancy site of hollow iron oxide nanoparticles without structural change occurred above 1.5 V [15]. On the assumption that lithium insertion voltage of compounds prepared in this study is almost same to these iron oxide nanoparticles, it is considered that the cation vacancy sites were almost fully utilized as the storage site of Li ion in the discharge until 1.5 V.

In Figure 5.7, relationship between cycles and discharge capacity was plotted. Some irreversible capacity observed at first charge process. For Mg-Fe and Ni-V, a little capacity fading was observed after second cycle, though large reversible capacity of 166 mAh/g and 327 mAh/g was obtained. This large charge-discharge capacity and good capacity retention shows the potential of the multiple metal oxide nanoparticles for the use of high capacity cathode for Li ion battery. For Ni-Fe oxide nanoparticle, the high discharge capacity over 250 mAh/g was retained to only until 4th cycle, and the capacity decreased to 143.56 mAh/g at 10th cycle. As shown in Table 5.2, the cation ratio of Ni^{2+} and Fe^{3+} in Ni-Fe oxide nanoparticle is 1.34:1. The lower M^{II} and M^{III} cation ratio than

Mg-Fe and Ni-V means the higher concentration of redox cation in the multiple metal oxides. In charge-discharge process, the larger volume change caused by higher concentration of Fe^{3+} cation could induce the instability of Ni-Fe structure, and the cycle retention was faded gradually.

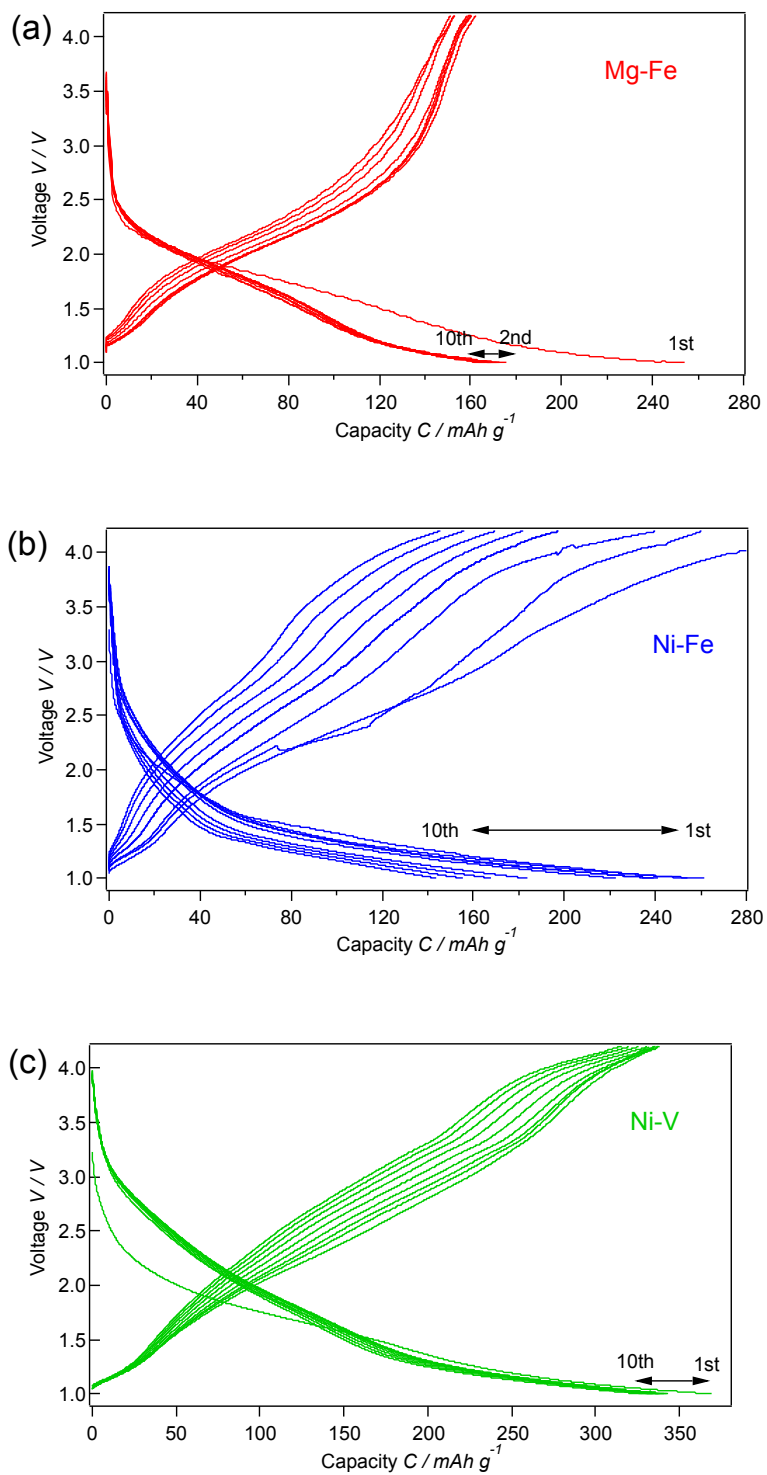


Figure 5.6 The results of charge-discharge measurements of (a) Mg-Fe, (b) Ni-Fe, (c) Ni-V. Current density was 10 mA/g for charge and discharge.

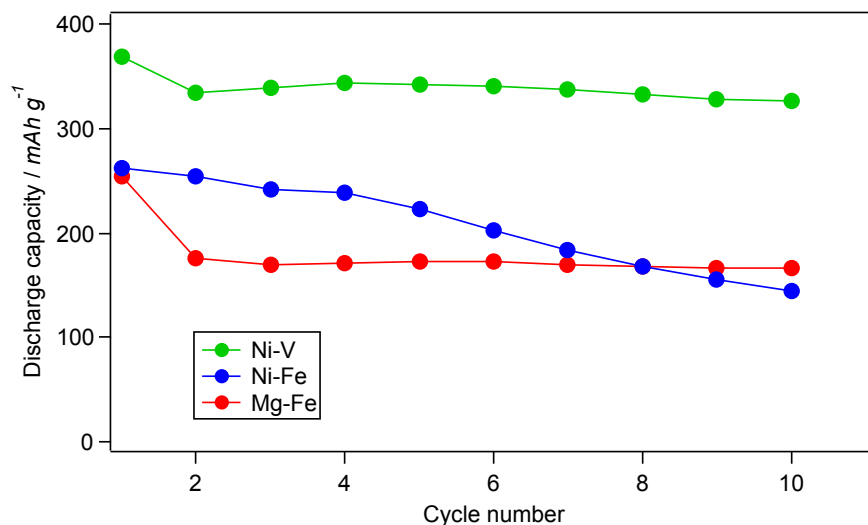


Figure 5.7 Capacity retention of three samples.

5.3.3 Reaction mechanism based on the ex-situ XRD and the AC-impedance measurement results

To confirm charge-discharge reaction mechanism for multiple metal oxide nanoparticles, ex-situ XRD measurements after first discharge to 1 V and one cycle discharge-charge to 4.2 V were carried out. We focused on the 022 reflection of Ni-Fe and Mg-Fe and 244 reflection of Ni-V near 63° as the target reflection because the highest 111 and 002 reflections overlapped with the cell reflection. In Figure 5.8, the XRD patterns for (1) before discharge, (2) after first discharge to 1 V and (3) after discharge-charge to 4.2 V were shown. For all samples, the target reflections shifted to lower angle after first discharge and returned to initial position again after following charge process. This result indicates that the lattice expands and shrinks reversibly during Li⁺ (de-)intercalation without significant structural change including the voltage region 1.5~1.0 V where some reaction other than lithium insertion into cation vacancy seems to proceed.

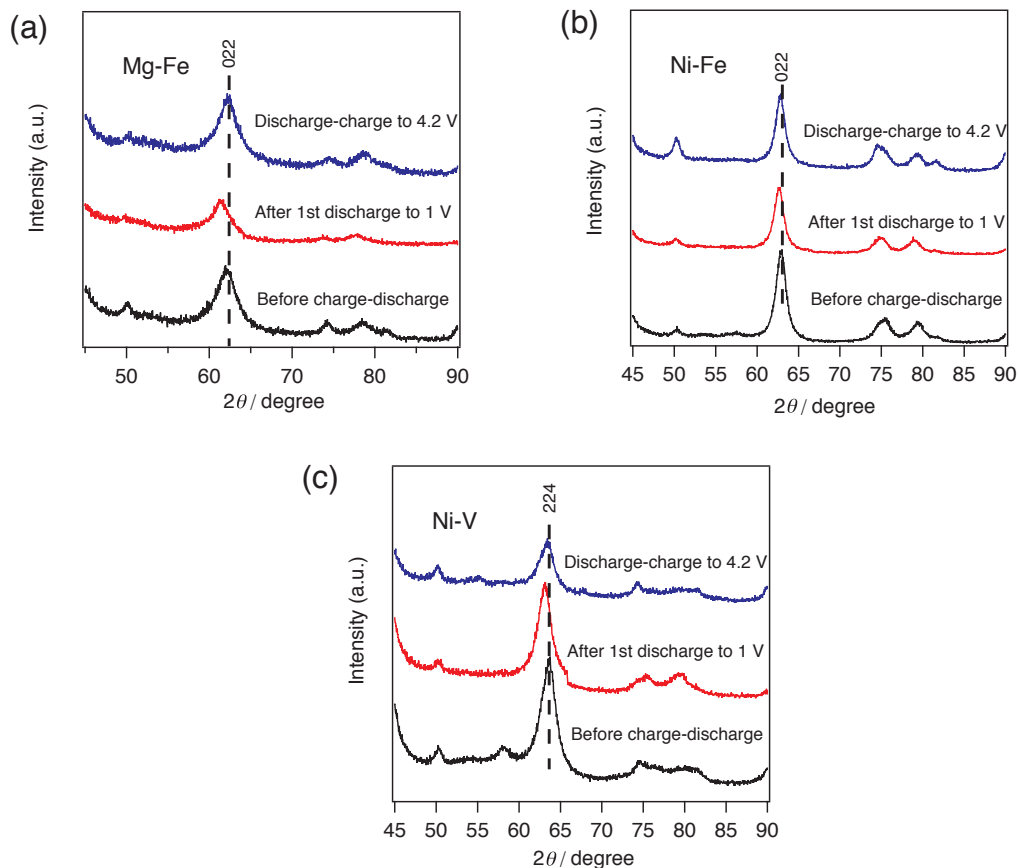


Figure 5.8 The ex-situ XRD patterns of (a) Mg-Fe, (b) Ni-Fe, (c) Ni-V at the stage of before charge-discharge, after first discharge to 1 V and recharge to 4.2 V.

For the further investigation of the reaction mechanism at lower voltage region, EIS analysis was performed on the cells during discharge-charge process. Figure 5.9 (a) and (b) showed the Nyquist plots upon first discharge-charge cycle at the potential range of 3~1 V for Mg-Fe sample. In Figure 5.9 (a), at early stage of discharge, a large semi-circle in high-middle frequency region and a straight line about 45° slope in the low frequency region were observed. The semi-circle in the high-middle frequency would be attributed to charge-transfer resistance since its diameter is dependent on the cell voltage. The straight line is related to Warburg impedance. Below 1.2 V, a small highly depressed second semi-circle

appeared in the low frequency region. Above 1.5 V of first discharge, only the change of charge-transfer resistance was observed. This would mean that the Li ion intercalation into cation vacancy is mainly proceeding and this is consistent with our discussion mentioned in the previous section. Laruelle et al. reported that a new large semi-circle appeared in very low frequency at 0.02 V by the conversion reaction of metal oxide, which is like a pseudo-capacitance-type behavior [16]. They explained that the absence of the 45° linear section was due to the low electronic conductivity and low ionic conductivity of the surface film on the electrode. For Mg-Fe electrode, the second semi-circle comes to be observed at 1.2 V that significantly higher than Laruelle's report and the small diameter of the second semi-circle was difficult to agree with low electronic and ionic conductivity compound they explained. Besides, Matsumura et al. proposed a reaction model that Fe³⁺ ion dissolved in the rutile type SnO₂ and reduced to Fe²⁺ attributes to the surface reaction on the α-Fe₂O₃-SnO₂ binary system at 1.2 V [17]. In the case of multiple metal oxide nanoparticles, until 1 V, dispersed Fe³⁺ in the host structure would be reduced to Fe²⁺ and then a part of Fe²⁺ would be further reduced with the surface reaction or a conversion reaction. A trace quantity of Li₂O might be formed accompanied with reduction to Fe. These Fe²⁺, or metallic Fe mixtures at the surface region of multiple metal oxides would become the new surface resistance at the low frequency region. Unfortunately, we cannot determine the exact component of this surface reaction matrix. Figure 5.9 (b) showed that the second semi-circle in the lower frequency region gradually faded in the subsequent charge process and, finally disappeared when voltage raised up to 2 V. This result suggests that the surface reaction matrix formed at low voltage region reacted to form the initial multiple metal oxide and Li⁺ ion reversely during the charge process up to 2 V. According to ex-situ XRD pattern in Figure 5.8, these formation and decomposition of surface reaction matrix seems to undergo without structure change of the host structure of multiple metal oxide.

In Figure 5.10 (a) and (b) are the Nyquist plots of Ni-Fe and Ni-V multiple

metal oxide nanoparticles during charge process of the first cycle. After first discharge to 1 V, the semi-circle in low frequency region clearly appears in addition to a semi-circle in high-middle frequency region, due to the formation of new surface reaction matrix as was discussed in the Mg-Fe system. The semi-circle lying in low frequency region, become unclear by charging up with decomposition of the new resistance phase as was the same to the Mg-Fe system. However, it seems that a little of this phase remained as residue until the voltage charge up to 3.5 V for Ni-Fe and Ni-V, because the second semi-circle did not disappeared completely. It seems that a small residual semi-circle is hidden in the semi-circle of charge-transfer resistance and straight line in Warburg region. The presence of residual surface reaction matrix may be the reason for the irreversible capacity in the first discharge.

The reaction mechanism, concluded on the basis of the results of the reversible change of the ex-situ XRD and EIS spectra of the multiple metal oxide nanoparticles at discharge-charge cycle was schematically illustrated in Figure 5.11. It indicates that (1) in the high voltage region of 4.2~1.5 V, Li^+ intercalation to the cation vacancy site of metal oxides proceeds, (2) in the low voltage region of 1.5 ~ 1.0 V, surface reaction with Li^+ occurs forming surface reaction matrix, (3) the inverse reaction of these steps are proceeds in the charging process with high reversibility without significant structure change of the host.

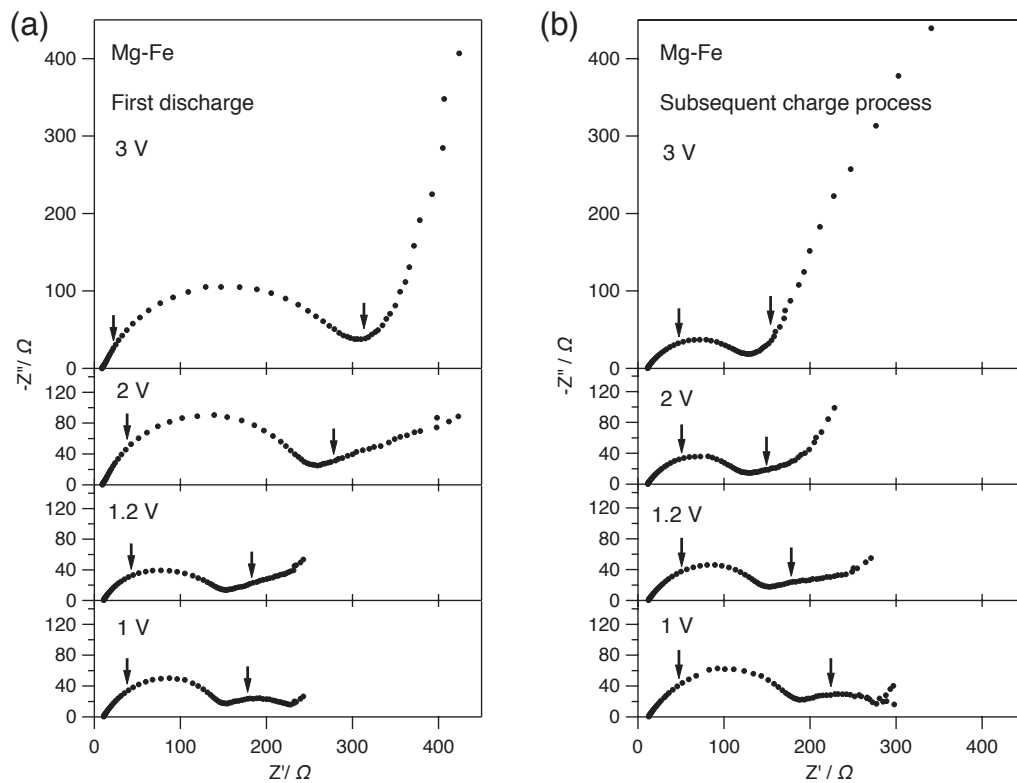


Figure 5.9 The Nyquist plots of Mg-Fe during (a) first discharge to 1V and (b) the first charge to 3 V. The EIS measurement was carried out in the frequency range from 10^6 Hz to 10^{-2} Hz under AC voltage with 10mV. Two arrows indicate the points obtained at 1 kHz and 1 Hz.

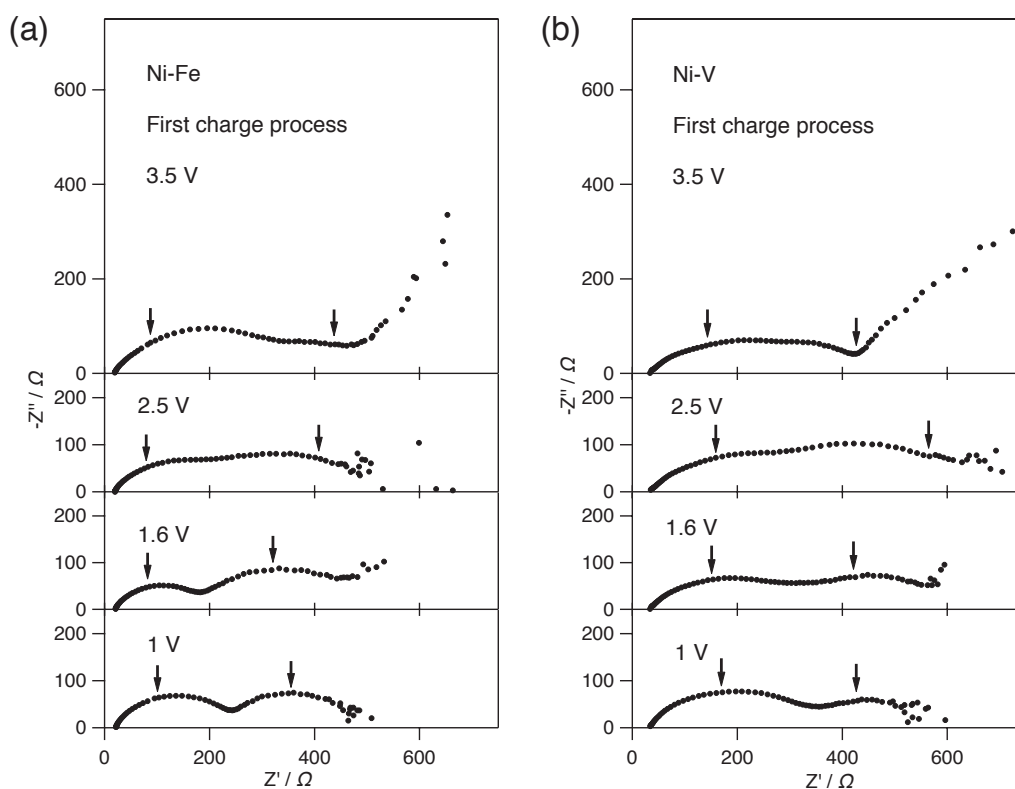


Figure 5.10 The Nyquist plots at various cell voltages in the first charging process. (a) Ni-Fe. (b) Ni-V. Two arrows indicate the points obtained at 1 kHz and 1 Hz.

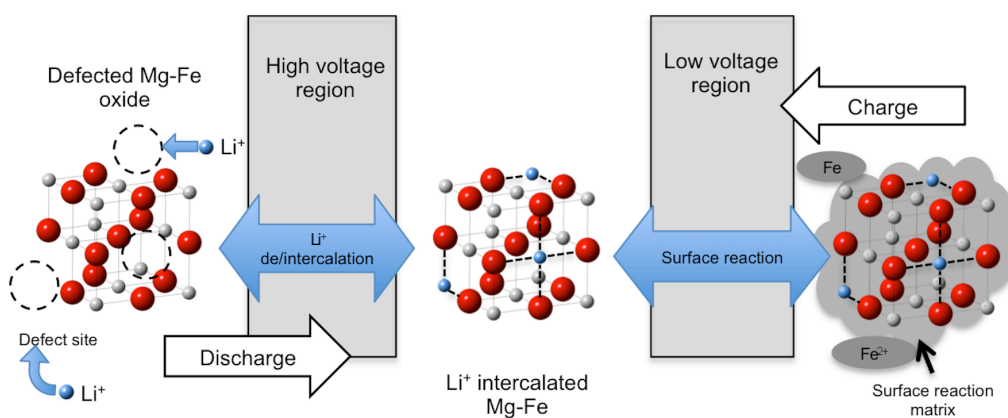


Figure 5.11 The schematic diagram for the reversible reaction mechanism of multiple metal oxides with Li ion.

5.4 Conclusion

Three multiple metal oxide nanoparticles of Mg-Fe and Ni-Fe with rock-salt structure and Ni-V with orthorhombic *Cmca* symmetry were synthesized by calcination of the LDH precursors at 400°C. The obtained multiple metal oxides consist of uniform fine particles with the size under 20 nm, and have extremely large surface area. From the result of XANES and composition analysis, these compounds are suspected to have cation vacancy. These multiple metal oxides showed very high reversible charge-discharge capacity and good capacity retention; especially, capacity of 327 mAh/g was obtained for Ni-V oxide nanoparticle at 10th cycle. In the charge-discharge process, the Li⁺ (de-)intercalation to the cation vacancy sites of the multiple metal oxide proceeds in the high voltage region and a formation of new surface reaction matrix reversibly occurs in the low voltage region after the Li⁺ insertion to all vacancies without remarkable structure change of the host. The multiple metal oxides will have possibility for a new type framework that can be used for the lithium storage.

Reference

- [1]K.H. Hwang, S.H. Lee, S.K. Joo, *J. Power Sources* 54 (1995) 224.
- [2]S. Komaba, N. Kumagai, M. Baba, F. Miura, N. Fujita, H. Groult, D. Devilliers, B. Kaplan, *J. Appl. Electrochem.* 30 (2000) 1179.
- [3]E. Levi, E. Zinigrad, H. Teller, M.D. Levi, D. Aurbach, E. Mengeritsky, E. Elster, P. Dan, E. Granot, H. Yamin, *J. Electrochem. Soc.* 144 (1997) 4133.
- [4]S. Kanzaki, T. Inada, T. Matsumura, N. Sonoyama, A. Yamada, M. Takano, R. Kanno, *J. Power Sources* 146 (2005) 323.
- [5]S. Kanzaki, A. Yamada, R. Kanno, *J. Power Sources* 165 (2007) 403.
- [6]S. Ito, K. Nakaoka, M. Kawamura, K. Ui, K. Fujimoto, N. Koura, *J. Power Sources* 146 (2005) 319.
- [7]M. Hibino, J. Terashima, T. Yao, *J. Electrochem. Soc.* 154 (2007) A1107.
- [8]B. Koo, H. Xiong, M.D. Slater, V.B. Prakapenka, M. Balasubramanian, P. Podsiadlo, C.S. Johnson, T. Rajh, E.V. Shevchenko, *Nano Lett.* 12 (2012) 2429.
- [9]X. Guo, F. Zhang, D.G. Evans, X. Duan, *Chem. Commun.* 46 (2010) 5197.
- [10]J. Morales, L. Sanchez, S. Bijani, L. Martinez, M. Gabas, J.R. Ramos-Barrado, *Electrochem. Solid-State Lett.* 8 (2005) A159.
- [11]F. M. Labajos, M. Dolores Sastre, R. Trujillano, V. Rives, *J. Mater. Chem.* 9 (1999) 1033.
- [12]D. Tichit, M.N. Bennani, F. Figueras, J.R. Ruiz, *Langmuir* 14 (1998) 2086.
- [13]G.A. Caravaggio, C. Detellier, Z. Wronski, *J. Mater. Chem.* 11 (2001) 912.
- [14]E.E. Sauerbrei, R. Faggiani, C. Calvo, *Acta Crystallographica Section B* 29 (1973) 2304.
- [15]K.H. Hwang, S.H. Lee, S.K. Joo, *J. Electrochem. Soc.* 141 (1994) 3296.
- [16]P. Poizot, S. Laruelle, S. Grugeon, J.M. Tarascon, *J. Electrochem. Soc.* 149 (2002) A1212.

[17]T. Matsumura, N. Sonoyama, R. Kanno, M. Takano, Solid State Ionics
158 (2003) 253.

Chapter 6

Summary

Nanostructured materials are becoming increasingly important for developing lithium battery technology. Although the attractive advantages of nanoelectrode motivate serious effort on approving nanomaterials, potentially complex synthesis process and high fabrication cost delays industrial application. Accordingly, easy and inexpensive synthesis methods for nanostructured electrode with excellent electrochemical properties are demanded. This study described the preparation process for LiCoO_2 thin film consisted of nanoparticles and multiple metal oxide nanoparticles using layered compounds as starting materials without any special apparatus. The electrochemical properties and reaction mechanism of these nanoelectrode also investigated carefully. The results of each material are summarized as follows.

In Chapter 2, LiCoO_2 thin films were synthesized on Au substrates by nanosheet restacking method and subsequent hydrothermal reaction. The result of XRD reflection indicated that LiCoO_2 films consisted of nanoparticles with the particle size of 15 nm. Comparing the rate performance of the thin films with various thickness, the optimum performance was obtained by the thin film with 5 min deposition time: 62% of the capacity was held at 400 C-rate compared with that at 20 C-rate. The SEM images of thin films showed that thinner film has three-dimensional surface structure, whereas surface of thicker films become flatter. It is considered that the large contact area between electrode and electrolyte of thinner film associated to three-dimensional surface structure facilitated the rate performance

In chapter 3, LiCoO₂ thin films were coated on the surface of carbon materials using the nanosheet restacking method and hydrothermal treatment, based on the study of chapter 2. Firstly, the LiCoO₂ thin film was fabricated on glassy carbon substrate. An excellent high rate discharge capability, 72% of cathode utilization efficiency at 300 C-rate compared with that at 30 C-rate, was obtained using the thinnest film with 5 min deposition time. Secondly, the LiCoO₂ nanoparticle was coated on the surface of acetylene black powder. A good high rate charge-discharge capability was also obtained on the acetylene black powder: 66% of the capacity retained at 17 C in comparison with that at 1.7 C, which is superior to the reports of other bulk materials. On contrast, LiCoO₂ thin film coated on the Toka black and TiO₂ powder only showed insufficient electrochemical property. It demonstrates that the nature of substrate and coverage of thin film strongly influence the electrochemical performance.

In chapter 4, The LiMn₂O₄ thin films composed of nanoparticles were synthesized by sintering electrodeposited Mn₃O₄ precursor on the Au substrate, and the electrochemical properties were investigated. The electrochemical performance was dependent on the film thickness. For the thinner LiMn₂O₄ films, cycling in the voltage range of 4.3 ~ 3.4 V resulted in superior rate performance, that is almost 100 % of discharge capacity compared with that at 20 times of discharge current density, and good stability without capacity loss until 500 cycles. CV and EIS measurements revealed that LiMn₂O₄ thin film has good electric contact with substrate and high lithium diffusion coefficient of 10⁻⁹~10⁻¹¹ cm²/s could be obtained.

In chapter 5, the multiple metal oxide nanoparticles, Mg-Fe, Ni-Fe, Ni-V oxides were synthesized by calcination of the LDH precursors. These multiple metal oxides have the uniform particle size less than 20 nm and huge surface area. Among three kinds of multiple metal oxide nanoparticles, Ni-V oxide showed highest charge-discharge capacity of 327 mAh/g in the voltage range 4.2~1.0 V.

Furthermore, the reaction mechanism carefully investigated by ex-situ XRD and AC impedance technique. It is cleared that two-step reaction reversibly occurs during charge-discharge process. In the higher voltage region, the Li^+ (de-)intercalation to the cation vacancy sites of the multiple metal oxide without major phase change. In the lower voltage region, the formation and decomposition of new surface reaction matrix.

The nanoelectrodes obtained this study showed significantly improved performance compared with bulk materials. In addition, the further development of nanomaterials derived from layered compounds is worth expecting. For example, abundant nanosheets derived from various layered compounds allow us to design nanostructures through various assemble method with peculiar properties. The capacity and cyclability of multiple metal oxide nanoparticles are possible to enhance by the abundant metal combination succeeded to LDHs. Thus, using layered compounds as starting materials is promising way to develop nanostructure materials for lithium batteries.

List of publication

1. Zhen Quan, Shouya Ohguchi, Masayasu Kawase, Hiroshi Tanimura and Noriyuki Sonoyama, "Preparation of nanocrystalline LiMn_2O_4 thin film by electrodeposition method and its electrochemical performance for lithium battery", *Journal of power sources*, in press, 2013.
2. Zhen Quan, Shouya Ohguchi, Masayasu Kawase, Noriyuki Sonoyama, "Synthesis and electrochemical property of LiMn_2O_4 thin film by electrodeposition method", *Proceeding of the 13th asian conference on solid state ionics*, pp. 128-137, 2012.
3. Zhen Quan, Tomoki Osokoshi, Noriyuki Sonoyama, "Synthesis and electrochemical property of LiCoO_2 thin film coated on the surface of carbon and anatase TiO_2 powders", *Journal of alloys and compounds*, Vol. 541, pp.137-143, 2012.
4. Shinya Uematsu, Zhen Quan, Yoshiaki Suganuma, Noriyuki Sonoyama, "Reversible lithium charge-discharge property of bi-capped Keggin-type polyoxovanadates", *Journal of power sources*, Vol. 217, pp. 13-20, November, 2012.
5. Noriyuki Sonoyama, Kenichi Inukai, Kentaro Hanamura, Takeshi Yamada, Zhen Quan, "Electrochemical luminescence of Gallium-ion-doped MgIn_2O_4 electrodes", *Journal of electrochemical society*, Vol. 158, pp. P140-P146, 2011.

6. Zhen Quan, Kosuke Iwase, Noriyuki Sonoyama, “Synthesis and electrochemical property of LiCoO_2 thin films composed of nanosize compounds synthesized via nanosheet restacking method”, *Journal of power sources*, Vol. 196, pp. 6762-6767, August, 2011.

7. Noriyuki Sonoyama, Yoshiaki Suganuma, Tomohiro Kume, Zhen Quan, “Lithium intercalation reaction into the Keggin type polyoxomolybdates”, *Journal of power sources*, Vol. 196, pp. 6822-6827, August, 2011.

Acknowledgements

The author would like to express his ultimate gratitude to the supervisor, Associate Professor Noriyuki Sonoyama, Nagoya Institute of Technology, for earnest guidance, warmhearted encouragement and valuable discussions during doctoral course.

The author is very grateful to Professor Masaki Tanemura and Professor Kazutake Takada of Nagoya Institute of Technology for the AFM, SEM and QCM measurements.

The author wishes to express his sincere thanks Professor Nobuyuki Imanishi and Mr. Takayuki Ichikawa of Mie University for the SEM, BET measurements and valuable advises.

The author wishes to appreciate to all of former and present students in the same laboratory for their continuous encouragement and support.

Quan Zhen
January, 2013